

November 2013

# Electromagnetic Interactions Between Metal Nanoparticles and Fluorescent Dipoles

Christopher John Breshike  
*Florida State University*

Follow this and additional works at: <http://diginole.lib.fsu.edu/etd>

---

## Recommended Citation

Breshike, Christopher John, "Electromagnetic Interactions Between Metal Nanoparticles and Fluorescent Dipoles" (2013). *Electronic Theses, Treatises and Dissertations*. Paper 8740.

This Dissertation - Open Access is brought to you for free and open access by the The Graduate School at DigiNole Commons. It has been accepted for inclusion in Electronic Theses, Treatises and Dissertations by an authorized administrator of DigiNole Commons. For more information, please contact [lib-ir@fsu.edu](mailto:lib-ir@fsu.edu).

FLORIDA STATE UNIVERSITY  
COLLEGE OF ARTS AND SCIENCES

ELECTROMAGNETIC INTERACTIONS BETWEEN METAL NANOPARTICLES AND  
FLUORESCENT DIPOLES

By

CHRISTOPHER JOHN BRESHIKE

A Dissertation submitted to the  
Department of Chemistry and Biochemistry  
in partial fulfillment of the  
requirements for the degree of  
Doctor of Philosophy

Degree Awarded:  
Spring Semester, 2014

Christopher John Breshike defended this dissertation on November 1, 2013.

The members of the supervisory committee were:

Geoffrey Strouse  
Professor Directing Dissertation

Piotr Fajer  
University Representative

Timothy Logan  
Committee Member

Kenneth Goldsby  
Committee Member

The Graduate School has verified and approved the above-named committee members, and certifies that the dissertation has been approved in accordance with university requirements.

For Paige, without you nothing that follows would have been.

## **ACKNOWLEDGEMENTS**

Thanks to my mom for your unyielding support which nurtured me into believing I can do anything I set my mind to. Her optimism has been contagious. My wife Paige for supporting me through this endeavor in all things. Thank you for relieving pressure when I thought I was going to drown by letting me know you would be there for me no matter how badly I failed. Thanks to my dad for teaching me to the value of doing things yourself. Dr. Horry, and Jason (Paige's cousin) for testing my knowledge and ensuring I know what I am talking about. Thanks to my brother Tricio for keeping me level headed... at all times. Special thanks to my Aunt Stace for her part in the editing process. I need to thank Ryan Riskowski for saving my project and giving me a different perspective to bounce ideas off of. Thanks to Prof. Strouse for his mentorship and showing me how much I can accomplish if I put my mind to it.

Finally I need to thank my first high school chemistry teacher, Mr. Brian Otterson, without you I would have continued to be a resentful student who thought teachers were always against him. You engaged me in your subject matter more than any teacher ever had and pulled me in with your exclusion of yourself from the human limitations you presented in class. You showed me the value of knowledge and critical thinking, thank you so much for leading me down this path.

# TABLE OF CONTENTS

List of Tables .....	vii
List of Figures .....	viii
List of Abbreviations .....	xii
List of Symbols .....	xiv
Abstract .....	xvii
1. Introduction.....	1
1.1 Properties of Metal Nanoparticles .....	1
1.1.1 Localized Surface Plasmons .....	4
1.2 Energy Transfer .....	6
1.2.1 A Brief History .....	9
1.2.2 State of the Art.....	16
1.2.3 Applications and Limitations .....	17
1.3 Summary of Chapters .....	19
2. Synthesis of Metal Nanoparticles and Metal Oxides.....	20
2.1 Introduction .....	20
2.1.1 Nucleation.....	21
2.1.2 Passivation.....	21
2.2 Metal Nanoparticle Synthesis.....	22
2.2.1 Water Soluble Methods .....	22
2.2.2 Biphasic Reduction of Metal Particles (Ni, Pd, Pt, and Au) .....	39
2.3 Microwave Synthesis.....	39
2.3.1 Copper Nanoparticles .....	39
2.3.2 Fe <sub>3</sub> O <sub>4</sub> Microwave Synthesis .....	42
2.4 Gold Shelling of Iron Oxide .....	42
3. Nanometal Surface Energy Transfer Predicts the Size-Enhanced Energy Coupling Between a Metal Nanoparticle and an Emitting Dipole .....	48
3.1 Introduction .....	48
3.2 Experimental Section.....	52
3.2.1 Materials .....	52
3.2.2 Energy Transfer Measurements.....	52
3.3 Results and Discussion .....	54
3.3.1 Experimental Validation of Size Dependent NSET .....	62
3.3.2 DNA Orientation Effects .....	63
3.3.3 Experimental Considerations.....	68
3.3.4 Photoluminescent Quenching Results .....	80
3.4 Conclusion .....	80
4. Super Quenching of Blue Dyes.....	86
4.1 Introduction .....	86
4.2 Materials and Methods .....	87
4.3 DNA Complex Results .....	88
4.4 Stern-Volmer Studies .....	94
4.4.1 Stern-Volmer on AF350 .....	94
4.4.2 Diphenyl Anthracene Stern-Volmer .....	100
4.5 Conclusions .....	101

REFERENCES .....	105
BIOGRAPHICAL SKETCH .....	111

## LIST OF TABLES

<b>Table 2.1</b> Volume of tannic acid to achieve desired nanoparticle diameter .....	23
<b>Table 2.2</b> The XRF results for Au/Pd alloyed nanoparticles prepared by method 2. The data shows good correlation between the mole fraction of the reactants and the mole fraction in the products.....	37
<b>Table 3.1</b> DNA sequences used as spacers for the proximal quenching of the dyes, FAM and Cy3B .....	53
<b>Table 3.2</b> Optical constants used in the derived NSET equation.....	58
<b>Table 3.3:</b> Orientation constants for calculating distance errors.....	66
<b>Table 3.4.</b> Theoretical and experimental NSET values for FAM and Cy3B .....	67
<b>Table 3.5</b> Lifetime values for Cy3B quenching studies by AuNP.....	81
<b>Table 4.1</b> List of DNA sequences used in the proximal study of the quenching of AF350 by 2nm AuNPs.....	91

## LIST OF FIGURES

<b>Figure 1.1</b> Nanoparticles in the quasi-static regime are too small to be effected by the sinusoidal properties of light.....	2
<b>Figure 1.2</b> Incident light induces an oscilation of the electrons in the nanoparticle, resulting in nonuniform charge around the surface of the particle .....	5
<b>Figure 1.3</b> (a) Shows the extinction spectra of AuNPs with different radii. (b) Normalized absorption spectra of the AuNPs illustrating a broadening with decreasing radii .....	7
<b>Figure 1.4</b> Illustrates the differences in quenching efficiencies for two models predicting different power dependence .....	9
<b>Figure 1.5</b> (a) Illustrations of the different orientations the acceptor and donor dipoles can have, their corresponding $k^2$ values for the FRET calculation are as follows i) $k^2=1$ , ii) $k^2=0$ , iii) $k^2=4$ , iv) $k^2=2/3$ . (b) Represents the J-integral for a FRET pair of fluorescent dipoles with FAM (donor) and TAMRA (acceptor) .....	12
<b>Figure 1.6</b> Illustrates the orientations the CPS-Kuhn model is solved for. The red dipole along the x-axis, and the circle with an “X” in it represents a dipole along the y-axis are both parallel to the metal film and the black dipole along the z-axis is perpendicular .....	14
<b>Figure 1.7</b> A volume of uncoupled dipoles, in the metal nanoparticle, with all possible orientations couple efficiently to a donor dipole at a set distance from the particle .....	15
<b>Figure 1.8</b> A surface of strongly coupled dipoles couples to an oscillating dipole a set distance from that surface .....	17
<b>Figure 2.1</b> Principle of nucleation. First ions (yellow balls with + signs) are reduced with electrons and form monomer (plain yellow balls) that grow into bulk (large yellow ball) .....	21
<b>Figure 2.2</b> TEM image with size analysis for 3.0nm AuNP showing a standard deviation of 0.6nm. Scale bar in image represents 20nm .....	24
<b>Figure 2.3</b> TEM image with size analysis for 4.2nm AuNPs showing a standard deviation of 1.1nm. Scale bar in image represents 20nm .....	25
<b>Figure 2.4</b> TEM image with size analysis for 5.3nm AuNPs showing a standard deviation of 0.9 nm. Scale bar in image represents 200nm .....	26

<b>Figure 2.5</b> TEM image with size analysis for 6.6nm AuNPs showing a standard deviation of 0.57 nm. Scale bar in image represents 50nm .....	27
<b>Figure 2.6</b> TEM image with size analysis for 16.5nm AuNPs showing a standard deviation of 2.4 nm. Scale bar in image represents 5nm .....	28
<b>Figure 2.7</b> TEM image with size analysis for 20.2nm AuNPs showing a standard deviation of 1.1 nm. Scale bar in image represents 20nm .....	29
<b>Figure 2.8</b> Normalized absorption spectra for a range of AuNP sizes.....	32
<b>Figure 2.9</b> (a) The extinction spectra for various size AuNPs. (b) Plot of the extinction coefficients of the peak absorption at 520 and slightly red of the peak at 570nm.....	34
<b>Figure 2.10</b> Reaction mechanism for citrate reduction and subsequent ligand exchange of AuNP.....	35
<b>Figure 2.11</b> TEM image with size analysis for 1.89nm AuNPs showing a standard deviation of 0.35. Scale bar in image represents 5nm.....	38
<b>Figure 2.12</b> Mechanism for metal nanoparticle formation from the biphasic method. $M^{+n}$ represents the metal ion of choice ( $Au^{3+}$ , $Pd^{2+}$ , $Pt^{2+}$ , $Ni^{2+}$ , or $Ag^{+}$ ) that is coordinated with TOA to phase transfer into toluene from water. TPP is then added and some of the M ions form complexes with it (usually seen as a color change in the reaction solution) and then the ions are reduced with $NaBH_4$ and form TPP passivated NPs .....	40
<b>Figure 2.13</b> Microwave formed Copper nanoparticles mean diameter of 6.6nm and a size distribution of 1.01nm. Scale bar in the image represents 100nm.....	41
<b>Figure 2.14</b> TEM of $Fe_3O_4$ nanoparticles with a mean diameter of about 7nm and a distribution of 0.6nm, scale bar 20nm.....	43
<b>Figure 2.15</b> (a) TEM of Au shelled $Fe_3O_4$ nanoparticles. (b) shows the saturation limit of the $Fe_3O_4$ drops from 64emu/g to 8 emu/g after gold shelling .....	46
<b>Figure 2.16</b> (a) absorption spectra of Au coated $Fe_3O_4$ nanoparticles suspended in Toluene. (b) pXRD pattern for the Au coated $Fe_3O_4$ .....	47
<b>Figure 3.1</b> Theoretical size dependent NSET curves illustrating the size dependent behavior for (a) $d_0$ value for FAM, (b) efficiency curve for FAM, (c) $d_0$ value for Cy3B, and (d) efficiency curve for Cy3B. The experimental points calculated from separation distance dependent experimental data for the $d_0$ curves in (a) and (b) are shown as black diamonds.....	60

**Figure 3.2** a) Schematic model of AuNP-DNA-fluorescent molecule construct. b) Spectral overlap between 8nm AuNP extinction spectra and the fluorescent molecule emission spectra in water for FAM and Cy3B .....64

**Figure 3.3** Schematic representation of DNA tilt relative to spherical AuNP, where d is separation distance, d' is DNA length from Clegg model, r is the AuNP radius, and  $\theta$  is the angle of tilt relative to normal .....65

**Figure 3.4** a) Absorption spectra of 4.0nm AuNP with different loading levels of FAM labeled DNA strands. b) Energy transfer efficiencies of the different loading levels of DNA on 4.0nm AuNP.....70

**Figure 3.5** Theoretical size dependent efficiency curves, for the developed model as well as two other leading theories, and experimental values for selected separation distances for FAM as an excited state donor to AuNP with radii of (a)  $0.95 \pm 0.18$  nm, (b)  $1.5 \pm 0.30$  nm, (c)  $2.16 \pm 0.55$  nm, (d)  $2.65 \pm 0.45$  nm, (e)  $3.3 \pm 0.5$  nm, (f)  $4.0 \pm 0.3$  nm, and (g)  $8.25 \pm 1.20$  nm , along with the residual plots for each size. (h) All sizes overlaid (i) All sizes overlaid for the Cy3B.....71

**Figure 3.6** a) DNA length dependent FAM quenching data for 0.945 nm radius AuNP b) DNA length dependent FAM quenching data for 1.5 nm radius AuNP c) DNA length dependent FAM quenching data for 2.15 nm radius AuNP d) DNA length dependent FAM quenching data for 2.65 nm radius AuNP e) DNA length dependent FAM quenching data for 3.3 nm radius AuNP f) DNA length dependent FAM quenching data for 4.0 nm radius AuNP g) DNA length dependent FAM quenching data for 8.25 nm AuNP .....81

**Figure 4.1** Illustration the experimental approach to investigating the distance dependence of the quenching behavior blue dyes will have. The gold ball in the middle represents the AuNP, the red cloud its near-field, the blue its far-field, and the yellow arrows dipoles at discrete distances from the AuNP .....92

**Figure 4.2** Spectral overlay of 2nm absorption spectra with AF350 absorption and emission. The arrow at 520nm indicates the decline of the intraband and the beginning of the interband transitions .....93

**Figure 4.3** Normalized PL intensity for AF350 for the control (AF350 labeled strand in the presence of unappended AuNPs) and the different length strands appended to the surface of the 2nm AuNP .....93

**Figure 4.4** Melting study indicates that as the ds-DNA is melted the AF350 signal returns as the labeled strand diffuses away .....96

**Figure 4.5** a) Temperature dependence of free AF350 labeled DNA. b) Plot of the normalized integrals for the temperature dependence .....97

**Figure 4.6** Efficiency curves for several theories explaining resonant energy transfer coupled to the LSPR of metal NPs the data point with the red circle around it represents the 90mer and is noted because it is likely that the rigid rod approximation is failing.....98

**Figure 4.7** a) Raw data for Stern-Volmer studies on AF350 b) Stern-Volmer plot included points corrected for the inner filter effect with line of best fit on the corrected data to extract a  $K_{SV}$  of  $41735M^{-1}$  .....102

**Figure 4.8** The  $I_0/I$  plots of the intensity integrals of the diphenyl anthracene fluorescence in the presence of various 2nm AuNP concentrations along with the points corrected for the inner filter effect and a best fit line to extract a  $K_{SV}$  of  $636720M^{-1}$  .....103

**Figure 4.9** Lifetime results for Stern-Volmer studies on the least concentrated and most concentrated AuNP samples with single exponential decay fits .....103

**Figure 4.10** Plot of the  $\tau_0/\tau$  and  $I_0/I$  data showing a lack of agreement between lifetime and steady state experiments leads to the conclusion of static quenching of the DPA .....104

## LIST OF ABBREVIATIONS

AuNPs-	Gold nanoparticles
UV-Vis-	Ultraviolet-Visible
nm -	nanometer
NPs -	nanoparticles
LSPR -	localized surface plasmon resonance
SERS -	surface enhanced Raman scattering
NSET -	nanometal surface energy transfer
FRET -	Förster Resonance Energy Transfer
LRET -	Lanthanide Resonance Energy Transfer
CRET -	Chemiluminescence Resonance Energy Transfer
RET -	Resonance Energy Transfer
sp-FRET-	single particle Förster Resonance Energy Transfer
FAM -	fluorescein
TAMRA-	carboxytetramethylrhodamine
CPS-Kuhn-	Chance Prock Silber and Kuhn model
G-N -	Gersten-Nitzan model
BRET -	Bioluminescence Resonance Energy Transfer
RNA -	Ribonucleic acid
DNA -	Deoxyribonucleic acid
sdNSET-	size dependent nanometal surface energy transfer
TPP -	triphenyl phosphine
BSPP -	bis(sulfanoto phenyl)phenyl phosphine
TOABr-	tetraoctylammonium bromide
TEM -	transmission electron microscopy
acac -	acetylacetonate
Olac -	Oleic acid
OIA -	Olyelamine
HAD -	hexadecylamine
pXRD -	powder X-ray Diffraction
Cy3B -	cyanine-3

R - distance  
bp - base pairs  
AuNP-DNA- gold nanoparticle DNA complex  
C<sub>6</sub> - six carbon linker  
PL - photoluminescence

## LIST OF SYMBOLS

$\omega$	-	frequency
$\omega_p$	-	Drude plasmon frequency
$\epsilon_1$	-	Complex dielectric function of a metal nanoparticle
$\epsilon_\infty$	-	Complex dielectric function of a bulk metal
$\epsilon_{Drude}$	-	Complex dielectric function calculated using the Drude assumptions
$\epsilon_{IB}$	-	Complex dielectric function accounting for the interband transitions
$\Gamma_r$	-	size-dependent damping constant
$\Gamma_\infty$	-	damping constant of bulk material
$l_\infty$	-	mean free path of an electron
$r$	-	Nanoparticle radius
$k_p$	-	plasmon wave vector
$\lambda$	-	wavelength
$\pi$	-	pi
$\epsilon_2$	-	complex dielectric function of medium
$d$	-	distance
$d_0$	-	50% quenching distance
$R_0$	-	50% quenching distance
$n$	-	power dependence
$\kappa$	-	orientation factor in FRET
$\Phi_D$	-	native quantum yield of donor
$J(\lambda)$	-	overlap integral
$N_A$	-	Avogadro's number
$n_m$	-	index of refraction of medium
$f_D(\lambda)$	-	normalized emission spectra for donor
$\epsilon_A(\lambda)$	-	extinction spectra of acceptor
$\text{\AA}$	-	angstrom
$\alpha$	-	orientation factor in CPS-Kuhn and sdNSET models
$A$	-	absorptivity
$n_r$	-	index of refraction of a metal

$k$	-	extinction of a film
$\Phi$	-	quantum yield of donor
$c$	-	speed of light
$\omega_{\text{dye}}$	-	frequency of emission for dye
$\kappa_f$	-	Fermi wave vector of metal
$\omega_f$	-	Fermi frequency of metal nanoparticle
$^{\circ}\text{C}$	-	degrees Celsius
%	-	percentage
mg	-	milligram
$\epsilon$	-	extinction coefficient
$b$	-	path length
$c$	-	concentration
$I$	-	intensity
$I_0$	-	control intensity
$E_{\text{EnT}}$	-	energy transfer efficiency
mM	-	millimolar
$\mu\text{L}$	-	microliter
$\tau$	-	lifetime
$\tau_0$	-	native lifetime
mW	-	milliwatt
$k_{\text{obs}}$	-	rate of emission
$k_r$	-	radiative rate
$k_{\text{nr}}$	-	nonradiative rate
$F_{\text{DA}}$	-	interaction coefficient of a system
$\epsilon_2'$	-	real component of the dielectric function of a material
$\epsilon_2''$	-	imaginary component of the dielectric function of a material
$i$	-	square root of -1
$\omega_i$	-	critical frequency
$\varphi_i$	-	efficiency of transition
$\Gamma_i$	-	dampening constant of interband transition
$\epsilon_{\lambda}$	-	extinction coefficient of nanoparticle

- $r_{cm}$  - radius of nanoparticle in cm  
 $V_{cm^3}$  - volume of nanoparticle in  $cm^3$   
 $\delta_{skin}$  - skin depth of light

## **ABSTRACT**

Nanoparticles are at the forefront of science and technology today. This dissertation will expand the basic fundamental understanding of the phenomenon known as resonant energy transfer. A number of analytical techniques were utilized to characterize metal nanoparticles that were synthesized for use in energy transfer; including transmission electron microscopy, powder X-ray diffraction, X-ray fluorescence spectroscopy, UV-Vis absorption spectroscopy, photoluminescence spectroscopy, and time resolved fluorescent lifetime spectroscopy (Chapter 2). A new theoretical model is developed explaining the observation of the size dependence that gold nanoparticles have on the rate of energy transfer from dyes whose emission is in resonance with the localized surface plasmon of those particles (Chapter 3). Then the role of the  $d \rightarrow sp$  transitions of gold nanoparticles will be observed by tracking the quenching behavior of dyes that emit higher energy than the plasmon (Chapter 4).

# CHAPTER ONE

## INTRODUCTION

### 1.1 Properties of Metal Nanoparticles

Nanoparticles have been the subject of intense research for decades. Metal nanoparticles are widely utilized today as molecular beacons, drug delivery hosts, catalysts, and in molecular sensing devices [1, 2, 3, 4]. Energy transfer in these modern day applications, is a particularly powerful way researchers have utilized the unique properties of metal nanoparticles among other nanomaterials. The nature and efficiency of energy transfer is dependent on the optical properties of the donor, acceptor and the separating medium. This dissertation will study the effect that the optical properties of the acceptor have on the energy transfer behavior. Specifically, the mechanism for which metal nanoparticles quench fluorescent molecules at a set distance will be investigated. Even with the extensive applications of nanoparticles in energy transfer the fundamental understanding of the specific mechanism that the acceptor and donor participate in is severely lacking. Several models in the literature exist that attempt to bring light to this complicated energy transfer mechanism but the correlation to experimental data is poor [5, 6, 7, 8]. This dissertation will attempt to broaden the fundamental understanding of how metal nanoparticles interact with oscillating dipoles, in hopes that it will improve the design of future technologies.

First, it is important to describe the metal nanoparticle size regime that was analyzed in these studies, as the optical properties under investigation are size dependent. While the term “nano” is potentially overused or trendy in this field, it is crucial to emphasize that “nano” is technically indicative of any material measuring under a micron in size. For the purposes of all the studies that follow in this dissertation, Kriebeg’s of “very small clusters” will be used, which

distinguishes nanoparticles ranging in size from 2-20nm [9]. This places these studies in the quasi-static regime. An important aspect of working in this size regime, is the sinusoidal nature of incident light can essentially be ignored, illustrated in Figure 1.1.

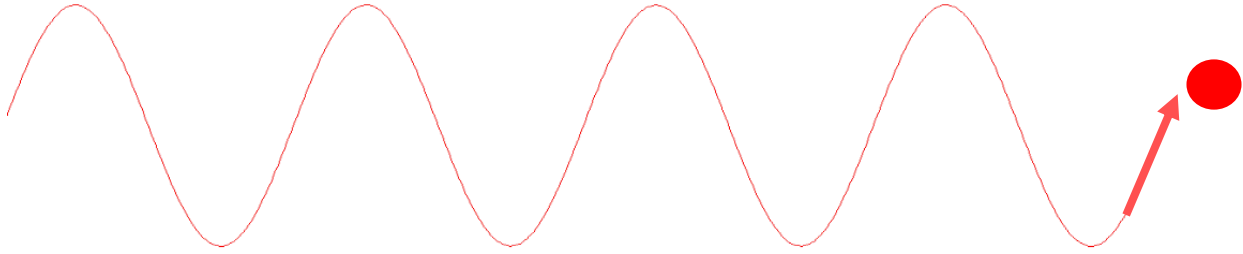


**Figure 1.1** Nanoparticles in the quasi-static regime are too small to be effected by the sinusoidal properties of light.

Taking this into account greatly simplifies the theoretical calculations needed to understand the optical properties of metal nanoparticles. The first optical property to be discussed will be the complex dielectric function. This function explains the interaction of light as it travels from a surrounding medium into that material. There are two components that dictate the behavior of the complex dielectric function: the real component, which consists of the scattering behavior, and the imaginary component, which encompasses the absorptivity. [9]

Light can undergo several processes, related to the dielectric function, as it passes through a substance. First, it can be scattered, which includes reflection and diffraction, described by the real component of the dielectric function. This light is considered “real” because it can be directly measured. It is important to note that the scattering efficiency of incident light by metal nanoparticles in this size regime is minimal. The second process that incident light can undergo is absorption, where light disappears from the physical measurement,

quantification of this light is indirect, and thus, this process is appropriately described by the imaginary dielectric component [87, 9]. To accurately calculate the dielectrics of small nanoparticles, certain assumptions must be made. These assumptions are more specifically fragmented into energy ranges, where multiple models must be incorporated to attain the complete picture [10].

The Drude model treats the valence band of a metal as a fermi gas of free electrons that is essentially decoupled from the lattice of positive ions. The electrons described by the Drude approximations are responsible for the most prominent optical feature in metal nanoparticles known as the localized surface plasmon, which will be discussed later. Additionally, the interband transition treat the direct excitation of the core electrons. These electrons, which are coupled to the nuclei that make up the lattice, experience a restoring force by the broad positively charge of the lattice during the displacement of those electrons by the excitation process. This restoring force results in the interband transitions to require more energy to initiate than the oscillation of the conduction electrons [10].

Coupling these two models, the Drude approximations, which describe low energy interactions, with the incorporation of the interband transitions for higher energy electron transitions, it is possible to calculate the size dependent complex dielectric function of a given material, given in equation 1.1

$$\begin{aligned}\epsilon_1 &= \epsilon_\infty + \epsilon_{Drude} + \epsilon_{IB} & (1.1) \\ \epsilon_{Drude} &= 1 - \frac{\omega_p^2}{\omega^2 + \Gamma_r^2} + i \frac{\Gamma_r \omega_p^2}{\omega(\omega^2 + \Gamma_r^2)} \\ \epsilon_{IB} &= \sum_{i=1,2} \frac{A_i}{\omega_i} \left[ \frac{e^{i\phi_i}}{\omega_i^{-1} - \omega^{-1} - \Gamma_i^{-1}} + \frac{e^{-i\phi_i}}{\omega_i^{-1} + \omega^{-1} + \Gamma_i^{-1}} \right]\end{aligned}$$

where  $\omega$  is frequency,  $\omega_p$  is the Drude plasmon frequency, and  $\Gamma_r$  is the size-dependent damping constant ( $\Gamma_r = \Gamma_\infty + \frac{l_\infty}{r}$ ), wherein  $\Gamma_\infty$  is the bulk damping constant of the material,  $l_\infty$  is the mean free path of an electron (in Au  $l_\infty = 420\text{\AA}$ ), and  $r$  is the nanoparticle radius [11, 12]. This dielectric function will be important in determining how metal nanoparticles can interact with oscillating dipoles, treated as incident light. For this reason, energy transfer involving metal nanoparticles is presumed to be coupled to the Drude electrons that are lower in energy and participate in a surface plasmon.

### 1.1.1 Localized Surface Plasmons

Most noble metals exhibit a surface plasmon, which is an induced oscillation of the electrons at the surface of the metal, when irradiated with a specific frequency of light, known as the plasmon frequency  $\omega_p$ . In bulk material this surface plasmon is manifested as an evanescent wave that travels over the surface of the metal until it eventually dissipates as heat.[9] This resonance condition is met in equation (1.2) for the plasmon wave vector  $k_p$  [13,14]

$$k_p = \left(\frac{2\pi}{\lambda}\right) \sqrt{\frac{\varepsilon_1 \varepsilon_2}{\varepsilon_1 + \varepsilon_2}} \quad (1.2)$$

where  $\lambda$  is the wavelength of the incident light, and  $\varepsilon_1$  and  $\varepsilon_2$  are the dielectric permeability constants at that wavelength for the metal and exit medium, respectively. As the bulk metal dimensions decrease in size, this surface plasmon begins to localize as an oscillation of the electrons strictly at the surface of the particle as illustrated in Figure 1.2 [9, 12]. This induced oscillation of the electrons at the surface of the particle is known as the localized surface plasmon resonance (LSPR). It is clear from equation (1.2) that the LSPR energy is environment dependent and will shift with the dielectric of the surrounding medium, a crucial characteristic

for experimental design. This means that experimental observations will be dependent on the solvent the nanoparticles are suspended in.

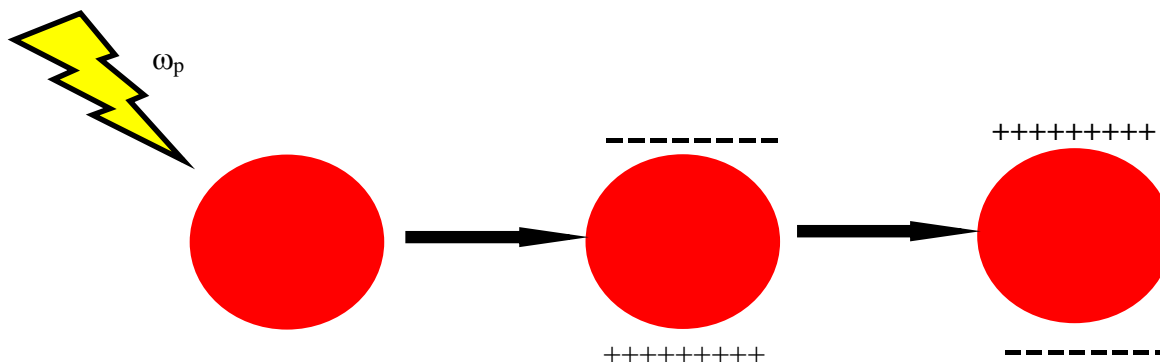


**Figure 1.2** Incident light induces an oscillation of the electrons in the nanoparticle, resulting in nonuniform charge around the surface of the particle

The LSPR is likely the most studied characteristic of gold nanoparticles. It is known to have two modes of oscillation, a transverse and a longitudinal model. In spherical particles these modes overlap and are degenerate [15]. This is represented in the extinction spectra of spherical gold nanoparticles (AuNPs) by a single plasmonic peak, in gold at approximately 520nm in water, illustrated in Figure 1.3a. The transverse and longitudinal modes split as the particles are shaped into rods or cubes, resulting in a higher energy peak (the transverse mode) and a lower energy peak (the longitudinal) [16]. The extinction spectra arises from the polarizability and dielectric function of the nanometal and thus, encompasses both scattering and absorption of light. When measured, the extinction spectra can provide information about the size, shape and structure of the nanometal. While the studies conducted in this dissertation develop a fundamental understanding of energy transfer solely with spherical nanoparticles, the lessons learned will be fully translatable to nanoparticles of different shapes.

The LSPR band is extremely sensitive to size, composition, shape, and environment [9, 10, 12]. As the nanometal gets smaller the plasmon begins to broaden out and eventually breaks

into discrete transitions. This transition from particle to molecular behavior appears at approximately 1.5nm in AuNPs [88, 89]. This dissertation will study nanoparticle sizes at the edge of this transition with a lower limit of 1.9nm and upper limit of 20nm diameter. Above this regime, >20nm, the magnitude of the plasmon increases with volume but the relative shape of the spectral peak remains constant. This is a result of the real component of the dielectric, scattering by the particle, beginning to dominate the extinction spectra [11, 16, 17]. But as nanoparticle size decreases towards the lower end of this size regime, a broadening of the LSPR band is observed, illustrated in Figure 1.3b. Size-dependent LSPRs are a critical observation. For all energy transfer models to be discussed in this dissertation, a resonance condition must be met for the size-dependent extinction spectra, as the shape of the acceptor's wavelength-dependent absorption will affect its resonance condition in the energy transfer process.

## **1.2 Energy Transfer**

Energy transfer has developed into a variety of techniques, such as; Förster Resonance Energy Transfer (FRET) [21, 22], Lanthanide Resonance Energy Transfer (LRET)[23, 24, 25], Chemiluminescence Resonance Energy Transfer (CRET)[26], Bioluminescence Resonance Energy Transfer (BRET) [27, 28], single particle FRET (sp-FRET) [29, 30], and Nanometal Surface Energy Transfer (NSET) [31, 32, 33]. These techniques have been used as molecular beacons, rulers, and sensors. All of them utilize a resonance between the donor's emission and the acceptor's absorption spectra. For all these resonant energy transfer techniques (all the RETs) the donor emission is higher energy than the absorption features in the acceptors that the energy is being transferred to, and is represented in the model as a J-overlap integral, which will be discussed later in this chapter.

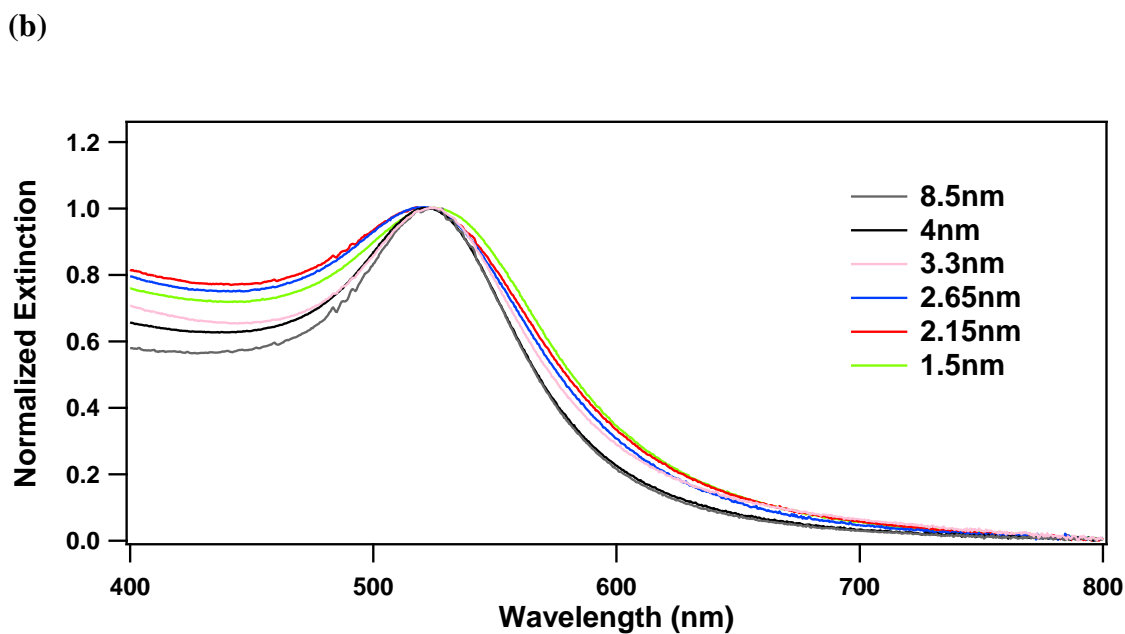
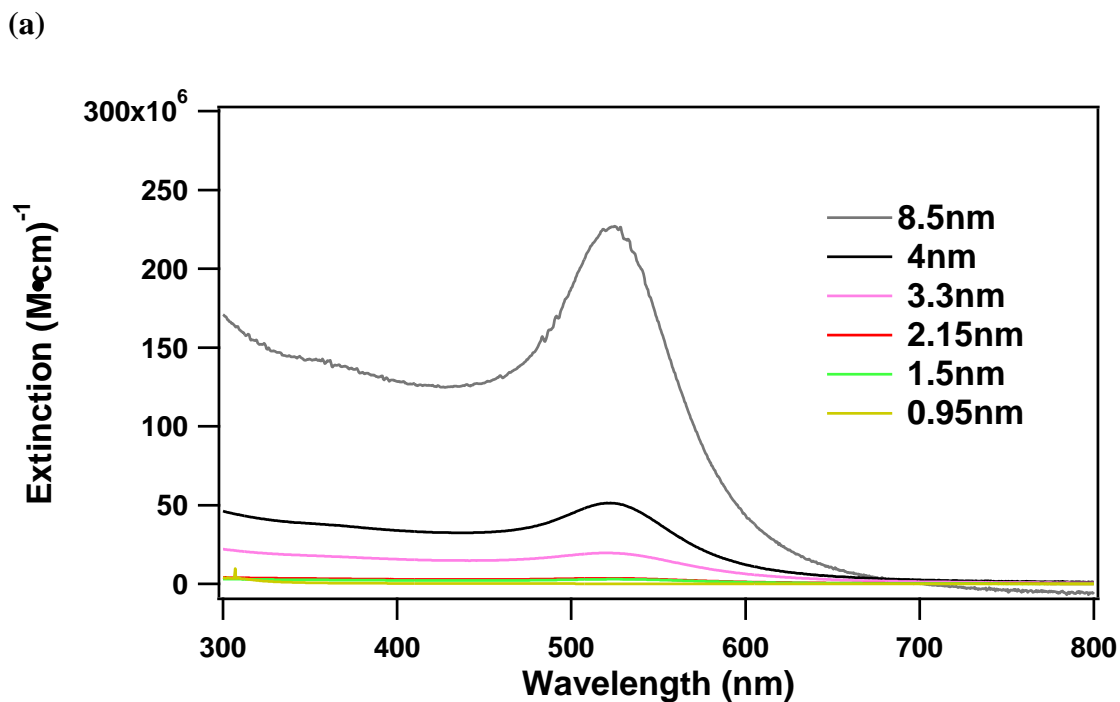


**Figure 1.3** (a) Shows the extinction spectra of AuNPs with different radii. (b) Normalized absorption spectra of the AuNPs illustrating a broadening with decreasing radii

In NSET, however, while a resonant condition is met, the emission energy of the excited state donor is generally lower in energy than the LSPR band. Thus, it is not calculated into the model. Researchers have attempted to explain the coupling of oscillating dipoles to the LSPR of metal nanoparticles in the past, yet varying observations were obtained, presumably due to differences in experimental design. For instance, in work with “larger” particles, diameter > 20nm, enhancement of the emitting dipoles has been observed, whereas below this size regime, quenching of the emission has been observed [34]. It is important to reiterate that this dissertation concentrates entirely in the very small cluster regime where only quenching has been observed. Even when excluding the enhancement-prone particle sizes, there still exists a multitude of theoretical models attempting to explain experimental energy transfer observations, but these theories show little correlation to experiment [5, 6, 7, 8]. In general though, most theories gauge their energy transfer efficiency by a given separation distance between the donor and acceptor that results in a 50% quenching efficiency, represented as either  $R_0$  or  $d_0$ . While all theories typically utilize the general  $R_0$  or  $d_0$  value, significant differences amongst the theories arise when a  $1/d^6$  or  $1/d^4$  energy transfer dependence is observed. These models sometimes result in very similar  $d_0$  values even though the assumptions they make are very different. The difference between these two efficiency curves is not dramatic from an experimental point of view. For this reason it is very important to ensure uniform distance separation between the donor and acceptor when designing experiments, as this information will eventually be used to develop theoretical models contingent on experimental accuracy. Figure 1.4 illustrates the expected efficiency curves for two different theories that result in the same  $d_0$  value but differ in

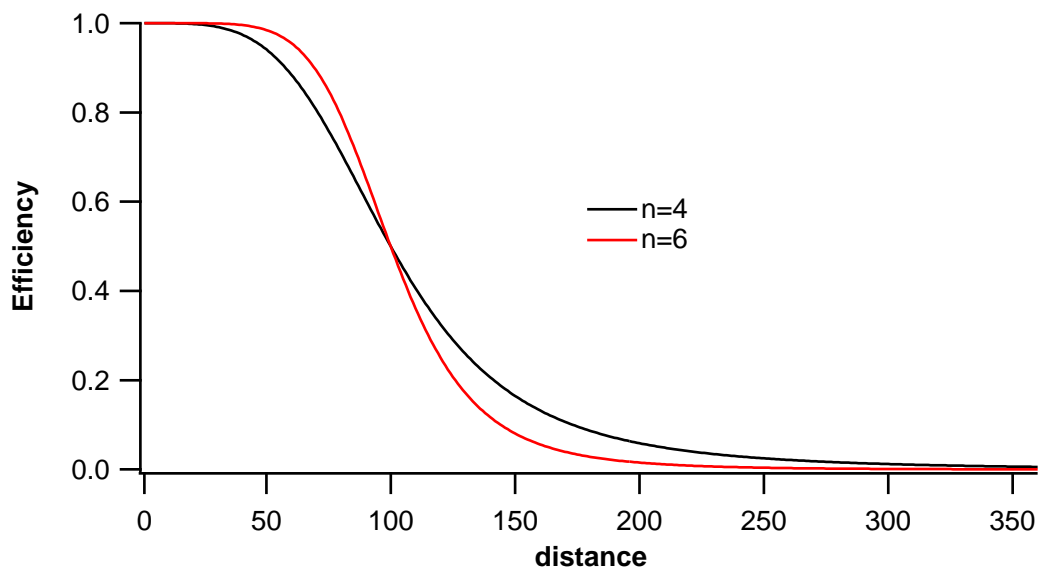


**Figure 1.4** Illustrates the differences in quenching efficiencies for two models predicting different power dependence

their power dependence. It is easy to see that even a 10% deviation in donor-acceptor distance could cause data misinterpretation for the development of a working energy transfer model.

This study will represent the 50% quenching value as  $d_0$  to avoid confusion with the term for radius,  $r$ . Efficiency curves are generally useful and plotted with the  $d_0$  values calculated from the respective theory and equation (1.3)

$$E_{ff} = \frac{1}{1 + \left(\frac{d}{d_0}\right)^n} \quad (1.3)$$

where  $d$  is the distance between the donor and acceptor,  $d_0$  is the 50% quenching distance, and  $n$  is the power dependence of the theory used to describe  $d_0$ . Next a brief history of energy transfer model and the assumptions of the respective models is given.

### 1.2.1 A Brief History

Förster published the first theory on energy exchange between two emitting dipoles in 1948. His corrected theory, dubbed Förster Resonance Energy Transfer (FRET), is given in

equation (1.4) [21]. This theory explained the interactions between two oscillating zero point dipoles at fixed distances apart that are in resonance.

$$d_0 = \left( \frac{9000(\ln 10)\kappa^2 \phi_D J(\lambda)}{128\pi^5 N_A n_m^4} \right)^{1/6} \quad (1.4)$$

$\Phi_D$  is the quantum yield of the donating dipole,  $n_m$  is the index of the medium separating the two dipoles.  $N_A$  is Avogadro's number and  $J(\lambda)$  represents the absorption overlap of the accepting dipole with the emission of the donor dipole, also known as the J-integral given as  $J(\lambda) = \int f_D(\lambda)\epsilon_A(\lambda) \lambda^4 \delta\lambda$ .  $f_D(\lambda)$  is the emission spectra normalized to quantum yield of the donor, and  $\epsilon_A(\lambda)$  is the extinction spectra of the acceptor. An example of the J-integral is shown in Figure 1.5b as the yellow shaded area under the emission of fluorescein (FAM) and the absorption spectra of carboxytetramethylrhodamine (TAMRA). The J- integral defines the magnitude of the resonance condition between the excited state dipole and the ground state accepting dipole. In this model  $\kappa$  represents the orientation between the two dipoles and is generally considered to be  $2/3$  for a freely rotating dipole at random orientations but has an upper limit of 4 for perfectly aligned dipoles, and a lower limit of 0 for perpendicular dipoles. The random orientation assumption is most often used because the dipoles in question are allowed to rotate freely in space, and their emission measurements are ensembles of large populations with no feasible way of controlling this orientation. Figure 1.5a illustrates the orientations between two dipoles and their resulting  $\kappa$  values. The illustration of (a) iv) represents a dipole rotating freely in space.

FRET set an important precedent for energy transfer models to come by classifying the energy transfer process as a nonradiative pathway for the relaxation of the excited state energy transferred to the ground state of the accepting dipole. This theory has been successfully used to

study countless biological systems [35, 36, 37]. While it has proven useful in many application, the primary limitation of FRET is the  $1/d^6$  distance dependence, which results in a maximum measurable distance of 80Å. By changing the accepting dipole to a metal, the distance dependent term is altered, extending the measurable distances passed the FRET limit.

Kuhn attempted to explain the energy transfer from a dipole to a thin metal film in 1970. [38] He treated the film as an absorbing mirror and correctly predicted the  $1/d^4$  distance dependence but over predicted those distances. In his model the metal is assumed to be a strongly coupled sea of dipoles. This was appropriate as the films he was describing were metals and the strongly coupled electrons represented as free electrons in the conduction band. Chance, Prock, and Silbey later added a correction factor to Kuhn's model to incorporate the dielectric functions of the metal film and the separating medium, the resulting model of which will be termed CPS-Kuhn. With this correction term Chance, Prock, and Silbey had great success correlating theory to experimental observation with thin silver films [39, 40]. The corrected theory is given in equation 1.5

$$d_0^{CPS-Kuhn} = \frac{\alpha\lambda}{n_m} (A\phi)^{1/4} \left[ \frac{n_r}{2n_m} \left( 1 + \frac{\epsilon_1^2}{|\epsilon_2|^2} \right) \right]^{1/4} \quad (1.5)$$

where  $\alpha$  is a new orientation factor and is solved for a dipole oriented perpendicular to the surface of the metal film,  $\alpha = \frac{(9)^{1/4}}{4\pi}$ , and parallel  $\alpha = \frac{(9/2)^{1/4}}{4\pi}$ . Figure 1.6 illustrates the two orientations for which the model has been solved. The black dipole is oriented perpendicular while the red dipole and the dipole along the y-axis are parallel.

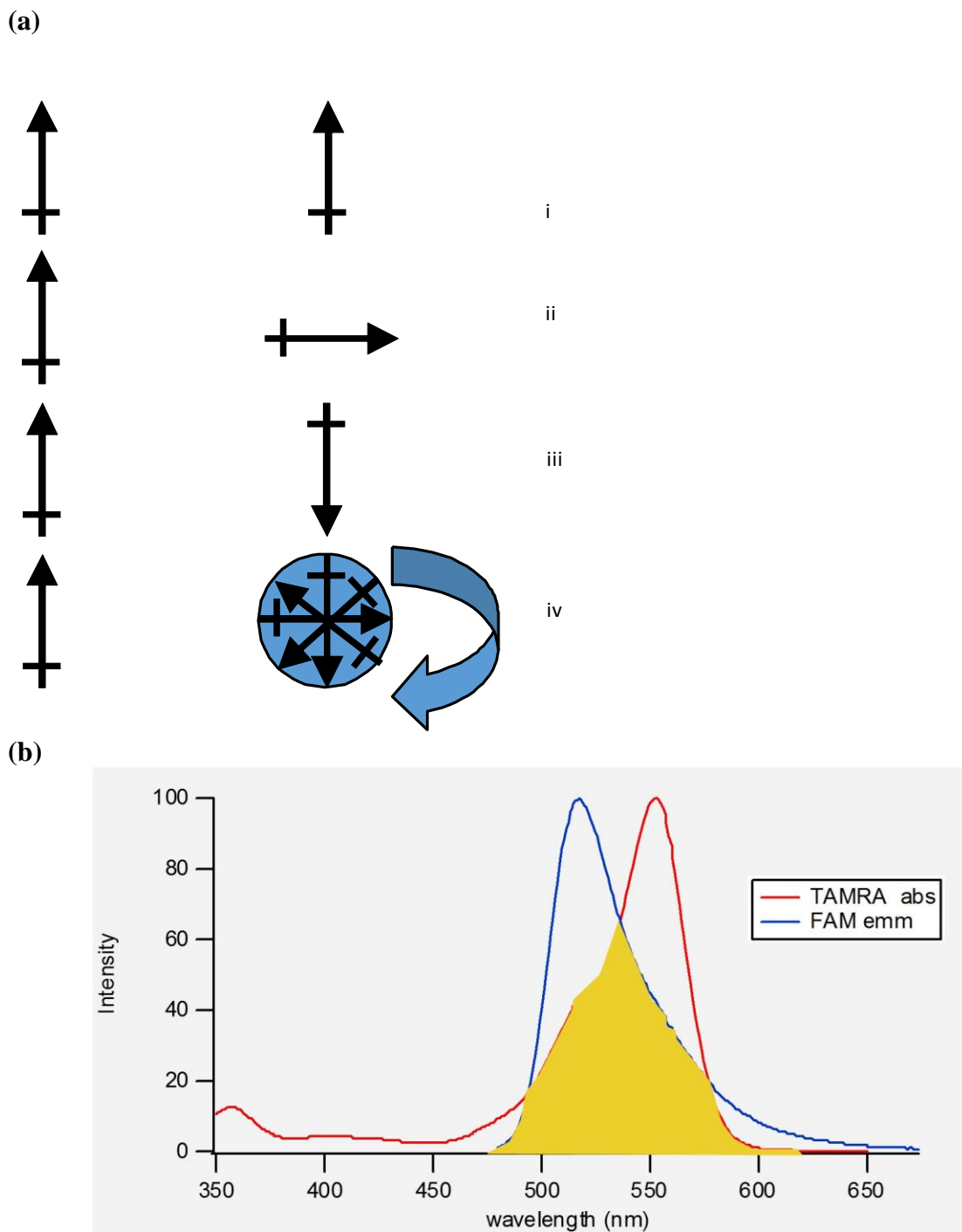


**Figure 1.5** (a) Illustrations of the different orientations the acceptor and donor dipoles can have, their corresponding  $k^2$  values for the FRET calculation are as follows i)  $k^2=1$ , ii)  $k^2=0$ , iii)  $k^2=4$ , iv)  $k^2=2/3$ . (b) Represents the J-integral for a FRET pair of fluorescent dipoles with FAM (donor) and TAMRA (acceptor)

The two parallel dipoles along the x and y-axis are degenerate, while the black dipole on the z-axis is not. This degeneracy results in a (2/3):(1/3) split in the coupling efficiency for an ensemble system with freely rotating dipoles.  $\lambda$  is the wavelength of emission of the donating dipole,  $n_m$  is the index of refraction of the medium between the dipole and the metal film,  $A$  is the absorptivity of the metal film given as  $A=4\pi\kappa d/\lambda$  where  $\kappa$  is the extinction of the metal reported by Johnson and Christie [41], and  $d$  is the thickness of the metal film.  $\Phi$  is the dipole quantum yield, and  $n_r$  is the refractive index of the metal. Finally  $\epsilon_1$  is dielectric of the medium separating the dipole and metal. This is a commonly mislabeled variable as there is some confusion in the literature which causes many researches to interpret it as the real component of the dielectric function of the metal. Upon thorough investigation of the original manuscript by Chance, Prock and Silbey it is clear that they meant it to be the complex dielectric function of the separating medium. That leaves  $\epsilon_2$  as the complex dielectric function of the metal. CPS-Kuhn theory was shown to work remarkably well for thin metal films but quickly breaks down when applied to nanoparticles. The reason for this will be discussed in Chapter Three [39, 40].

Around the same time as CPS-Kuhn was being modified for thin films, Gersten-Nitzan developed a model attempting to explain the interaction between an oscillating dipole and a metal nanoparticle. In their model they assumed the nanoparticle to consist of a volume of uncoupled dipoles. This assumption results in a  $1/d^6$  distance dependence as the donating dipole couples to a single dipole in the volume of oscillators present in the metal nanoparticle.

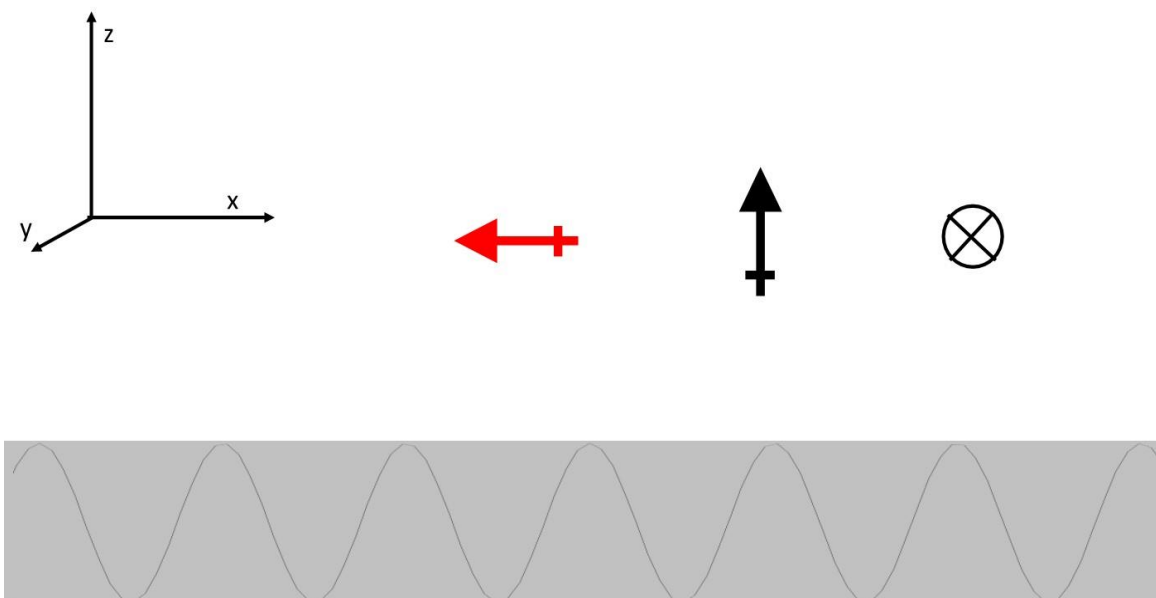


**Figure 1.6** Illustrates the orientations the CPS-Kuhn model is solved for. The red dipole along the x-axis, and the circle with an “X” in it represents a dipole along the y-axis are both parallel to the metal film and the black dipole along the z-axis is perpendicular

The  $d_0$  equation for the Gersten-Nitzan model (G-N) is given in equation (1.6)

$$d_0 = \left( 2.25 * \frac{c^3}{\omega_{dye}^3} \phi_D r^3 \frac{(\epsilon_1 + 2)^2 + \epsilon_2^2}{|\epsilon_2|^2} \right)^{1/6} \quad (1.6)$$

where  $c$  is the speed of light,  $\omega_{dye}$  is the frequency of maximum emission of the donor,  $\phi_{dye}$  is the quantum yield of the donor,  $r$  is the radius of the accepting nanoparticle, and  $\epsilon_1$  and  $\epsilon_2$  are the real and imaginary components of the dielectric function of the acceptor (metal nanoparticle).

With a more contemporary modeling system by the incorporation of nanoparticles, this model has gained traction in the field. Though several modifications have been made in an attempt to more accurately fit experimental energy transfer data, the attempts have seen little success. G-N has had reasonable success in calculating the  $d_0$  value but a distance dependence prediction of  $1/d^6$  does not match experimental observations. Figure 1.7 illustrates the assumptions the G-N model makes. The nanoparticle can be considered a volume of dipoles each of which can couple

to the donor. This volume of dipoles within the nanoparticle is assumed to be uncoupled and therefore the efficiency of coupling to the donor follows the same distance dependence as FRET. Because the volume of dipoles has all possible orientations, the orientation factor in FRET is no longer needed. Overall, this model predicts more efficient quenching behavior than FRET simply because the increased number of accepting dipoles increases the probability of coupling.

Persson and Lang described the interaction between a dipole and an infinite surface [42]. As written, their model was not able to accurately portray the interaction between dipoles and nanoparticles. Strouse, et al successfully modified the surface component of the Persson and Lang model to correctly incorporate small nanoparticle with great success and dubbed the new model nanometal surface energy transfer (NSET). The NSET model showed that it held true for predicting interactions between 2nm AuNPs and a range of emission frequency [31].

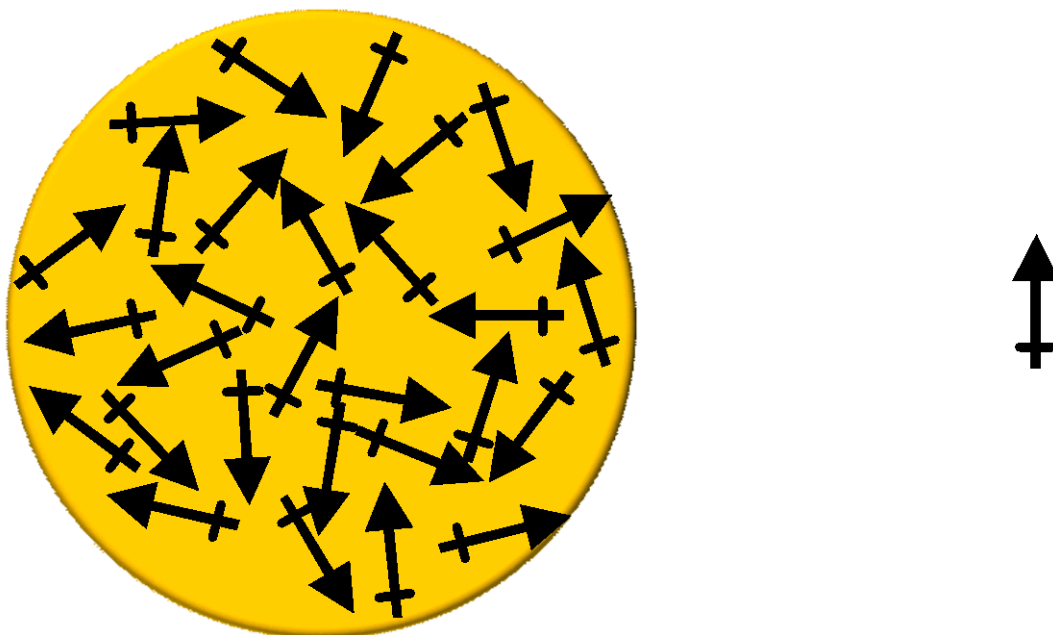


**Figure 1.7** A volume of uncoupled dipoles, in the metal nanoparticle, with all possible orientations couple efficiently to a donor dipole at a set distance from the particle.

While this model correctly describes 2nm AuNPs, where the largest surface to volume ratio for gold nanoparticles is observed, the model fails quickly as nanoparticle size increases. As noted previously, nanoparticles smaller than 2nm begin to behave like molecular clusters and lose the LSPR band, invalidating the NSET theory at sub-2nm AuNP sizes. By treating the particle as a surface, NSET correctly predict the  $1/d^4$  behavior observed experimentally for 2nm AuNPs [31]. The model is given in equation 1.7

$$d_0^{NSET} = \left( 0.225 \frac{\varphi_D * c^3}{\omega_{dye}^2 \omega_f \kappa_f} \right)^{1/4} \quad (1.7)$$

where  $\varphi_D$  is the quantum yield of the donor,  $c$  is the speed of light,  $\omega_{dye}$  is the frequency of emission of the dye,  $\omega_f$  is the Fermi frequency of the metal nanoparticle, and  $\kappa_f$  is the Fermi wave vector of the metal. The assumptions for NSET are represented in Figure 1.8 with the dipoles in the metal nanoparticle being coupled but still containing all the orientations to increase the probability of coupling to the donor dipole at a distance from the surface of the particle. NSET also assumes the dipoles that couple to the donor are located at the surface of that particle. Unfortunately this model fails quickly once the size of the nanoparticle begins to increase. Solving the inconvenient problem of NSET's failure above the 2nm AuNP size regime will be discussed in chapter three.

### 1.2.2 State of the Art

Each model used to describe the energy transfer process incorporates terms from the donor and the acceptor. It is the limitations, and subsequent assumptions, that each model places on those terms that set them apart from one another. As stated earlier in equation 1.4 the  $d_0$  for FRET depends on the orientation between the two dipoles, the quantum yield of the donor, the index of refraction of the medium separating the dipoles and what is known as the J-overlap. This J-overlap is unique in energy transfer models and has been extensively studied [10].

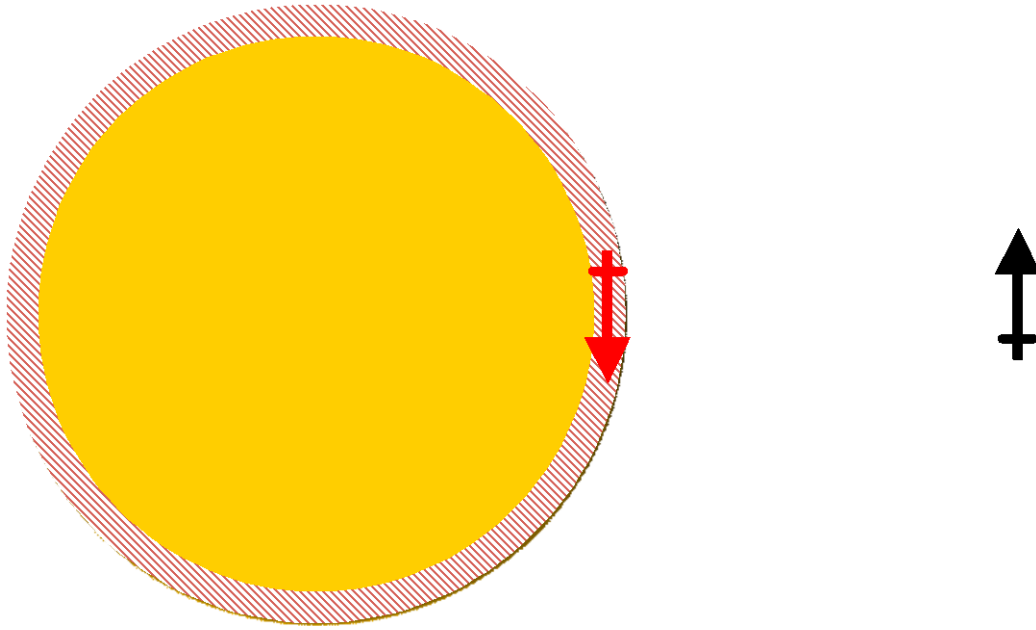


**Figure 1.8** A surface of strongly coupled dipoles couples to an oscillating dipole a set distance from that surface

More than half a century after its development FRET remains the primary model used in describing interactions between two oscillating dipoles. Recently with the development of more sensitive optical techniques scientists have been able to take single molecule measurements. This breakthrough has allowed for the development of single molecule FRET. With this new extension of FRET, scientists have been able to distinguish single molecule events from ensemble measurements. This is an important development in science because it has allowed scientists to investigate conformational changes of proteins in real time [35].

### 1.2.3 Applications and Limitations

FRET is the most widely used technique of energy transfer and has given rise to specific uses. Bioluminescence resonant energy transfer (BRET) utilizes fluorescence in biological systems as the donating dipole, usually a fluorescent protein such as GFP [28, 29]. In most applications of BRET a binding molecule is modified with a fluorescent dye that will participate

in FRET with the fluorescent protein. As the protein is excited it transfers its energy to the now bound accepting dipole and the technique extracts out structural information measures the signal from the dye.

Chemiluminescent resonant energy transfer (CRET) incorporates molecules that can be chemically excited, typically by reducing agents, and give off a photon during the relaxation of the excited state to act as the donors. By incorporating a chemiluminescent donor, CRET allows researchers to investigate traditional FRET problems without the use of incident light, permitting experimentation in high scattering environments that would normally be difficult to accomplish by other means. Lanthanide resonant energy transfer (LRET) utilizes the narrow line emission of lanthanides as donors [24, 26]. This dramatically decreases the amount of cross talk between the donor and acceptor emission.

NSET has been utilized in biology to track events in cellular uptake, conformational changes, and payload delivery into cells [19, 108, 22, 68, 53]. AuNPs are labeled with fluorescent payloads, transfected into cultured cells, and as the payload is released from the nanoparticle surface inside the cell, the fluorescent signal turns on as it diffuses from the quenching AuNP. This has been used almost exclusively as an “on/off” system with the payload-bound as the “off” state and the released payload as the “on” state. NSET has also been utilized to track binding events such as small molecules binding to aptamers [109]. Similarly, this technique is exclusively “on/off,” with the unbound aptamer as the “off” state by a fluorescently-labeled base pair within quenching distance to the AuNP, and the target-bound aptamer “on” state with a label farther away from the AuNP. Once the small molecule has bound to the aptamer the system turns “on” by either releasing a complimentary strand containing the fluorescent base, or the label is moved away from the AuNP via folding of the aptamer. Again,

no distal calculations are performed using NSET measurements because there is a lack of understanding of non-2nm AuNPs' ability to quench fluorophores. The Strouse group is one of few that has attempted to use this model to track structural changes by mapping the folding of Hammerhead RNA. This was performed by labeling hammerhead RNA with 2 different fluorescent dyes and a 1.5nm AuNP. The quenching efficiency of each dye was subsequently monitored as the RNA was induced to fold by varying salt concentrations [19].

### **1.3 Summary of Chapters**

This dissertation will focus on energy transfer between metal nanoparticles and fluorescent molecules. A cohesive model will be developed that incorporating size dependent factors of nanoparticles that have not been considered until now. Chapter Two will discuss the synthesis of metal nanoparticles that were used for the energy transfer studies and will also give details about the synthesis of some other interesting materials. Chapter Three will present an all-encompassing model to explain the size dependent quenching behavior of fluorescent dipoles by AuNPs. Moreover, Chapter Three will include a discussion of the evolution of two models, CPS-Kuhn and NSET, joined to form the CPS-NSET model. Enhanced quenching of high energy dyes will be interrogated and discussed in Chapter Four.

# **CHAPTER TWO**

## **SYNTHESIS OF METAL NANOPARTICLES AND METAL OXIDES**

### **2.1 Introduction**

In order to study the electromagnetic interactions of light with nanoparticles, it is imperative to be able to produce those particles. There are many methods in the literature, each with slight variations resulting in slightly different material [89-95]. This chapter will describe the various techniques employed to prepare and characterize these nanoparticles.

A basic understanding of nanoparticle nucleation is required to choose the most appropriate synthetic method for each nanomaterial. Nanoparticles can be prepared using engineered approaches or by condensation from the gas phase [96], both of which will not be discussed in this chapter. In general, there are two traditional approaches to form nanoparticles. First there is the top down approach, where mechanical processing is used to reduce bulk dimensions to nanosize by breaking down the material until the desired scale is achieved. The most primitive mechanical method used is ball milling, where the desired material is set into a chamber with debris of harder material and that chamber is violently rotated to break up the material into smaller and smaller pieces [43]. Mechanical methods do not yield uniform particles with well-formed structural features or faceting. The most substantial benefit for ball milling is the ease of use it offers researchers.

On the other hand, bottom up chemical synthesis of nanoparticles differs greatly from the top down mechanical method, offering essential shape control, stability, and well-formed features. Chemical synthesis of nanoparticles is essentially the polar opposite of the mechanical

method. Where mechanical methods begin with bulk, chemical synthesis begins with either molecular or even atomic precursors. Solution based, opposed to gas phase, chemical synthesis is more common and will be the subject of discussion hence forth [96].

### 2.1.1 Nucleation

Figure 2.1 illustrates the basic principle of nucleation. Chemical formation of metal nanoparticles begins with formation of critical nuclei from metal ion precursors containing metal ions. The ions are reduced with a reducing agent generating a nuclei where growth exceeds dissolution. The size of the critical nuclei is material and structural dependent. Typical reducing agents for metal nanoparticle synthesis are sodium borohydride, ethanol, and a combination of citric acid and tannic acid. Borohydride reactions are exothermic, while citrate requires elevated temperatures to achieve reducing conditions [44, 96]. After being reduced the ions, now atoms, are thought to form monomers of what are known as critical nuclei, which in turn form polymers. If these polymers are left unchecked they will continue to grow to bulk. In order to prevent growth beyond the nanoscale, passivation of the surface is required [45].

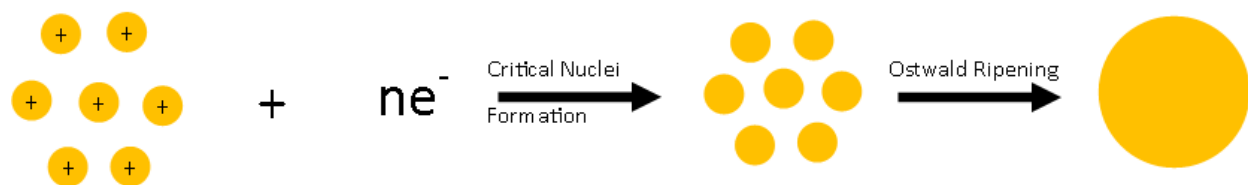


**Figure 2.1** Principle of nucleation. First ions (yellow balls with + signs) are reduced with electrons and form monomer (plain yellow balls) that grow into bulk (large yellow ball)

### 2.1.2 Passivation

The size and shape of nanoparticles isolated from a synthesis are determined by the concentration of reactants and the passivating ligands in solution. The size of the particles is controlled by the ligands to nuclei ratio, with a larger ratio resulting in smaller nanoparticles.

This is due to the passivation process that occurs shortly after nucleation. The passivation process depends on the number of nuclei formed during nucleation which is a function of the precursor concentration. The critical nuclei that form after ion reduction quickly begin to grow. If left unchecked these critical nuclei will continue to grow into bulk. By introducing surfactants that compete for the binding sites on the surface of the growing nuclei with the reduced atoms, researchers can prevent cascade of growth to bulk [46]. These surfactants, or ligands, form covalent bonds with the surface atoms and undergo an equilibrium process between the bound and the unbound states. Using a high ligand to precursor ratio it is possible to shift the equilibrium to obtain fully passivated nanoparticles. The covalent bonds that the ligands form obey the same ligand field rules utilized in metal coordination compounds [46]. For the studies to follow on AuNPs phosphines will be used as stabilizing ligands, while harder acid metals will utilize amines. The choice of phosphine for AuNPs reflects the instability of acid functionalized ligands and the desire to be able to exchange payloads onto the surface via stronger ligand groups; namely thiols and dithiols [45, 46].

## **2.2 Metal Nanoparticle Synthesis**

### **2.2.1 Water Soluble Methods**

**Method 1:** The standard citrate reduction method was used for synthesis of AuNPs larger than 2nm in diameter. For this procedure, 1 mL of a 1% solution by mass of  $\text{HAuCl}_4$  was diluted to 80mL of degassed water and heated to 60°C. Simultaneously, 4mL of a 1% solution by mass of sodium citrate and X mL of 1% by mass tannic acid were mixed and diluted to a total volume of 20mL. The volume of tannic acid varied depending on what size nanoparticles were being synthesized and is given in Table 2.1. This solution was heated to 60°C and then poured quickly into the gold solution. [47]

The reaction is heated for 15 minutes and then cooled to room temperature. 500mg of bis(sulfanoto phenyl)phenyl phosphine (BSPP) is added to this solution to displace the citric and tannic acid on the surfaces, stabilizing the particles from aggregating. This ligand exchange is given 24 hours to complete and particles smaller than 8nm were washed by salting out with 6M NaCl and centrifuged down while larger particles did not need salt for centrifugation.

This method was used to produce AuNPs ranging from 3nm to 20nm in diameter. TEM analysis confirms mean size, narrow size distribution, and good spherical formation. The TEM used to analyze the particles was a FEI CM120 equipped with a tungsten filament running at 120keV. The samples were deposited onto 200mesh formvar coated copper grids. The TEM images for the aforementioned sizes are given in Figure 2.2-2.12.

**Table 2.1** Volume of tannic acid to achieve desired nanoparticle diameter

Nanoparticle diameter (nm)	Volume of Tannic acid (mL)
3	5
4	2.5
6	0.5
7	.25
8	0.175
16	0.025
20	0.005

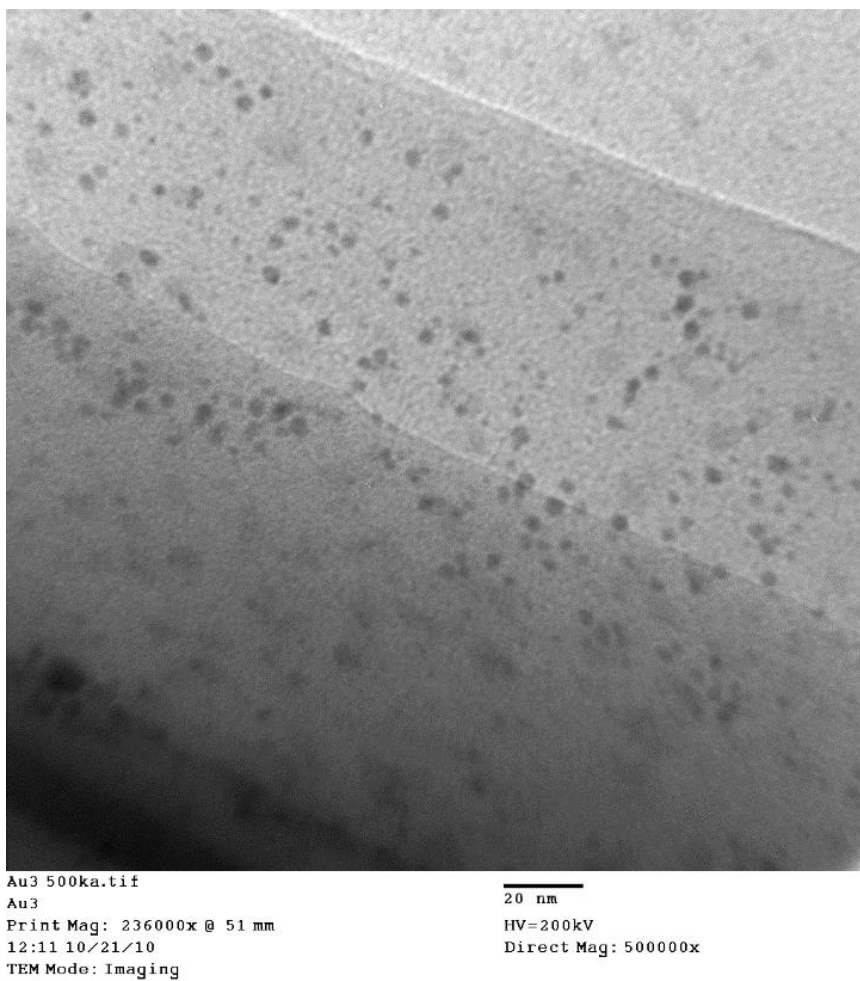


**Figure 2.2** TEM image with size analysis for 3.0nm AuNP showing a standard deviation of 0.6nm. Scale bar in image represents 20nm

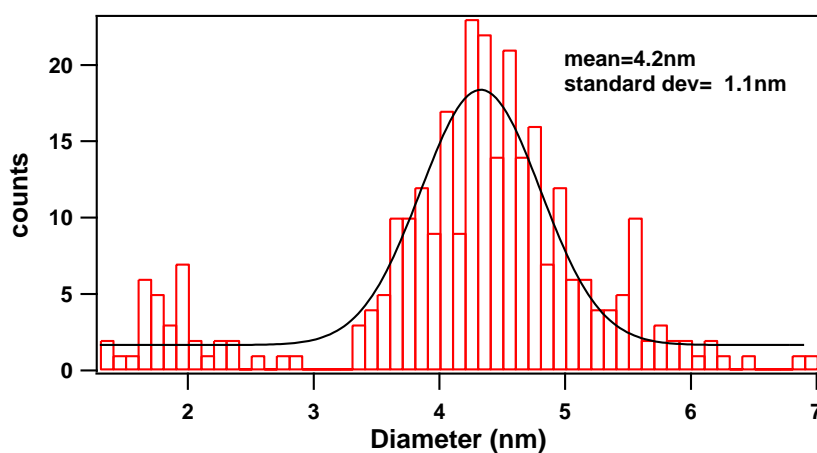
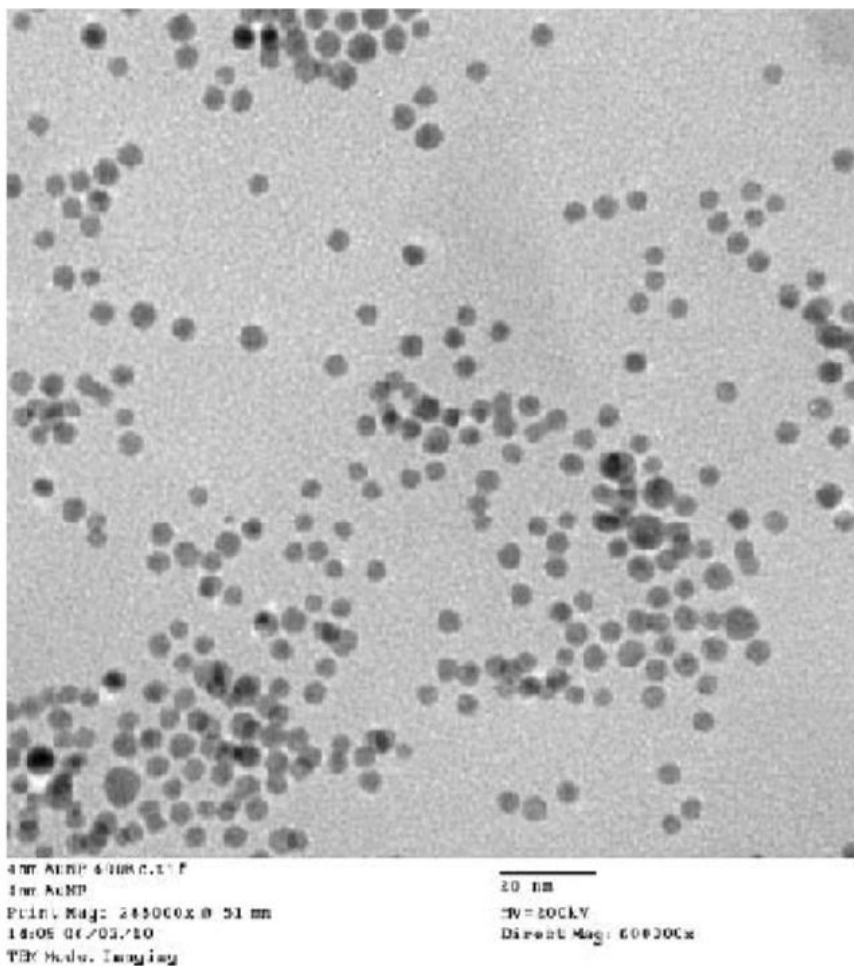


**Figure 2.3** TEM image with size analysis for 4.2nm AuNPs showing a standard deviation of 1.1nm. Scale bar in image represents 20nm

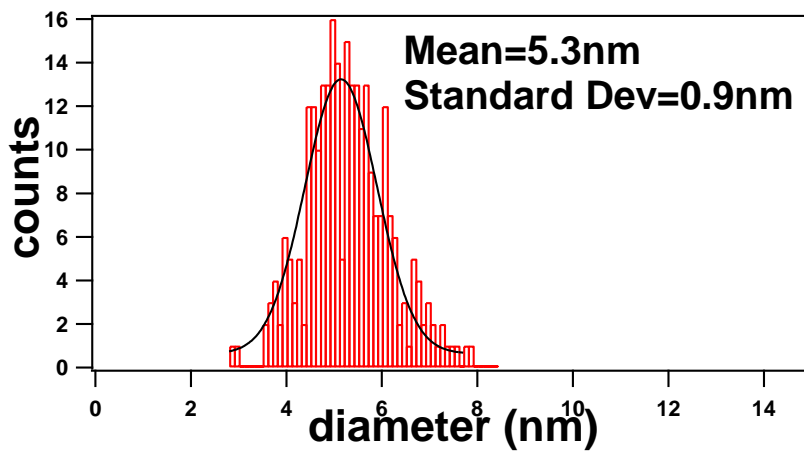
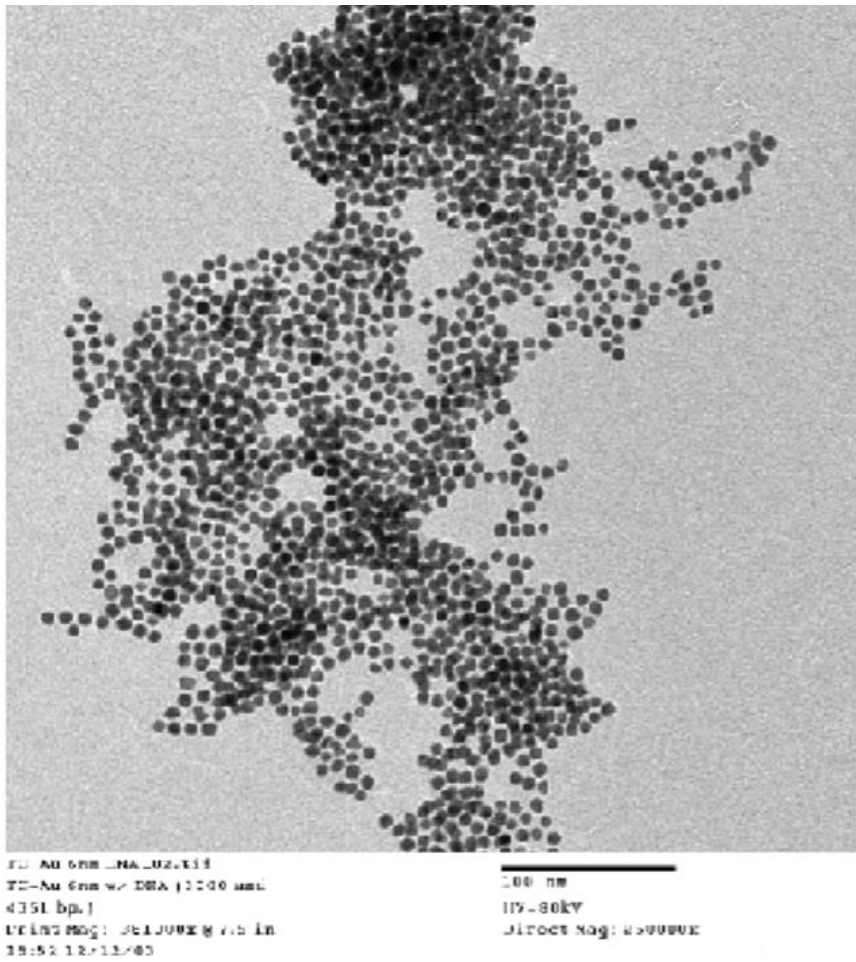


**Figure 2.4** TEM image with size analysis for 5.3nm AuNPs showing a standard deviation of 0.9 nm. Scale bar in image represents 200nm

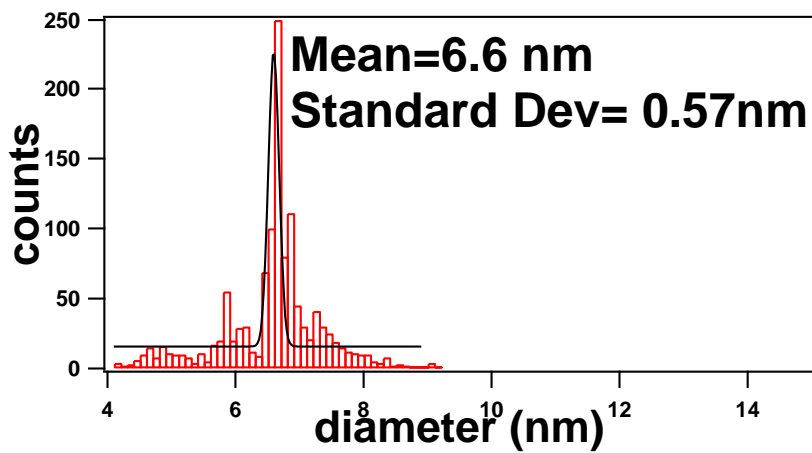
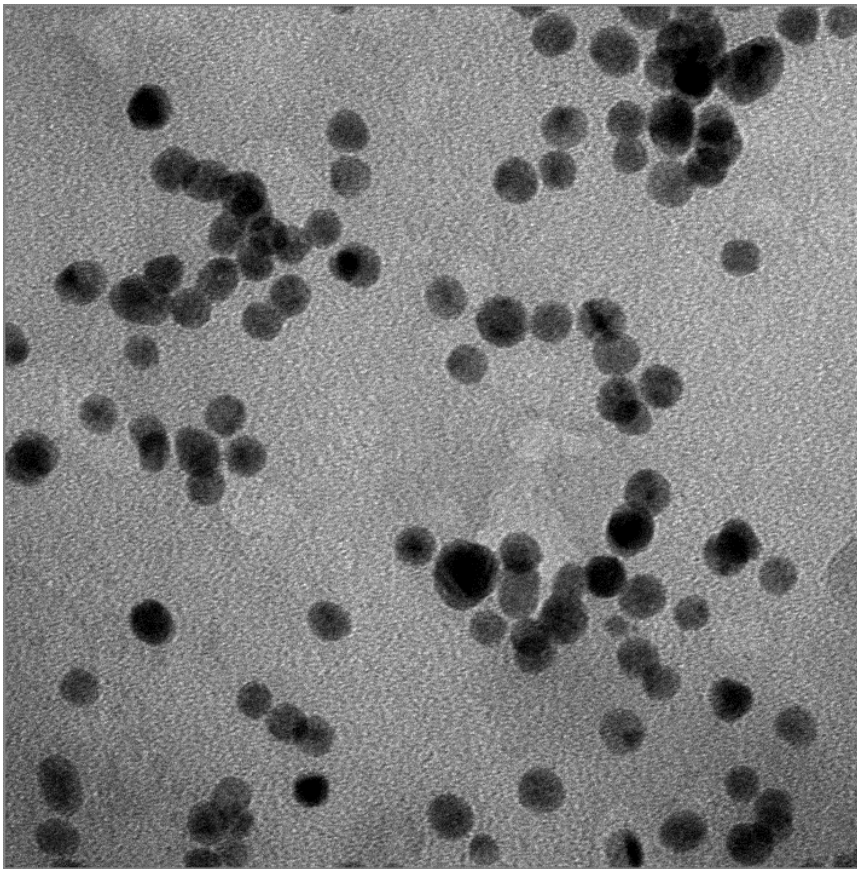


**Figure 2.5** TEM image with size analysis for 6.6nm AuNPs showing a standard deviation of 0.57 nm. Scale bar in image represents 50nm

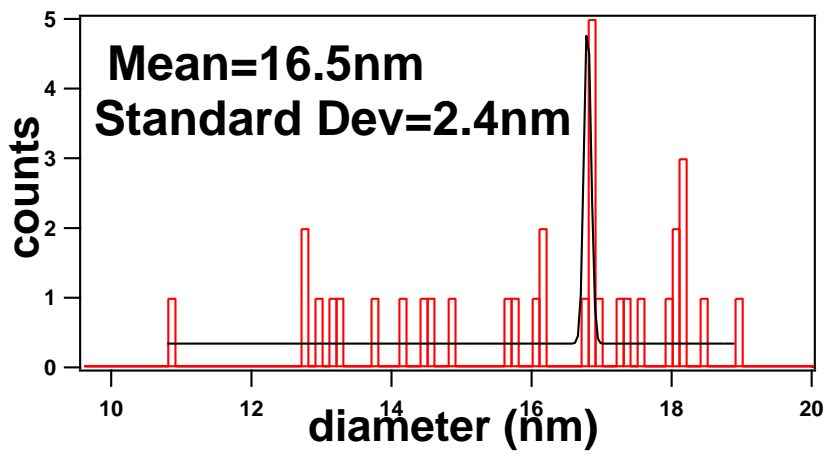
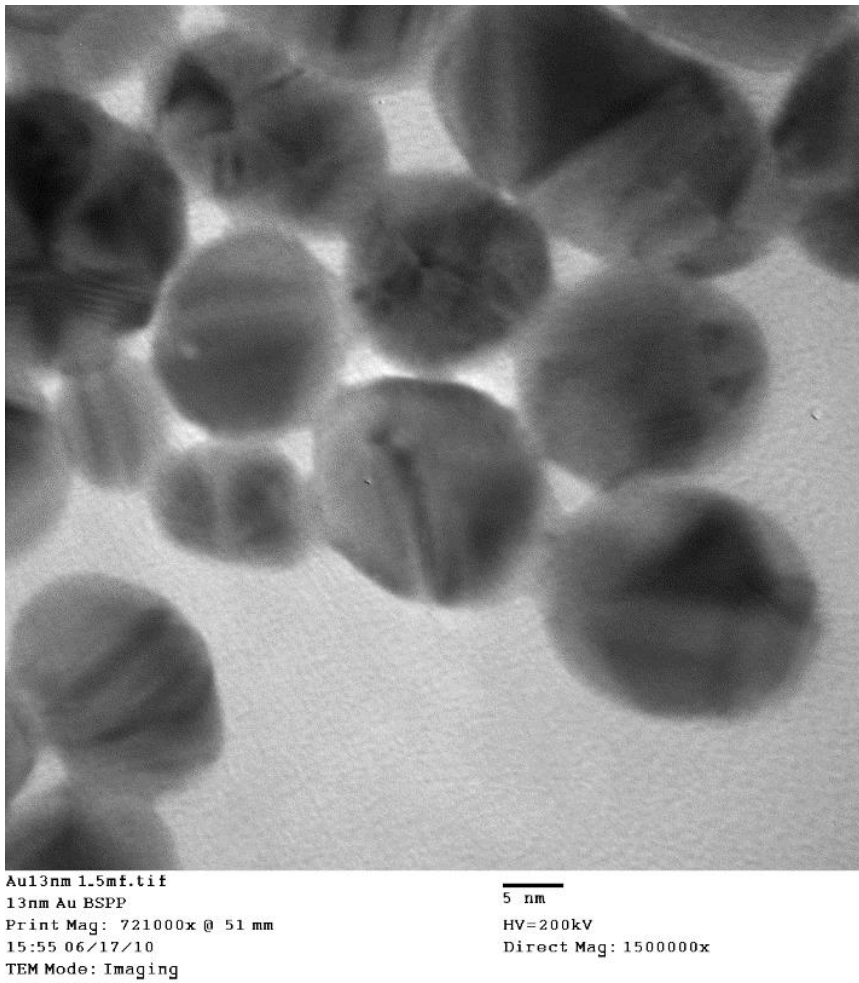
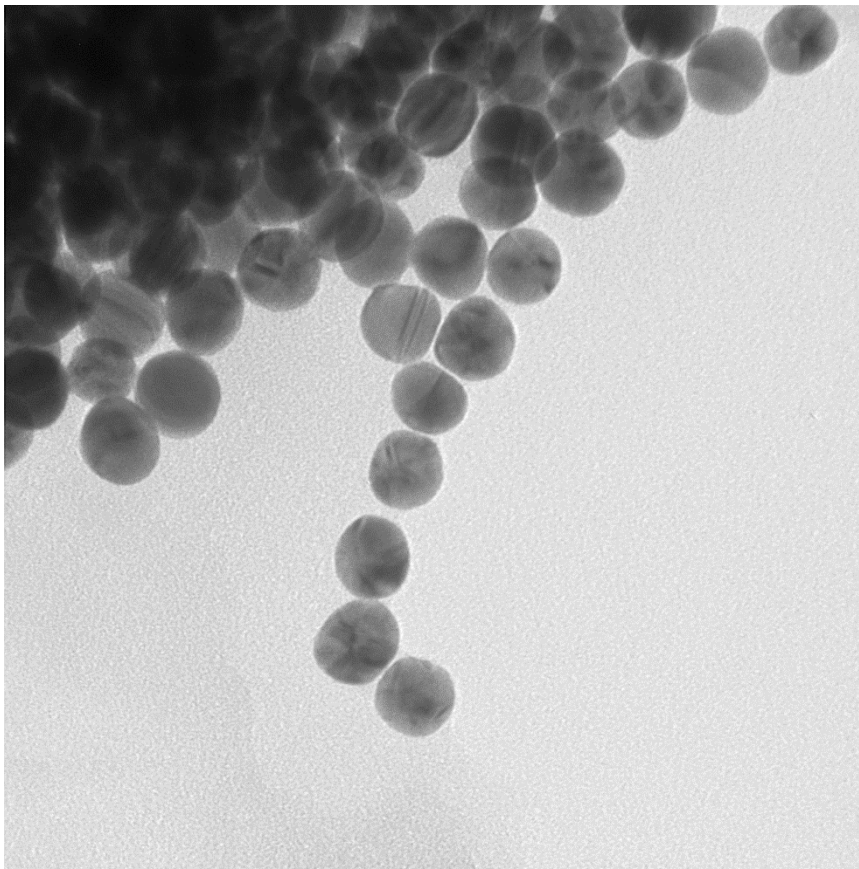


**Figure 2.6** TEM image with size analysis for 16.5nm AuNPs showing a standard deviation of 2.4 nm. Scale bar in image represents 5nm



Au20nmBSPP 500kc good.tif  
20nm Au BSPP  
Print Mag: 240000x @ 51 mm  
14:12 06/17/10  
TEM Mode: Imaging

20 nm  
HV=200kV  
Direct Mag: 500000x

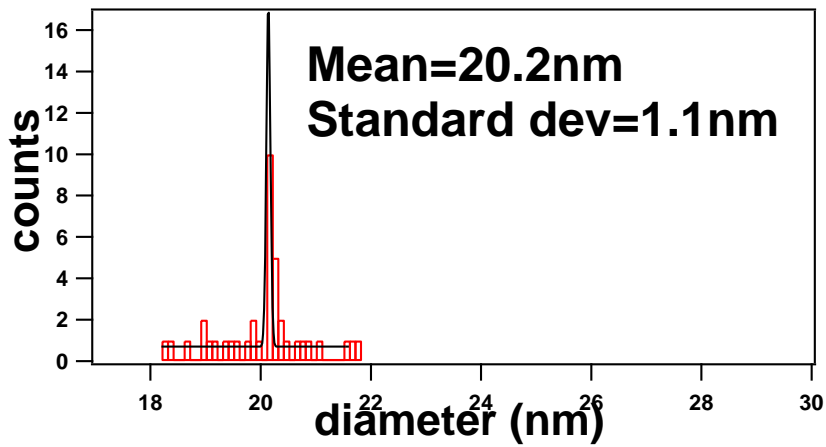


**Figure 2.7** TEM image with size analysis for 20.2nm AuNPs showing a standard deviation of 1.1 nm. Scale bar in image represents 20nm

Figure 2.2 shows a mean size of 3.0 nm with a distribution of 0.6 nm, a 20% dispersity in size. The Gaussian fit over the histogram of sizes encompasses only slightly more than 50% of the particle sizes measured, illustrating the poor size control this method provides for synthesizing smaller nanoparticles. Even with the broad size dispersity there are not very many particles outside one standard deviation of the average, which is desirable for the size dependent studies that will be discussed in Chapter Three.

Figure 2.3 shows a mean size of 4.2 nm with a distribution of 1.1nm, a 26% dispersity in size. From the histogram it is apparent that two populations are present in the sample; a larger population with a mean size of 4.4 nm and a smaller population with a mean diameter of approximately 1.7nm. A potential cause for this size distribution is a lack of extended heating for Oswald ripening to completely dissolve the smaller sizes [97-99]. Before this sample was used in any experiments, the larger population was size selectively precipitated out with the minimum amount of 6M NaCl solution and centrifuged to a pellet, leaving the smaller population left in the supernatant.

Figure 2.4 shows a mean diameter of 5.3nm with a distribution of 0.9 nm which is a 17% dispersity. The Gaussian fit over the histogram illustrates better dispersity of the 3.0nm and 4.2nm particles. There has been better dispersity reported in the literature for AuNP of 6nm and smaller radii synthesized but in general those synthesis result in AuNPs that are capped with a surfactant that is difficult to exchange and therefore the materials produced from these methods are not favorable for any experiment in where DNA or any other payloads are being attached to the surface [100, 46].

Figure 2.5 shows a mean diameter of 6.6nm with a distribution of 0.6nm which is an 8% dispersity. The Gaussian curve fit to the histogram indicates a tight size distribution overall but

there is a very small population of smaller nanoparticles. Again this can be caused by not allowing the reaction to complete. The reason the reaction is sometimes stopped prematurely is that the citrate capped nanoparticles are not stable for very long so BSPP is added as soon as the particles reach room temperature. When the BSPP is added it coordinates to the surface with a higher binding affinity than the citrate and tannic acid [46]. This shifts the passivation equilibrium towards the fully capped nanoparticle, which prevents further growth, as well as aggregation. The minute population of smaller particles is not large enough to effect the standard deviation is size very much and was therefore not required to separated out via centrifugation.

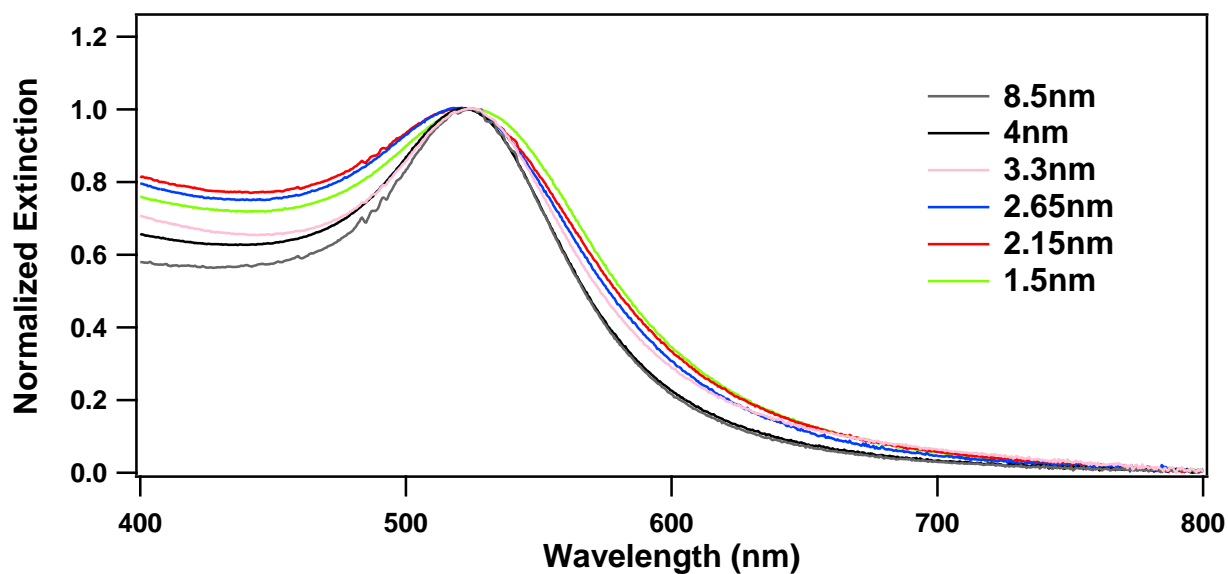
Figure 2.6 shows a mean diameter of 16.5nm with a distribution of 2.4nm which is 14% dispersity. This sample exhibited the largest size distribution. Even though dispersity of the particles is not as large as the smaller particles it is important to note that in general larger particles not only have tighter size dispersity but a good sample will have around 1nm as a standard deviation. This sample's large size distribution is likely due to it sitting in solution for an extended period of time. Even with the BSPP as a stabilizing ligand particles when kept in solution the particles still undergo the equilibrium between bound and unbound ligands and will eventually continue to grow to bulk.

Figure 2.7 shows a mean diameter of 20.2 nm with a distribution of 1.1nm, which is a 5% size dispersity. Upon investigation of the histogram it is clear that this sample has an extremely tight size distribution with only a few outliers. By comparing this sample to the smaller-diameter nanoparticle batches, a general conclusion can be made: as the nanoparticles get larger in diameter, the size dispersity decreases, while the size distribution remains relatively constant in the citrate reduction method of AuNP synthesis.

Along with TEM analysis UV-Vis absorption spectroscopy was done to determine the concentration of the nanoparticles in solution. This is done using the Beer-Lambert law, equation 2.1,

$$A = \epsilon bc$$

Where A is the absorbance measure,  $\epsilon$  is the material's extinction coefficient at a specific wavelength, b is the path length the incident light travels, and c is the concentration of the material being measured [101,102]. Along with concentration the absorption spectra also contains information about size, and shape. Figure 2.13 illustrates the narrowing of the predominant absorption feature of AuNPs known as the LSPR.



**Figure 2.8** Normalized absorption spectra for a range of AuNP sizes

It is interesting to note that the stoichiometric amount of nanoparticles formed in each reaction is inversely proportional to the size of the nanoparticles formed. Because reaction volume and gold ion concentration are constant for all reactions studied here, it is understandable that a constant concentration of gold precursors will form more small nanoparticles than large.

When plotted relative to the size-dependent extinction coefficient, the absorption spectra gives rise to the extinction spectra, given in Figure 2.9a. In order to see the size dependence of the extinction of the AuNPs it is useful to plot the extinction coefficients at the peak of the LSPR at 520nm, illustrated in Figure 2.9b. Clearly, the extinction follows a volumetric trend with an  $r^3$  power dependence. Interestingly, this power dependence broadens into an  $r^4$  power dependence as the extinction coefficient red of the LSPR band is considered. This offers further evidence of the broadening of the absorption spectra and will be important when determining how efficiently the LSPR couples to excited state molecules.

The reaction mechanism for the citrate reduction method is shown in Figure 2.10. In this method the citrate and tannic acid both act as reducing agents as well as surfactants. The passivating group for each of these ligands are the acid functional groups. Acids are ideal for coordinating to gold so the acid passivated AuNPs are not stable for very long or in harsh conditions [46]. The citrate and tannic acid passivated particles are so unstable, in fact, that they cannot be efficiently salt precipitated to separate them from unreacted reagents and smaller-sized nanoparticles. If the reaction is left stirring for more than 24 hours without introducing a more stable surfactant the passivation equilibrium process will lose out to growth and flakes of gold will begin to crash out of solution. The stabilizing ligand choice of BSPP reflects that fact that phosphines are better coordinators to gold than acids but not so good that they cannot be later displaced by ligand exchanging with thiol or dithiol labeled payloads of interest [46].

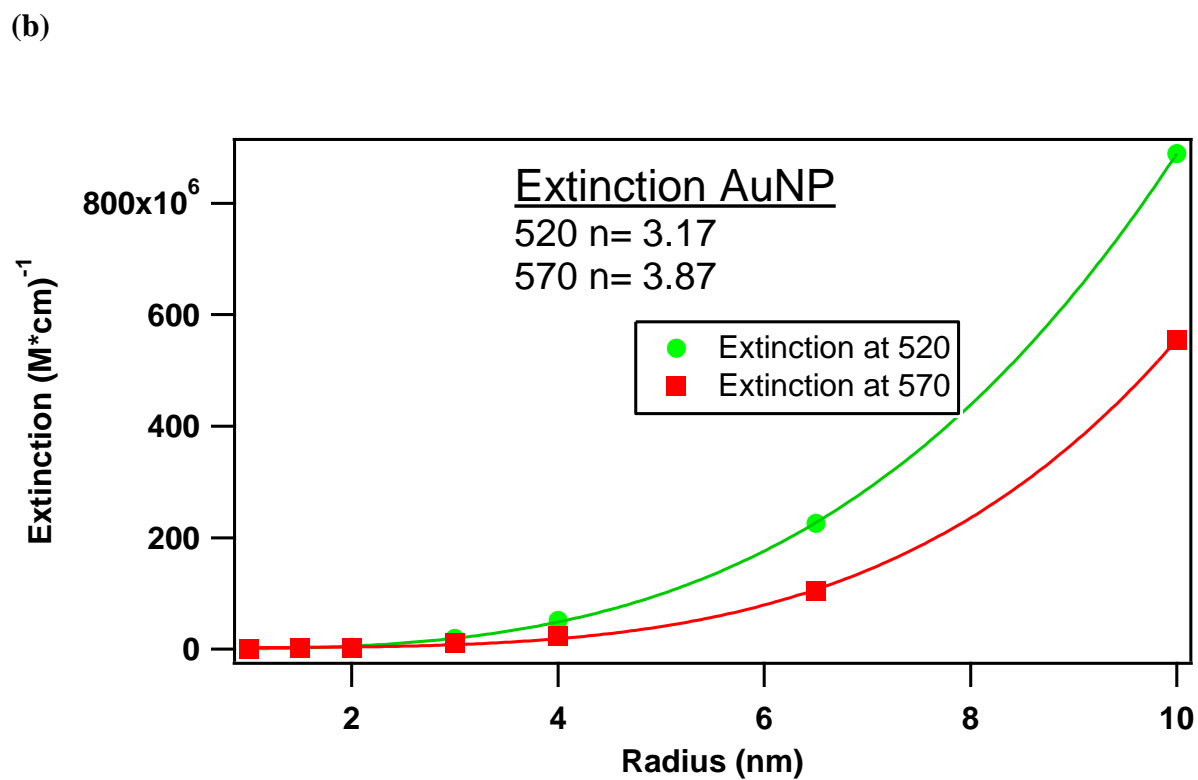
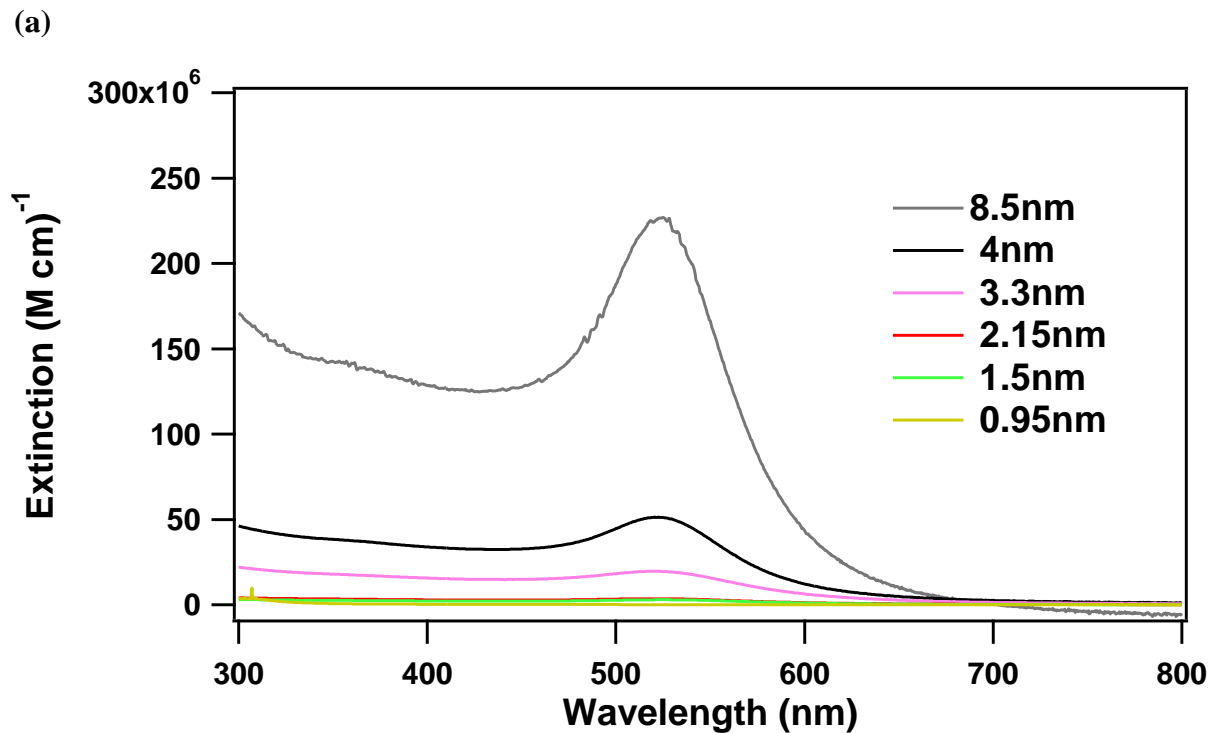


**Figure 2.9** (a) The extinction spectra for various size AuNPs. (b) Plot of the extinction coefficients of the peak absorption at 520 and slightly red of the peak at 570nm

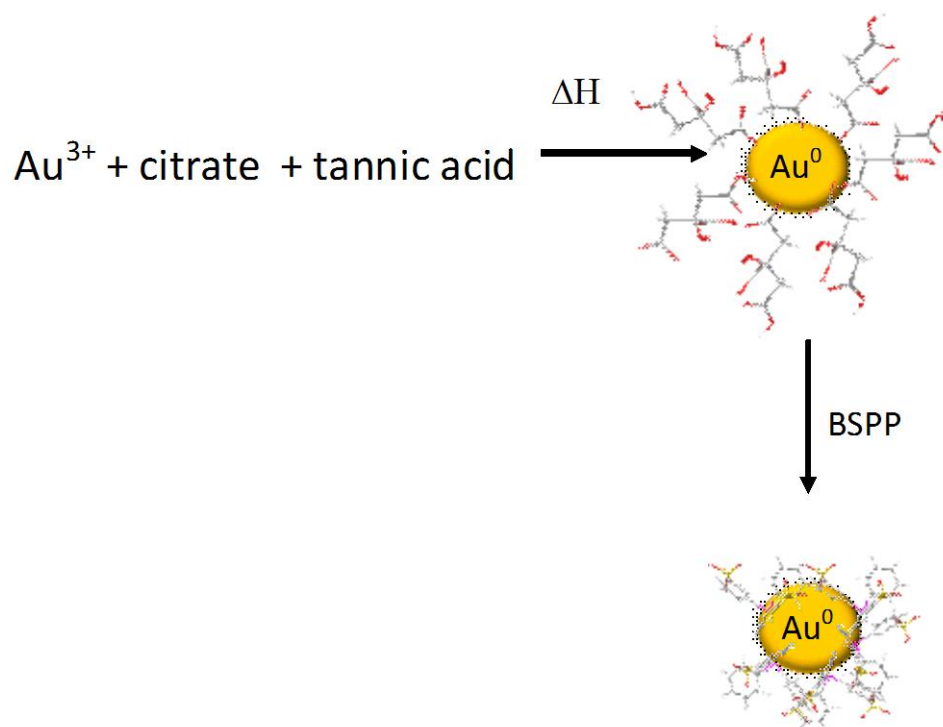


**Figure 2.10** Reaction mechanism for citrate reduction and subsequent ligand exchange of AuNP

Another important note to make is the control over the temperature for this method is crucial. Uneven heating of the reaction or failing to heat the acid solution before injecting into the gold solution can result in nonspherical particles. This will most easily be distinguished in the absorption spectra as a peak begins to form slightly bluer than the normal LSPR band at 520nm. TEM analysis is also a good indicator of a failed reaction. In most cases egg shaped particles are formed. This method cannot produce nanoparticles with good size distribution below 3nm so in order to probe down to the metallic limit (about 1.5nm) another technique was used.

**Method 2** Metal nanoparticles approximately 2nm in diameter were synthesized via a biphasic reaction and then phase exchanged into water with BSPP. Citric acid and tannic acid are

not able to protect the particle surfaces well enough to prevent growth below 3nm, thus this synthesis utilizing a more protective capping-ligand was necessary to synthesize 2nm nanoparticles. This method can be used to produce water soluble AuNPs, palladium NPs, and a variety of alloys containing these two metals. First, X moles of  $\text{HAuCl}_4$  were dissolved in degassed water with Y moles of  $\text{PdCl}_2$ , where  $X+Y= 0.125\text{mmoles}$ . Then, 500mg of BSPP were added to the solution and stirred for 10 minutes. After stirring for 10 minutes, 1mL of freshly made aliquot of 0.1M  $\text{NaBH}_4$  solution is rapidly injected. The nanoparticles are formed instantly but the reaction is allowed to stir for an additional 3 hours to allow for the complete reaction of excess  $\text{NaBH}_4$ . X-ray Fluorescence (XRF) was performed on alloyed nanoparticles to determine the mole fraction of the metals contained within the nanoparticle. Table 2.2 shows these results.

TEM analysis of the AuNPs synthesized via method 2 is shown in Figure 2.11. It illustrates a mean diameter of 1.89 nm with a distribution of 0.35nm, an 18% dispersity. The Gaussian fit of the histogram indicates reasonable control over growth. It is important to note that even though this sample has the smallest distribution it also has one of the broadest size dispersions. The smaller size is achieved by maintaining greater control of the reduction and passivation during the nanoparticle formation. For the AuNPs this is done by reducing the  $\text{Au}^{3+}$  in  $\text{HAuCl}_4$  to  $\text{Au}^+$  during the coordination of the BSPP ligand before reduction. This process is observed for AuNPs as the solution changes colors upon the addition of the BSPP. The pre-reduction results in a nucleation process that requires only one electron shortening the time between the reduction to  $\text{Au}^0$  and passivation by the BSPP.

**Table 2.2** The XRF results for Au/Pd alloyed nanoparticles prepared by method 2. The data shows good correlation between the mole fraction of the reactants and the mole fraction in the products.

Fraction of H <sub>2</sub> AuCl <sub>4</sub> used	Fraction of PdCl <sub>2</sub> used	Mole fraction Au of sample	Mole fraction Pd of sample
1	0	1	0
0.75	0.25	0.66	0.34
0.5	0.5	0.45	0.55
0.25	0.75	0.72	0.28
0	1	0	1

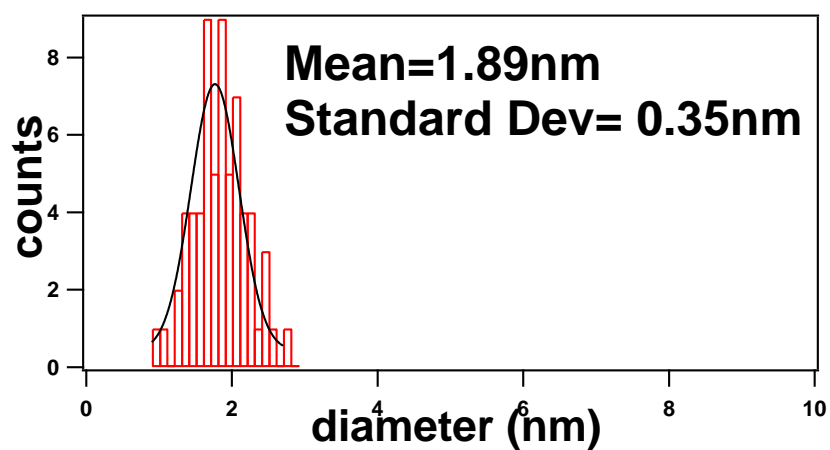
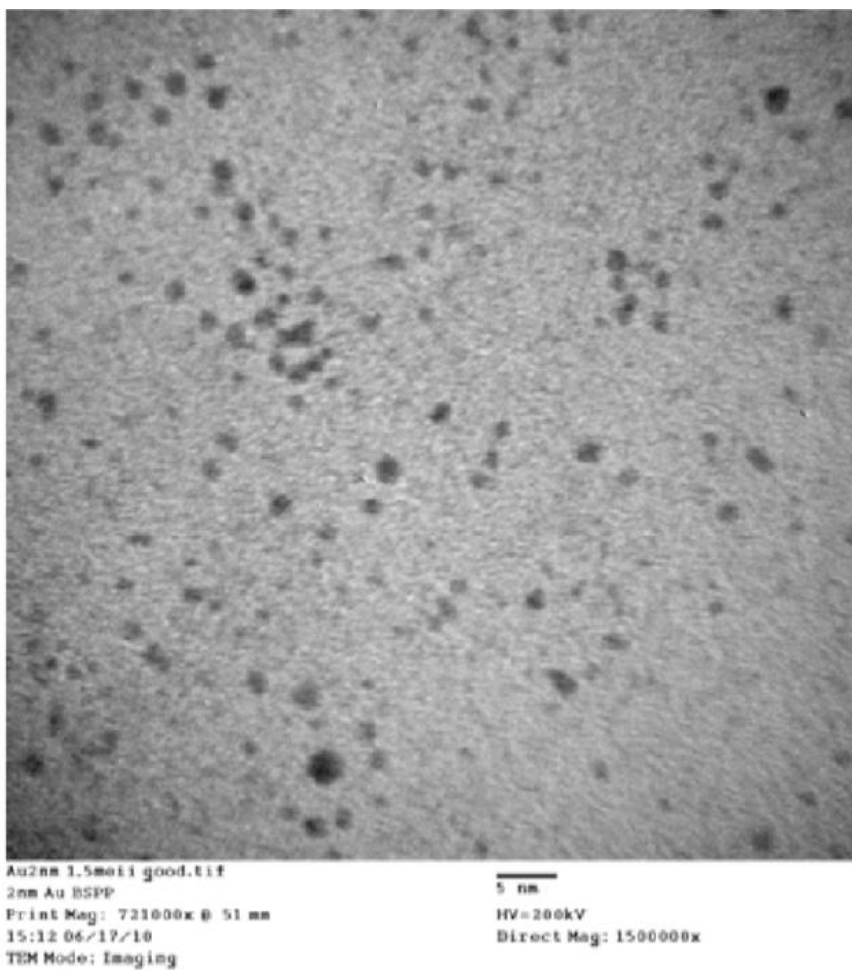


**Figure 2.11** TEM image with size analysis for 1.89nm AuNPs showing a standard deviation of 0.35. Scale bar in image represents 5nm

### **2.2.2 Biphasic Reduction of Metal Particles (Ni, Pd, Pt, and Au)**

Organically soluble metal nanoparticles were synthesized with the following method. First, 0.125 mmoles of the metal salt were dissolved in 5 mL of degassed water. Then 6 mL of degassed toluene were injected into the metal salt solution and 350mg of tetra-octylammonium bromide (TOABr) were added to the mixture. In order to phase exchange into toluene TOABr acts as a phase transfer catalyst on the metal ion. For the sake of simplicity, Figure 2.17 illustrates that the metal forms an intermediate structure of TOAM, though it is important to mention this is not an accurate representation of the mechanism [103]. Phase transfer catalysts act like detergents by changing the ionic environment so that the complex is able travel across the aqueous/organic interface. After addition of TOABr, the solution was stirred until all the color has transferred to the organic layer. The water layer was removed and 300mg of triphenyl phosphine (TPP) is added. After 10 minutes of stirring, a color change occurred indicative of metal ion-TPP association. Freshly prepared 0.1 M NaBH<sub>4</sub> was rapidly injected, 1mL, followed by vigorous stirring for 3 hrs. With the injection of the NaBH<sub>4</sub> solution, the metal is reduced to M<sup>0</sup>, initiating the nucleation process and, shortly thereafter, the passivation of the nuclei by TPP. The synthesized nanoparticles are organically soluble, so in order to water solubilize them 500mg of BSPP was dissolved in 6mL of H<sub>2</sub>O and added to the organic reaction mixture. After 48 hours of stirring, the organic layer was removed and the now water soluble particles were precipitated with ethanol. Figure 2.12 shows the proposed mechanism for this reaction.

## **2.3 Microwave Synthesis**

### **2.3.1 Copper Nanoparticles**

Copper nanoparticles were synthesized in a microwave reactor. 540mg of copper acetylacetonate (Cu acac) was dissolved in 18mL of oleic acid (Olac), 20mL of oleylamine

(OIA), and heated in the microwave reactor to 175°C. N-methylpyrrole was rapidly injected and the reaction was held at temperature for 15 minutes. The resulting copper nanoparticles are approximately 6.6nm in diameter and soluble in organic solvents. Figure 2.13 is a TEM image of the microwave synthesized copper nanoparticles.

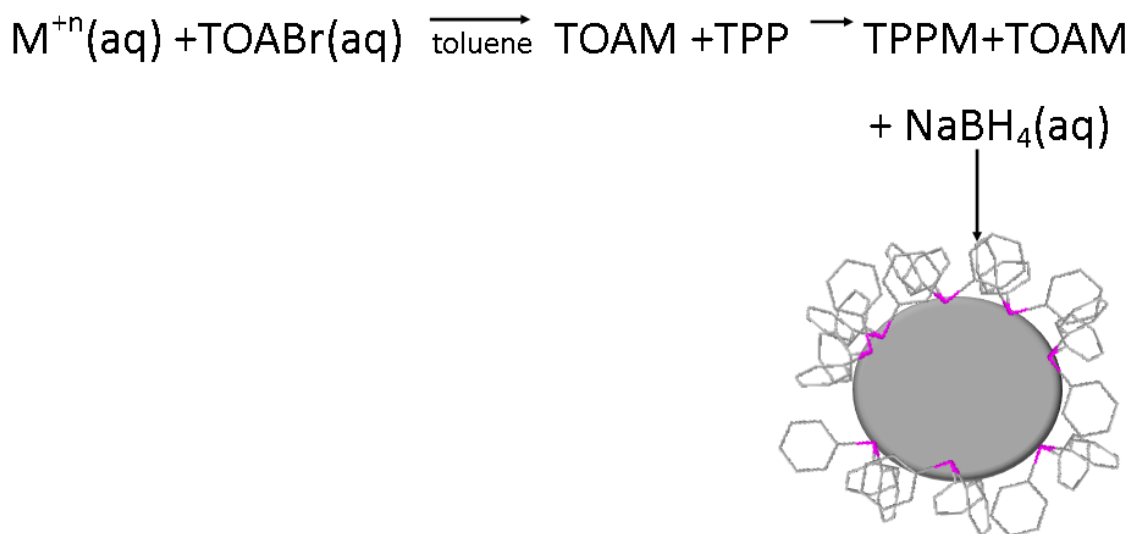
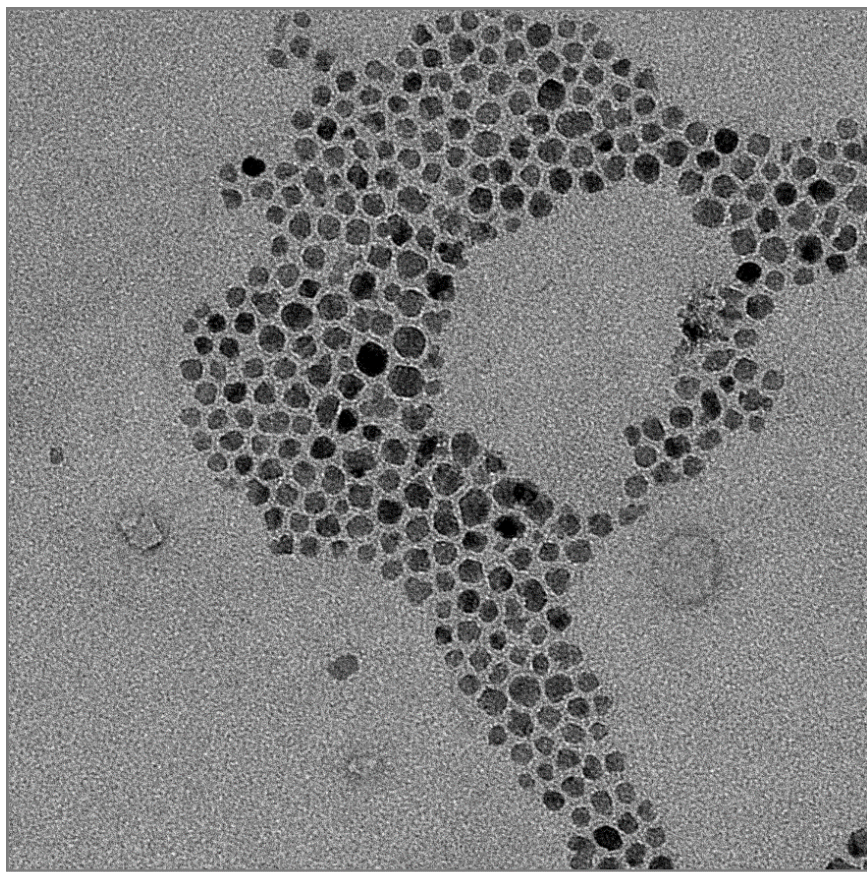


**Figure 2.12** Mechanism for metal nanoparticle formation from the biphasic method.  $M^{+n}$  represents the metal ion of choice ( $Au^{3+}$ ,  $Pd^{2+}$ ,  $Pt^{2+}$ ,  $Ni^{2+}$ , or  $Ag^{+}$ ) that is coordinated with TOA to phase transfer into toluene from water. TPP is then added and some of the  $M$  ions form complexes with it (usually seen as a color change in the reaction solution) and then the ions are reduced with  $NaBH_4$  and form TPP passivated NPs

The copper nanoparticles are primarily spherical, but not as ideally formed as the AuNPs. Figure 2.13 is a histogram of the TEM analysis, which shows an average diameter of 6.6nm with a distribution of 1.01nm, a 15% dispersity. This may be due to a mix of ligands on the surface, possibly a combination of Olac and OIA, resulting in uneven growth at the nanocrystal's facets. The mixture of Olac and OIA is required to produce copper nanoparticles. Without the OIA the

nanoparticles do not form, and without the Olac the reaction does not heat as efficiently under microwave irradiation.



35-01-2012 05:40:06

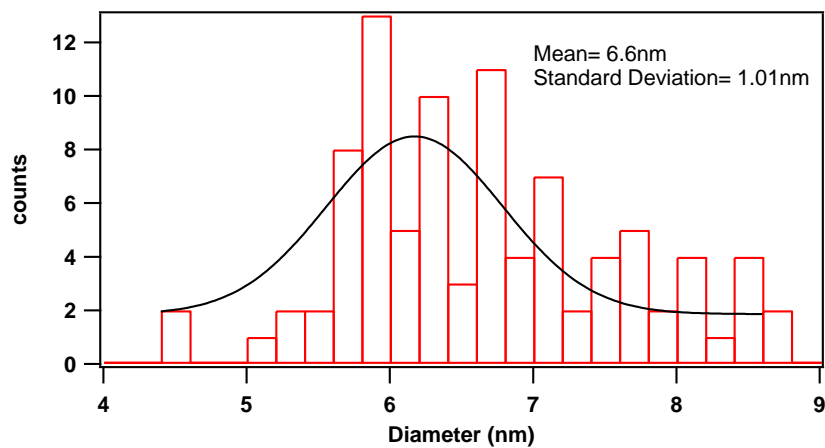


**Figure 2.13** Microwave formed Copper nanoparticles mean diameter of 6.6nm and a size distribution of 1.01nm. Scale bar in the image represents 100nm

### 2.3.2 Fe<sub>3</sub>O<sub>4</sub> Microwave Synthesis

Fe<sub>3</sub>O<sub>4</sub> was synthesized by dissolving 500mg of Iron (II) acetoacetate (Fe acac) in 18mL of OIA and 20mL of Olac. The solution was heated to 180°C and 2mL of n-methylpyrrole was rapidly injected. The temperature was held at 180°C for 30 minutes and cooled to room temperature. The resulting nanoparticles were magnetically separated and washed with methanol. These particles are approximately 7nm in diameter and soluble in toluene. A typical reaction yielded about 150mg of nanoparticles. Figure 2.14 shows the TEM analysis of the Fe<sub>3</sub>O<sub>4</sub> nanoparticles and their formation of ordered structures during deposition onto the copper TEM grids. The mean size was determined to be 7.0nm with a distribution of 0.6nm, an 8% size dispersity. The dramatic improvement in dispersity of the Fe<sub>3</sub>O<sub>4</sub> particles over the copper nanoparticles may be attributed to longer microwave reaction time, permitting Oswald ripening of the smaller populations. Moreover, the passivation of the surface of Fe<sub>3</sub>O<sub>4</sub>, with OIA, is slightly more favorable than that of copper [47].

### 2.4 Gold Shelling of Iron Oxide

Fe<sub>3</sub>O<sub>4</sub> NPs were synthesized via the method from section 2.4.2 and were cleaned by magnetic separation. To prepare for Au shell generation on the Fe<sub>3</sub>O<sub>4</sub> nanoparticle surface, the OIA on the surface was ligand exchanged with hexadecylamine (HDA) at 60 °C for 24 hours. The organically soluble NPs were then cleaned with methanol and magnetically separated out to store dry. Chloro tri-phenyl phosphine gold(I) was synthesized via ethanol reduction of H<sub>2</sub>AuCl<sub>4</sub> in the presence of excess tri-phenyl phosphine (TPP) at room temperature under nitrogen. The excess TPP was washed away with ethanol during vacuum filtration and the remaining white powder was dried under vacuum. The powder was then dissolved in chloroform and

recrystallized with hexane. The fine white crystals were dried under vacuum and weighed out for use in the gold shelling.

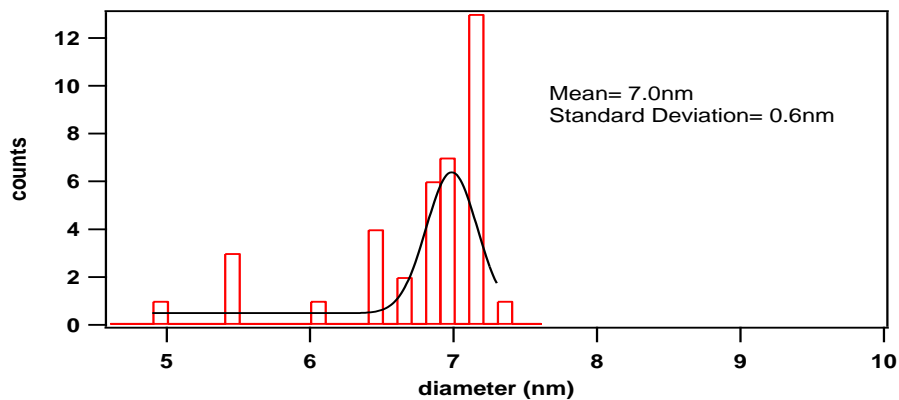
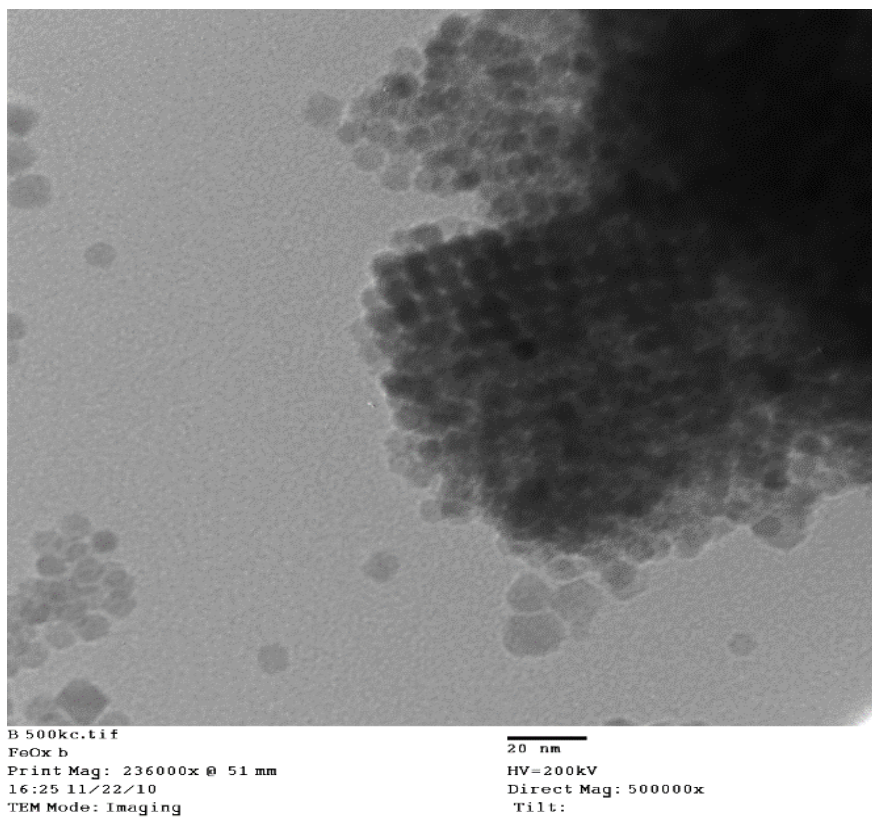


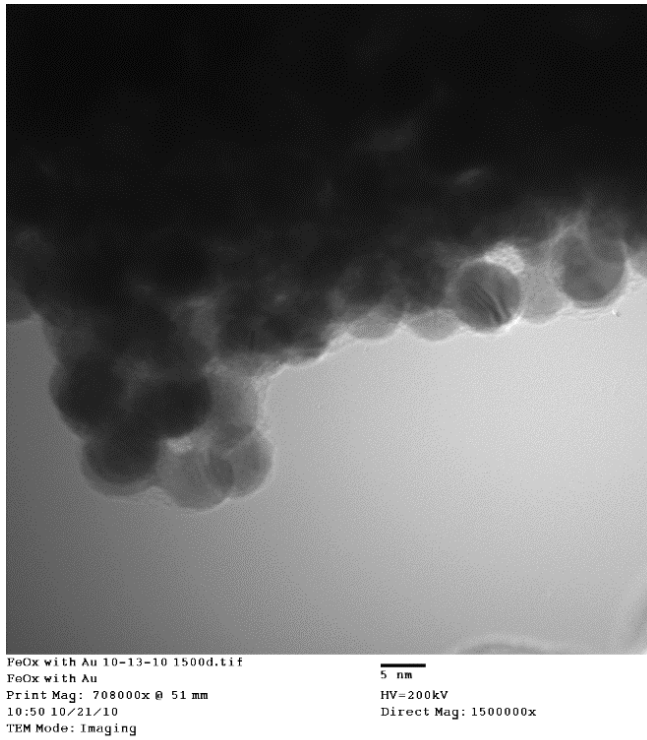
**Figure 2.14** TEM of Fe<sub>3</sub>O<sub>4</sub> nanoparticles with a mean diameter of about 7nm and a distribution of 0.6nm, scale bar 20nm

For the Fe<sub>3</sub>O<sub>4</sub> NPs, 7nm in diameter, 15mg of the organically soluble NPs were dissolved in 5mL of trichloroethene, forming a black solution, and heated to 60 °C to remove any remnant magnetism. Then, 300mg of the gold salt dissolved in the minimum amount of chloroform was injected into the NP solution, turning the solution purple. The reaction was allowed to cool to RT before a 1mL of 1mM NaBH<sub>4</sub> in ethanol was rapidly injected into the reaction. The resulting mixture was stirred for an additional 3 hours to ensure all the NaBH<sub>4</sub> has reacted. The final solution was dark red/purple. The gold shelled Fe<sub>3</sub>O<sub>4</sub> NPs were then washed with methanol and magnetically separated. Figure 2.15 shows TEM of the shelled material as well as the magnetic properties of the nanoparticles before and after shelling. The total emu/g drops after the Au shelling because the Au shell adds mass to the particles without additional magnetic moment, dropping the overall magnetic saturation. The drop in saturation corresponds to a 1nm thick Au shell, confirmed by the TEM.

Confirmation of the Au shelling is indicated in Figure 2.16. The absorption spectra of the organically soluble Au coated Fe<sub>3</sub>O<sub>4</sub> exhibits a prominent feature centered at 535nm. This feature is the developed LSPR band of the Au shell around the Fe<sub>3</sub>O<sub>4</sub> nanoparticle. Further evidence of the Au layer around the Fe<sub>3</sub>O<sub>4</sub> is demonstrated in the pXRD pattern of the shelled nanoparticles. The gold peaks obscure most of the Fe<sub>3</sub>O<sub>4</sub> peaks with only a small portion of the signal stemming from the core. Using the information provided in Figures 2.15 and 2.16 it is easy to conclude that the shelling process is effective. This process exhibits better control over other shelling methods reported in the literature [110, 111]], which can be attributed to the substitution of the Au<sup>+3</sup> salt with a Au<sup>+1</sup> salt as a starting material. Traditional methods utilize the association of the preformed AuNPs with the surface of Fe<sub>3</sub>O<sub>4</sub> NPs and then introduce “filler” Au<sup>+3</sup> ions to reduce into the gaps of the AuNP seeds. This method is appropriately termed

“seeded growth” [110]. The seeded growth techniques have been shown to form highly uniform shells but those shells are much thicker than 1nm since the seeds used are around 2nm in diameter. Another way to produce Au shells is the simple addition of  $\text{Au}^{+3}$  salt to  $\text{Fe}_3\text{O}_4$  NPs and direct reduction onto the surface [111]. Since this is a 3 electron process, this method generally does not produce as uniform shells as using the  $\text{Au}^{+1}$  salt discussed earlier.

(a)



(b)

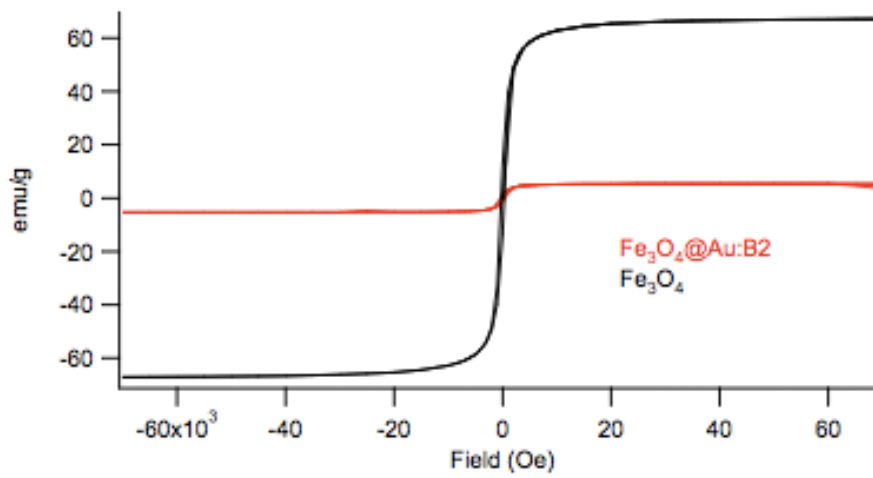
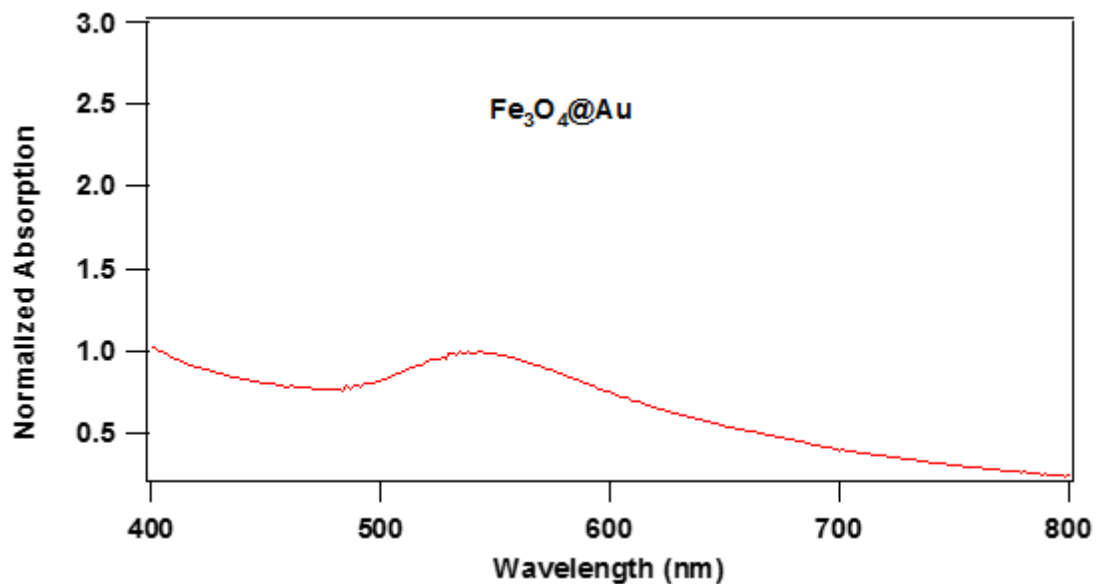


**Figure 2.15** (a) TEM of Au shelled  $\text{Fe}_3\text{O}_4$  nanoparticles. (b) shows the saturation limit of the  $\text{Fe}_3\text{O}_4$  drops from 64 emu/g to 8 emu/g after gold shelling

(a)



(b)

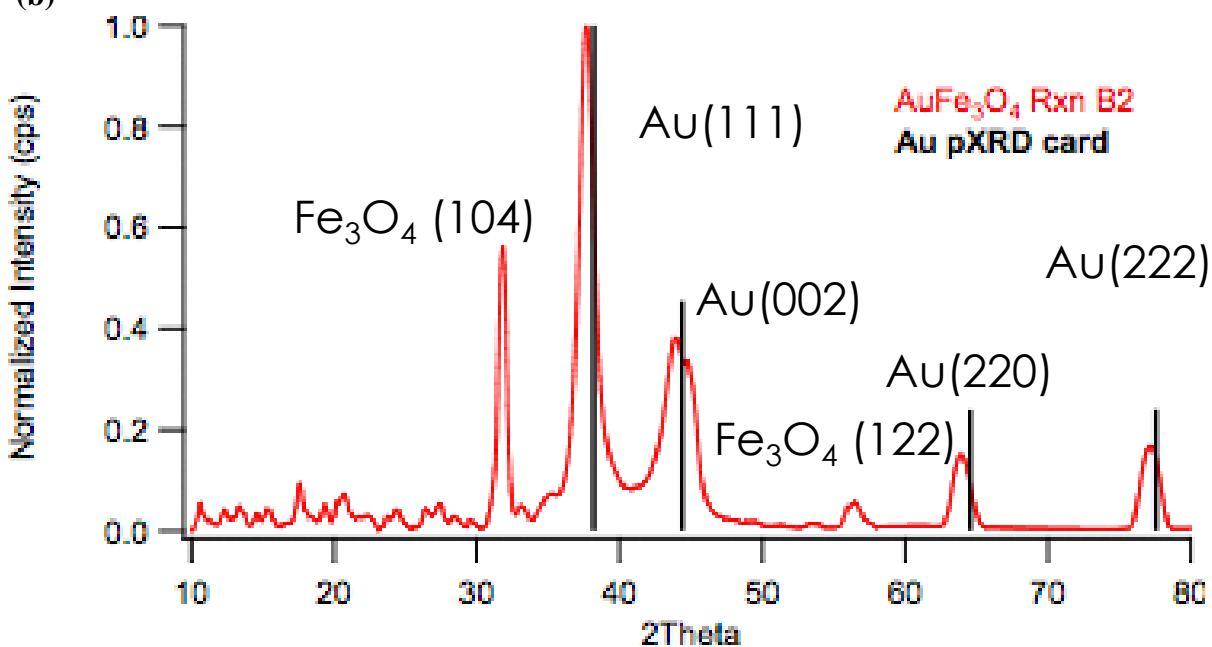


**Figure 2.16** (a) absorption spectra of Au coated Fe<sub>3</sub>O<sub>4</sub> nanoparticles suspended in Toluene. (b) pXRD pattern for the Au coated Fe<sub>3</sub>O<sub>4</sub>.

## **CHAPTER THREE**

# **NANOMETAL SURFACE ENERGY TRANSFER PREDICTS THE SIZE-ENHANCED ENERGY COUPLING BETWEEN A METAL NANOPARTICLE AND AN EMITTING DIPOLE**

### **3.1 Introduction**

Engineering fluorescent properties has led to significant advances in the fields of high throughput DNA detection, bio-imaging, drug delivery, and structural biology by utilizing the optical signature of the fluorescent molecule as a marker for imaging applications, or in energy transfer studies [48-50, 2, 104, 5-7]. Energy transfer can be radiative or non-radiative and is the basis of optical molecular rulers, where a donor and acceptor exhibit distance dependent coupling [48-50, 2]. While Förster resonance energy transfer (FRET) is perhaps the best known of these optical probe methods [104,5, 52], the use of a gold nanoparticle (AuNP) as a proximal quencher of a fluorophore in nanometal surface energy transfer (NSET) methods has garnered attention due to its ability to more than double the range for energy transfer [48, 49, 32, 53, 54]. Although the enhanced proximal quenching of an excited state oscillator in the near field of a AuNP is well accepted, the mechanistic picture to explain the observation and the formulation of a mathematical model with predictive capability is still lacking. This manuscript develops an NSET model that predicts the metal nanoparticle size dependent quenching of an excited state dye positioned at a fixed distance by considering the mathematical implications of enhanced coupling between a fluorophore dipole and the localized surface plasmon (LSPR) that arise from the Drude like electrons in a metal nanoparticle.

The theoretical size dependent NSET model represents an extension of the seminal work of Kuhn [38] and Chance, Prock, and Silbey [39] (CPS-Kuhn) that theoretically treated an oscillator interacting with a bulk metal or thin film. The presented theory provides a mathematically rigorous analysis of the NSET behavior at AuNP surfaces by correctly incorporating the observed changes in absorptivity and dielectric constants as the AuNP changes size to correctly account for the magnitude of the induced image dipole and its effect on an oscillator at the surface of a AuNP. By incorporating the changes in the complex dielectric function and the absorptivity of the AuNP, the size dependent efficiencies and resultant  $d_0$  values can be theoretically predicted for fluorescent molecules in resonance with the LSPR of the AuNP. The developed model is tested for AuNPs between 0.945 and 8.25 nm in radii (1.90 nm–16.5 nm diameter) using fluorescein (FAM,  $\lambda_{em}=518$  nm) as the donor fluorescent molecule at separation distances from 6.8 nm to 27 nm. The model is further verified at selected sizes and lengths for cyanine-3B (Cy3B,  $\lambda_{em} = 570$  nm). The separation is controlled by implementation of duplex DNA spacers with specific chemical modifications for fluorescent molecule appendage and AuNP coupling at discrete locations on the DNA.

Early studies on proximal quenching of a dye at the surface of a 2nm AuNP was observed to exhibit an  $R^{-4}$  distance dependence for quenching of emitting fluorescent molecules overlapping the AuNP LSPR. The studies led to the reported observation that the FRET distances typically employed for molecular rulers could be surpassed by use of a metal nanoparticle. The surprising result was understood in terms of a quenching of the fluorescent molecule occurring within the near field of the AuNP by formation of an image dipole at the nanoparticle surface [32, 19, 33]. Although not mathematically rigorous, the NSET results could be predicted by applying the limiting conditions proposed by CPS-Kuhn for an oscillator

interacting with a thin mirror [33, 42]. As the AuNP increased in size researchers still observed an  $R^{-4}$  dependence but needed to apply an empirical correction to the model to accommodate the experimental results [53, 9, 55, 56, 57]. Thus although the empirical approach could approximate the observed proximal quenching behavior at a 2nm AuNP, the model as originally derived failed to accurately predict the changes in the observed radiative and non-radiative terms for fluorescent molecules as the AuNP increased in size [11,7,58,39]. A number of alternative theoretical models have been developed to treat an oscillator in the metal nanoparticle near field in an attempt to account for the experimentally observed size dependent quenching behavior [55, 39, 6, 8, 60, 38]. The prevailing descriptive models can be classified within a FRET like approximation, a Gerstein-Nitzan (G-N) model [11, 6, 60, 59, 61] or a CPS-Kuhn model [7, 58, 39, 8, 38]. Of these models, only the G-N and CPS-Kuhn models correctly treat the metal-excited state oscillator interactions mathematically rigorously, since the FRET limit is restricted to zero-dimensional dipoles approximated by molecular dyes. The G-N model [6] was developed for large spherical metal particles and predicts an  $R^{-6}$  distance dependence for interaction by considering the AuNP as a single dipole of defined volume with predominately the AuNP enhancing field influencing the dye radiative and non-radiative rates. The G-N model requires a significant scattering contribution from the AuNP for the assumptions to be valid, and therefore would be effective at AuNP radii of  $> 20$  nm. Recent experiments have shown that the G-N model approximates the size dependent quenching behavior for spherical gold  $< 20$  nm in radius [105] but the G-N was unable to predict separation distance dependent quenching behavior [11]. The failure of the G-N model is believed to reflect the inability to accurately predict the observed rates for the dye when the AuNP has insignificant scattering contributions. In comparison, the CPS-Kuhn model [39] was developed to describe thin films below the electron mean free path

and assumes the metal is primarily an absorber of the excited state oscillator energy in the near field through the formation of an image dipole. In the CPS-Kuhn model, the surface is treated as a strongly correlated collection of oscillators resulting in an  $R^{-4}$  distance dependence. The CPS-Kuhn model formed the basis of the original NSET empirical model developed for 2 nm AuNP by assuming a thin film approximation and is shown to correctly predict the size and separation distance data measured experimentally for two dyes in this manuscript when the size dependent absorption and dielectric terms for the AuNP are correctly incorporated into the theory. Unfortunately, over multiple length scales and nanoparticle sizes the models require empirical corrections due to their failure to correctly predict the shape of the quenching efficiency, the frequency dependence for the dye, or the metal size dependence.

The NSET model derived herein provides a firm basis for correctly interpreting the results of researchers utilizing fluorescence quenching methods at a metal nanoparticle surface for applications in sensing and distance measurements. It correctly treats the image dipole within the metal as the collective oscillations of strongly coupled electrons behaving like a confined layer of charge; resulting in the reported  $R^{-4}$  distance dependence observed experimentally. For the sizes modeled here (radius < 20 nm), NSET incorporates the energy transfer pathway into the non-radiative decay rates of the proximal fluorophore so that quenching tracks with particle absorption; as observed experimentally. The model can be easily implemented by spectroscopists and is believed to be extendable to other metals. More importantly, the model does not require extensive calculations typically employed by alternate models based upon a quasi-static [55, 6, 8, 60, 59] or quantum mechanical [61, 62] approach. The strong correlation between theory and experiment provides a firm basis for use of NSET as a molecular ruler technology in biophysical and molecular sciences.

## 3.2 Experimental Section

### 3.2.1 Materials

Spherical gold nanoparticles between 0.945 and 8.25 nm radius (1.9 nm to 16.5 nm diameter) were synthesized by standard literature protocols discussed in chapter two. The fluorescent molecule to AuNP separation distance is controlled by utilizing duplex DNA as a spacer, assuming rigid rod behavior. The DNA lengths utilized in the study are 15bp, 30bp, 45bp, 60bp, and 75bp which when assembled onto the AuNP results in a AuNP surface to center of fluorescent molecule distance of (15bp) 6.8 nm, (30bp) 11.7 nm, (45bp) 17.0 nm, (60bp) 22.0 nm, and (75bp) 27.2nm calculated by the Clegg model [67]. The sequences are given in Table 3.1. Formation of a AuNP-DNA-Fluorescent molecule conjugate is accomplished as described previously utilizing stoichiometric place-exchange of a BSPP passivating layer on the AuNP by the synthetic duplex DNA, which contains a 5'-C6 thiol for attachment to the Au surface. The fluorescent molecule (FAM, Cy3B) is appended to the DNA via a 5'-C6 linker and are available from Midland. Full details and analytical data are available in chapter 2 including TEM, size dispersity, and UV-Vis.

### 3.2.2 Energy Transfer Measurements

The size-dependent AuNP effects on the excited state photoluminescence of FAM was monitored by measuring the integrated fluorescence intensity of the assembled complex ( $I$ ) relative to a sample containing the FAM labeled DNA and a non-appended AuNP ( $I_0$ ) under identical reaction conditions and plotted in terms of efficiency of energy transfer ( $E_{EnT}$ ), where  $E_{EnT} = 1 - \frac{I}{I_0}$ . Steady state photoluminescence (PL) measurements were acquired on samples dissolved in 100 mM PBS buffer (50mM NaCl, pH = 7.8) on a Varian Cary Eclipse Fluorescence spectrophotometer using Z-matched 50  $\mu$ L quartz cuvettes. Fluorescein (FAM) is

pumped at 490 nm and the PL spectra monitored between 500 nm and 800 nm. The PL data is corrected for scattering and absorption by the AuNP by comparison to a control consisting of the fluorescent molecule labeled DNA in the presence of uncoupled AuNP at an identical concentration.

**Table 3.1** DNA sequences used as spacers for the proximal quenching of the dyes, FAM and Cy3B.

<b>15mer</b> - 68 Å	Dye-C <sub>6</sub> -CGTGTGAATTCGTGC
T <sub>m</sub> =48.1 °C, ΔG <sub>1</sub> =-28.76kcal/mol, ΔG <sub>2</sub> =-6.91kcal/mol	HS-C <sub>6</sub> -GCACGAATTCACACG
<b>30mer</b> - 117 Å	Dye-C <sub>6</sub> -CGCCTACTACCGAATTCGATAGTCATCAGC
T <sub>m</sub> = 61.3 °C, ΔG <sub>1</sub> = -56.65kcal/mol, ΔG <sub>2</sub> =-5.19kcal/mol	HS-C <sub>6</sub> -GCTGATGACTATCGAATTCGGTAGTAGGCG
<b>45mer</b> - 170 Å	Dye-C <sub>6</sub> -CGTTCCGTGTGCATACTGAATTCGGTGTACTCTTGCCAACCTCG
T <sub>m</sub> = 68.3 °C, ΔG <sub>1</sub> =-88.22kcal/mol, ΔG <sub>2</sub> =-14.84kcal/mol	HS-C <sub>6</sub> -CGAGGTTGGCAAGAGTAACACGGAATTCAGTATGCACACGGAACG
<b>60mer</b> - 220 Å	Dye-C <sub>6</sub> - CGTTCCGTGCACATACTATCCACTCTTAGCGAATTCATCCACATAATCTCT AGTATCTGC
T <sub>m</sub> = 67.0 °C, ΔG <sub>1</sub> =-107.26kcal/mol, ΔG <sub>2</sub> =-9.41kcal/mol	HS-C <sub>6</sub> - GCAGATACTAGAGATTATGTGGATGAATTCGCTAAGAGTGGATAGTATGT GCACGGAACG
<b>75mer</b> - 272 Å	Dye-C <sub>6</sub> - CGTTCCGTGTGCATACTGAATTCGGTGTACTCTTGCCAACCTCGCGTTC CGTGTGCATACTGAATTCGGTGTTA
T <sub>m</sub> = 71.7 °C, ΔG <sub>1</sub> =-148.27kcal/mol, ΔG <sub>2</sub> =-56.91kcal/mol	HS-C <sub>6</sub> - TAACACGGAATTCAGTATGCACACGGAACGCGAGGTTGGCAAGAGTAA CACGGAATTCAGTATGCACACGGAACG

The size dependent AuNP-Cy3B interaction was analyzed by monitoring the spectrally resolved excited state lifetime, where  $E_{EnT} = 1 - \frac{\tau}{\tau_0}$ . The lifetime measurements were acquired

by exciting Cy3B at 560 nm (<1 mW) using a Nd:VO<sub>4</sub>-pumped (Spectra-Physics Vanguard, 2W, 532 nm, 76 MHz, 10 ps), cavity dumped R6G fluorescent molecule laser (Coherent 702-1) as a source and collected onto a Hamamatsu C5680 streak camera coupled to a Chromex 500 imaging monochromator. The intensity decay profiles are binned over a 20 nm spectral window.

### 3.3 Results and Discussion

Several attempts have been made to describe this interaction in the near field by considering formation of an image dipole in analogy to a mirror effect (CPS-Kuhn) [39] or by coupling to the metal radiating field (G-N) [6]. The rate of emission ( $k_{\text{obs}}$ ) for an excited state oscillator (fluorescent molecule) is defined by its radiative ( $k_r$ ) and non-radiative ( $k_{\text{nr}}$ ) terms. When an excited state oscillating dipole is positioned within the near field of a bulk metal, metal foil or nanoparticle, the oscillator will interact with the near field of the metal through coupling which will influence its non-radiative and radiative rates of the oscillating dipole. The non-radiative rate of the oscillator is modified by transferring energy to the absorbing metal, with subsequent Joule heating within the metal; and the radiative rate is modified due to the Purcell effect by reflection of the field back onto the emitting molecule. The magnitude of the effect on non-radiative and radiative rates is dependent on the presence of a strong local field to increase the photonic mode density appreciably at the emitting dipole, and therefore the nature of the fluorophore-metal interaction will be different due to changes in the magnitude of the scattering, absorption, and image dipole strength. For a gold nanoparticle below a 20 nm radius, scattering can be largely ignored and thus the particle behaves mostly as a simple absorber [64]. Therefore, for fluorophores proximal to a AuNP with a radius less than 20nm only the non-radiative rates will be significantly modified while the radiative rate modification is minimal.

The nature of the interaction of the emitting oscillator with the metal will be strongly dependent on the separation distance of the oscillator from the metal, the frequency of the oscillator, and the extent of the coupling. As noted by Kreibig [9], the LSPR modes represent the collective oscillation of many strongly coupled electrons and therefore the coupling of the oscillator is best described as an interaction with an array of coupled dipoles, as initially described by the CPS-Kuhn model. In contrast, the G-N model assumes a dipole approximation arising from treating the  $L=1$  mode of LSPR excitation as ‘the dipole mode’ which represents an over-simplification. The dipole assumptions lead to  $F_{DA}=1/r^3 * 1/r=1/r^4$  distance dependence predicted by CPS-Kuhn instead of the  $F_{DA}=1/r^6$  dependence derived by G-N. Although the two approaches are powerful predictors of the observed trends, it has been reported that as the metal nanoparticle is reduced in size the change in extinction cross-section and a loss of the scattering component in the complex dielectric leads to failure of the models to predict experimental results for both the CPS-Kuhn and G-N theories [11, 33]. To derive an effective expression that predicts the observed experimental proximal quenching behavior for AuNPs below 10 nm in radius, the change in the physical properties of the gold nanoparticle must be considered.

In a nanoparticle, neither an infinite surface nor a bulk volume is a correct model and thus the CPS-Kuhn model, although validated in thin films [39, 38] traditionally over-predicts the interaction strength for nanoparticles [32, 33]. It is reasonable to assume that the failure of the model in nanoparticles reflects the size dependent changes in the AuNP dielectric properties and changes to the optical cross section. The size dependent electronic properties of the AuNP can be incorporated by redefining the quasi-static model of Chance, Prock, and Silbey (CPS-Kuhn) within a nanoparticle limit [33, 38, 39] The CPS-Kuhn assumption of perfect mirror behavior for describing the oscillator-metal interaction is not appropriate in small metal

nanoparticle. For metal nanoparticles below 50 nm radius, the weak absorption limit is appropriate which translates to the interaction of the metal with the oscillator being described primarily by the effect on the non-radiative rate of the oscillator when describing the oscillator NP interaction. The loss of perfect mirror behavior is readily incorporated into the theory by introducing size dependent electronic properties that are defined with respect to the metal nanoparticle radius. To accomplish this it is useful to begin with the of CPS-Kuhn theory expressed in terms of the distance at which the probability of non- radiative quenching of the fluorescent molecule excited state results in a lowering of the PL intensity by 50%.

$$d_0 = \frac{\alpha\lambda}{n_m} (A\Phi)^{1/4} \left( \frac{n_r}{2n_m} \left( 1 + \frac{\epsilon_1^2}{|\epsilon_2|^2} \right) \right)^{1/4} \quad (3.1)$$

The  $d_0$  value incorporates donor and acceptor terms that while not directly analogous to the FRET  $\langle J \rangle$  overlap expression are in effect related if one assumes the donor oscillator couples to states below the Fermi level (Drude model) in the AuNP. The donor specific terms are:  $\lambda$ , the emission wavelength maximum for the donor, and  $\Phi$ , the quantum yield of the donor. The acceptor specific terms include  $A$ , the absorptivity of a thin film mirror;  $n_r$ , the refractive index of the metal; and  $\epsilon_2$ , the complex dielectric function of the metal which can be decomposed into the real and imaginary components ( $\epsilon_2 = \epsilon_2' + i \epsilon_2''$ ). In CPS-Kuhn,  $\epsilon_1$  is the solvent dielectric and  $n_m$  is the index of refraction. The orientation of the donor to the metal plasmon vector is  $\alpha$ , and is assumed to be influenced only by the averaged vector resulting in  $\alpha = ((9/2)^{1/4})/4\pi$ . As stated earlier, the CPS-Kuhn expression is only appropriate for a thin film with mirror-like behavior where the image dipole depth is defined by the penetration depth of the oscillator dipole, which is dependent on the metal complex dielectric function ( $\epsilon_2$ ) and absorptivity ( $A$ ) at the oscillator frequency[39].

To account for the interaction of an oscillator within the limited volume of a nanoparticle, the size dependent electronic terms including the change in the dielectric constant and the cross-section for absorption of incident radiation must be incorporated. This can be accomplished by redefining the CPS-Kuhn expression to accurately account for the expected change in the  $\epsilon_2$  and A values as the NP decreases in size. The size dependent response of  $\epsilon_2$  has not been previously considered in the development of energy transfer models to metal NPs. It can be correctly incorporated by utilizing the full complex dielectric function, including bulk ( $\epsilon_\infty$ ), Drude ( $\epsilon_{Drude}$ ), and interband ( $\epsilon_{IB}$ ) contributions; allowing the complex dielectric to be expressed as a size dependent function.

$$\epsilon_2 = \epsilon_\infty + \epsilon_{Drude} + \epsilon_{IB} \quad (3.2)$$

$$\epsilon_{Drude} = 1 - \frac{\omega_p^2}{\omega^2 + \Gamma_r^2} + i \frac{\Gamma_r \omega_p^2}{\omega(\omega^2 + \Gamma_r^2)}$$

$$\epsilon_{IB} = \sum_{i=1,2} \frac{A_i}{\omega_i} \left[ \frac{e^{i\phi_i}}{\omega_i^{-1} - \omega^{-1} - \Gamma_i^{-1}} + \frac{e^{-i\phi_i}}{\omega_i^{-1} + \omega^{-1} + \Gamma_i^{-1}} \right]$$

where  $\omega$  is the dipole frequency,  $\omega_p$  is the Drude plasmon frequency, and  $\Gamma_r$  is the size-dependent damping constant ( $\Gamma_r = \Gamma_\infty + \frac{l_\infty}{r}$ ), wherein  $\Gamma_\infty$  is the bulk damping constant,  $l_\infty$  is the mean free path in Au ( $l_\infty = 420\text{\AA}$ ), and  $r$  is the AuNP radius [87,9]. In eq 3.2,  $A_i$ ,  $\omega_i$ ,  $\phi_i$ , and  $\Gamma_i$  are fit parameters in frequency and are listed in Table 3.2 [63].  $A_i$  describes the magnitude of the transition,  $\omega_i$  is the critical frequency of the discrete transition,  $\phi_i$  is the efficiency of the transition and  $\Gamma_i$  is the dampening term the positive charge of the nuclei has on the core electron. The latter term is similar to the dampening term in the Drude expression except that this one is dependent on the material and not the size. The magnitude of  $\Gamma_i$  is also much a larger than that of

$\Gamma_r$ . These terms are fit to experimental observations in the literature, hence the name “fit parameters.”

**Table 3.2** Optical constants used in the derived NSET equation

$\epsilon_\infty$	$\Gamma_\infty$	$\omega_p$	$\omega_{i=1,2}$	$\Gamma_{i=1,2}$	$A_{i=1,2}$	$\phi_{i=1,2}$
1.53	$1.075 \times 10^{14}$	$1.38 \times 10^{16}$	$4.03 \times 10^{15}$ , $5.22 \times 10^{15}$	$4.35 \times 10^{-4}$ , $1.06 \times 10^{-3}$	0.94, 1.36	$-\pi/4$ , $-\pi/4$

Correcting the absorptivity term for size dependence must also be incorporated and has not been considered previously in the literature. The absorptivity of a bulk mirror ( $A_{\text{mirror}}$ ) is defined in terms of a metal thickness for a semi-infinite plane

$$A_{\text{mirror}} = \frac{4\pi k_2 d}{\lambda} \quad (3.3)$$

where  $k_2$  is the extinction component of the complex index of refraction, and  $d$  is the thickness of the metal film. Since a AuNP is not a semi-infinite plane or a perfect mirror, the  $A$ -term re-expressed in terms of the absorptivity within a single nanoparticle in analogy to molecular absorption can be formulated as

$$A_{np} = 10^3 \ln(10) \left[ \frac{\epsilon_\lambda \left( 2 r_{cm} \left( \frac{2 r_{cm}}{\delta_{skin}} \right) \right)}{N_A V_{cm^3}} \right] \quad (3.4)$$

where  $\epsilon_\lambda$  is the extinction coefficient of the NP at the maximum emission wavelength of the donor (size dependent  $\epsilon_\lambda$  values are reported for spherical AuNPs [64, 34].),  $r_{cm}$  is the radius of the NP in cm,  $N_A$  is Avogadro’s number, and  $V_{cm^3}$  is the volume of the particle in  $cm^3$ . By describing absorptivity in terms of the extinction coefficient both the scattering and absorption terms in the complex dielectric can be correctly treated.

Inserting eqns. 3.2 and 3.4 into eqn. 3.1 yields a size dependent NSET expression that predicts the size dependent interaction of an excited state oscillator at a fixed distance from a AuNP surface, given in eqn. 3.5. Fitting eqn. 3.5 with the corrected values for the dielectric (eqn 3.2), absorptivity (eqn 3.4), and literature values for the size dependent extinction terms (Table 3.4) allows a theoretical plot to be generated for the expected AuNP size dependent  $d_0$  values for an emitter in resonance with the LSPR at 518 nm (FAM) and near resonance with the LSPR at 570 nm (Cy3B), as shown in Figure 3.1.

$$d_0 = \frac{\alpha\lambda}{n_m} \left( 10^3 \ln(10) \left[ \frac{\epsilon_\lambda \left( 2 r_{cm} \left( \frac{2 r_{cm}}{\delta_{skin}} \right) \right)}{N_A V_{cm^3}} \right] \phi \right)^{1/4} \left( \frac{n_r}{2n_m} \left( 1 + \frac{\epsilon_1^2}{|\epsilon_\infty + \epsilon_{Drude} + \epsilon_{IB}|^2} \right) \right)^{1/4} \quad (3.5)$$

The theoretical efficiency curves plotted as a function of oscillator to metal surface separation distance is plotted for AuNP radii between 0.95 nm and 8.25 nm is shown for FAM in Fig. 3.1b and Cy3B in Fig. 3.1d. The calculated  $d_0$  distances are listed in Table 3.4 for FAM and Cy3B. In Figure 3.1, the theoretical  $d_0$  plots and efficiency curves predict a size dependent shift to longer distance as the AuNP increases in size. Such a shift has been observed in quenching studies previously [66, 53]. Intriguingly, the  $d_0$  plot exhibits an oscillatory behavior, which reflects the difference in the response of the real and imaginary components of the dielectric function with size. Within the limit of AuNPs below 50 nm radii, the interaction will result in a loss of PL intensity and a shortening of the lifetime of the excited state of a fluorescent molecule that overlaps the localized surface plasmon for a metal NP. The distance dependent quenching behavior has been experimentally demonstrated to follow a  $1/R^4$  distance dependence between the fluorescent molecule to AuNP surface [53, 66].

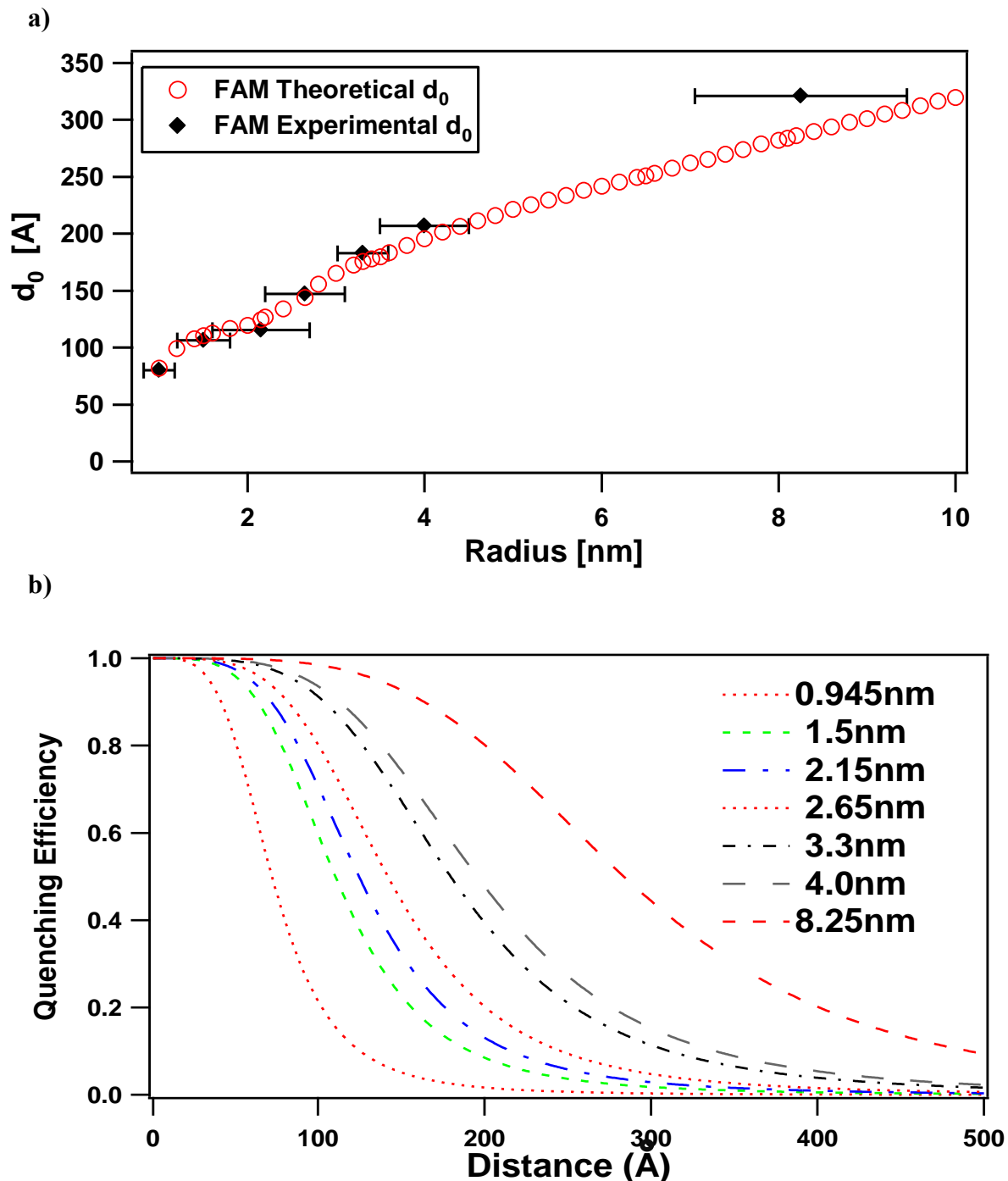
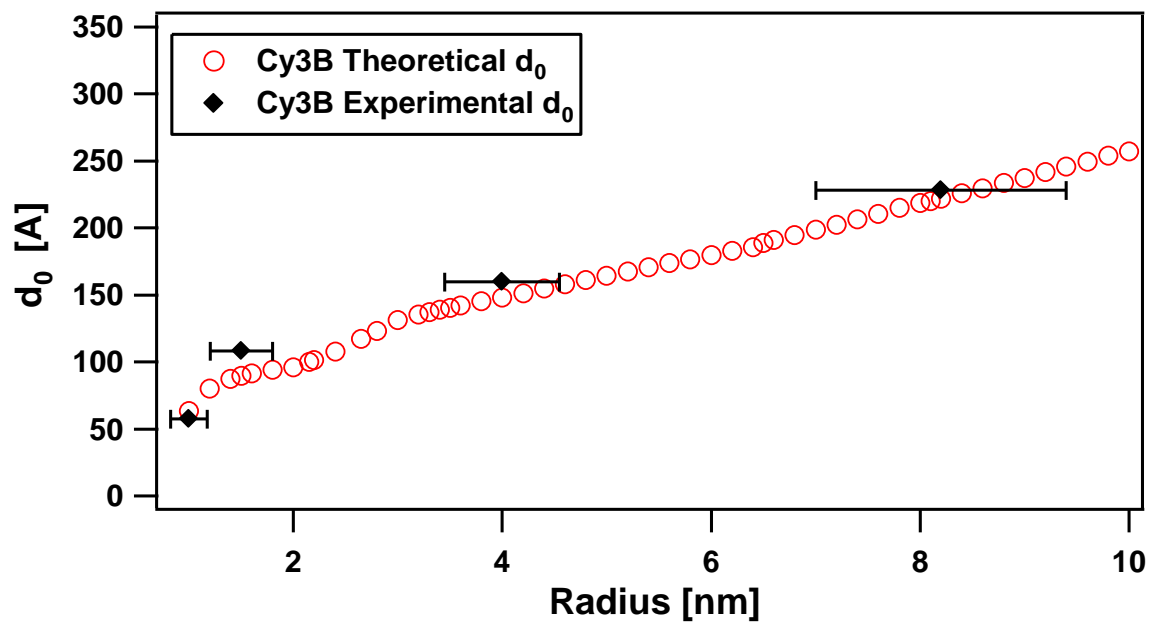


**Figure 3.1** Theoretical size dependent NSET curves illustrating the size dependent behavior for (a)  $d_0$  value for FAM, (b) efficiency curve for FAM, (c)  $d_0$  value for Cy3B, and (d) efficiency curve for Cy3B. The experimental points calculated from separation distance dependent experimental data for the  $d_0$  curves in (a) and (b) are shown as black diamonds

c)



e)

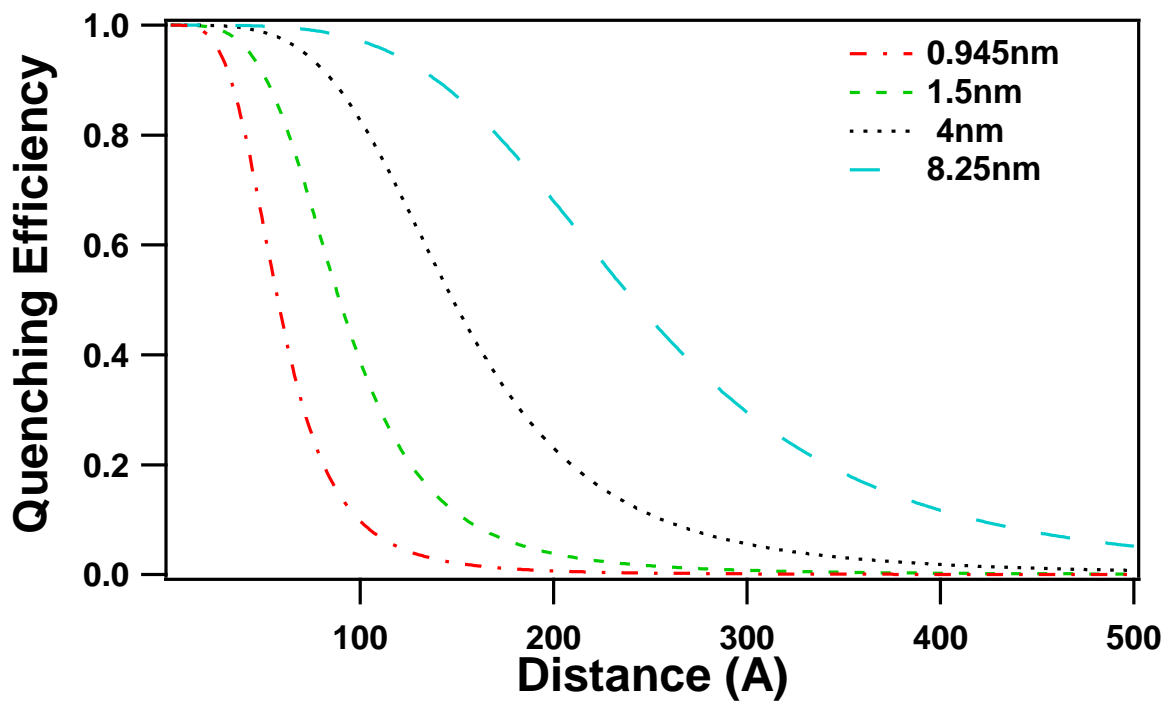


(Figure 3.1 continued)

The observed size dependent shift in energy transfer rates predicted in eqn 3.1- 3.5 can also be plotted as a function of the separation distance of the dye from the metal surface. A convenient way to project this is using an efficiency plot, which exhibits a power law behavior. The efficiency expression can be written as shown in eqn 3.6 if the experimentally reported distance (d) to the fourth power is assumed over all AuNP sizes below 50 nm in radius [53, 66].

$$E_{EnT} = \frac{1}{1 + \left(\frac{d}{d_0}\right)^4} \quad (3.6)$$

In Figures 3.1b and 3.1d, the theoretical size dependent shift in the efficiency curves (dashed lines) for FAM and Cy3B on selected nanoparticle sizes is shown. The choice of the plotted efficiency curves in Figures 3.1b and 3.1d reflect the experimentally measured AuNP sizes used to validate the theory, as discussed below.

### 3.3.1 Experimental Validation of Size Dependent NSET

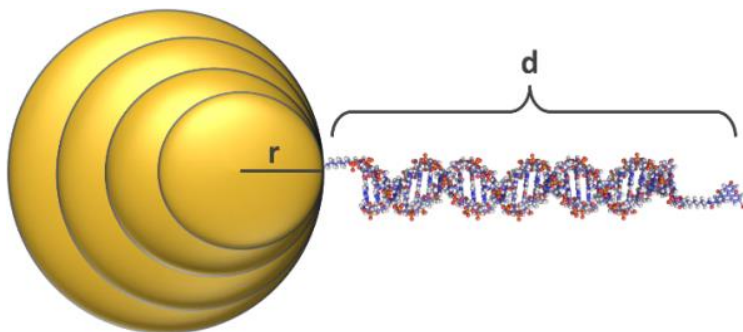
The predictions of the size dependent NSET expression (eqn 3.1-3.6 ) are readily tested by experimentally measuring the emissivity of excited state fluorescent molecules overlapping the AuNP LSPR frequency when positioned at discrete distances from AuNPs between 0.945 and 8.25 nm in radius (1.9 nm to 16.5 nm diameter). A schematic of the AuNP-DNA-fluorescent molecule assembly and the spectral overlap between the fluorescent molecules and AuNP utilized for the study is shown in Figure 3.2. To evaluate the validity of the NSET expression the quenching behavior of FAM and Cy3B were studied. The choice of FAM and Cy3B reflect the desire to be within resonance of the LSPR band on the AuNPs across the full size range studied. These fluorescent molecules remain in resonance as the Au LSPR feature in the extinction spectra exhibits a clear sharpening of the LSPR feature [7]. The model is tested for all AuNP sizes for FAM, while only select data is gathered for Cy3B to validate the developed model.

The distance between the donor and metal in Figure 3.2 is systematically controlled using synthetic DNA to achieve 69 Å (15bp), 118 Å (30bp), 170 Å (45bp), 220 Å (60bp) and 272 Å (75bp). The reported distances are calculated from the AuNP surface to the centroid of the fluorescent molecule according to the Clegg cylinder model [67]. In the calculation the fluorescent molecule is assumed to be a free rotor when coordinated to the 5' end of the DNA through a C6 spacer. Since the Clegg model assumes a rigid rod approximation with B-DNA structure only DNA lengths below 100bps were utilized in the study. DNA lengths below 15bp were not utilized to eliminate DNA melting complications inherent in short DNA lengths. Since the Clegg model requires a perpendicular orientation for the DNA to the AuNP surface, calculations were performed to verify that errors due to tilting are not significant for AuNPs below 8.25nm radius

### **3.3.2 DNA Orientation Effects**

It is well known that self-assembled molecules can tilt at a metal surface or even electrostatically associate with the surface, leading to significant deviation in the measured energy transfer efficiency curve due to perturbation to the measured donor-acceptor distance predicted by the Clegg model Figure 3.3. Recent studies by Li, et al have suggested that the tilt of DNA on a NP surface is influenced by the packing density of the DNA [50]. The potential perturbation in calculated distance will be influenced by electrostatic interactions of the DNA with the NP surface passivation layer [50], DNA packing efficiency at the NP surface [49], and the loading level of DNA on the NP relative to other ligands [2]. Since packing density depends on NP size, the effect of packing on the experimental contact distances and the potential impact on the efficiency curves cannot be summarily rejected without mathematical consideration.

a)



b)

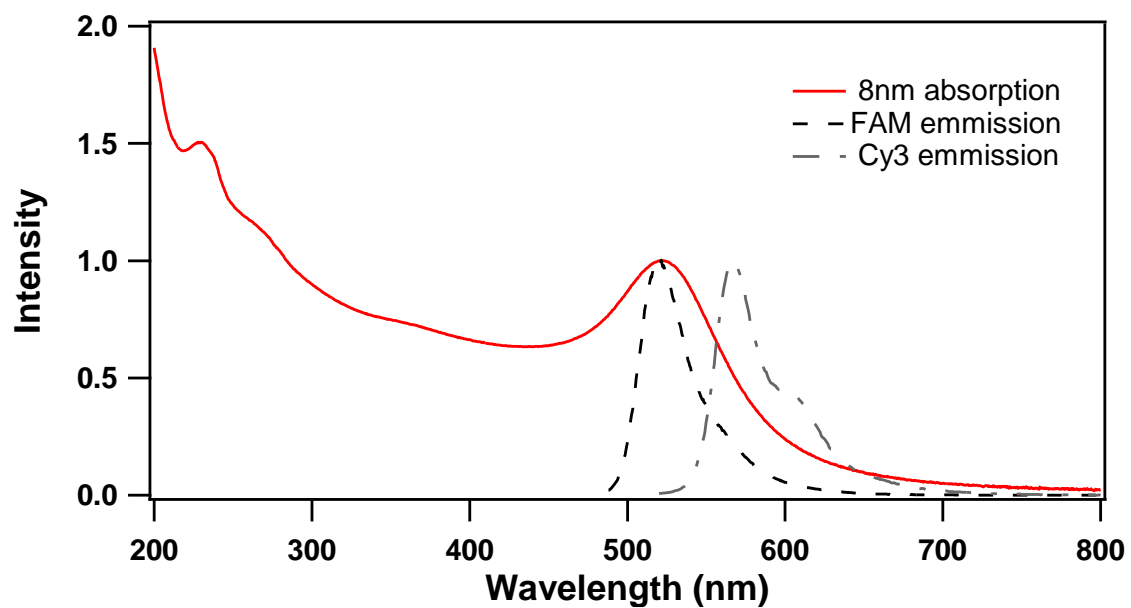


**Figure 3.2** a) Schematic model of AuNP-DNA-fluorescent molecule construct. b) Spectral overlap between 8nm AuNP extinction spectra and the fluorescent molecule emission spectra in water for FAM and Cy3B

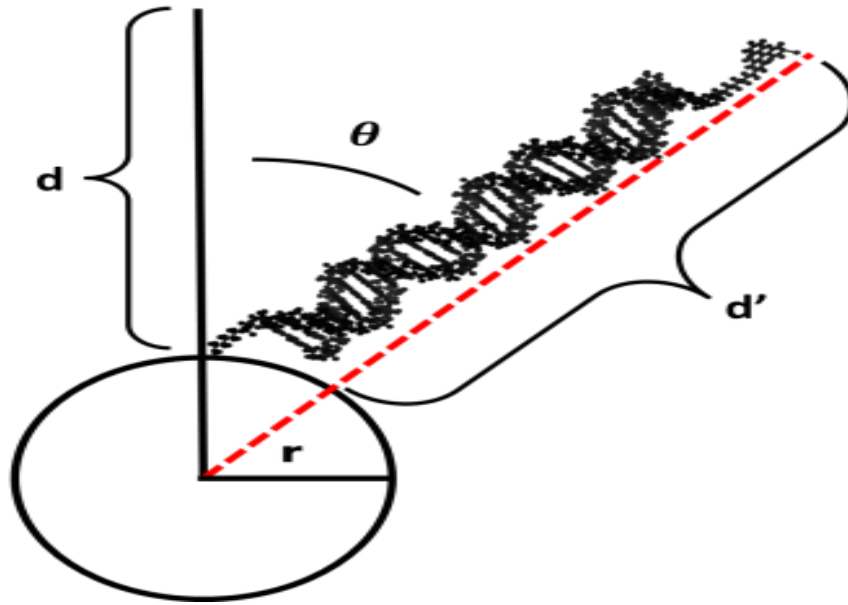


**Figure 3.3** Schematic representation of DNA tilt relative to spherical AuNP, where  $d$  is separation distance,  $d'$  is DNA length from Clegg model,  $r$  is the AuNP radius, and  $\theta$  is the angle of tilt relative to normal

The potential effect of packing induced DNA tilt on experimental distance can be calculated using the predictions of Li, et al by incorporating the size dependent packing density of DNA on AuNPs. The calculation shows no significant perturbation to the calculated distances will arise for AuNPs below 10 nm. It is worth noting that above 10 nm the error can become significant, for example a 20 nm diameter AuNP(20 nm) will exhibit an error in reported distance of 14% for a 15 bp dsDNA appendage. The calculated tilt angle ( $\theta$ ) and packing density for each AuNP size in Figure 3.3 extracted from Li [69] is listed in Table 3.2. Error bars were added the 16.5 nm data points in Figure 3.4 to account for possible orientation effects inducing error,

$$\theta = \arcsin(1.155\sqrt{(1 - 0.866 * 10^{-16} N_A a^2 \Gamma_m)}) \quad (3.7)$$

$$\Gamma_m = \frac{10^{15}}{0.866 N_A L_a^2}$$

where  $N_A$  is avogadros number,  $\alpha$  is the foot print of double stranded DNA ( $\text{cm}^2$ ),  $\Gamma_m$  is the DNA surface coverage ( $\text{mol} \cdot \text{cm}^{-2}$ ), and  $L_\alpha$  is the distance between DNA strands which is calculated using the maximum packing density given by Mirkin [68].

**Table 3.3:** Orientation constants for calculating distance errors

<b>AuNP size (diameter nm)</b>	<b><math>\theta</math> degrees from normal</b>	<b>Packing Density</b>
2	0	2.41
3	0	2.36
4	0	2.30
6	0	2.20
8	0	2.1
13	23.3	1.82
16	31.67	1.64
20	39.07	1.45

**Table 3.4.** Theoretical and experimental NSET values for FAM and Cy3B

Donor	AuNP Radius (10 <sup>-7</sup> cm)	AuNP Extinction (M*cm) <sup>-1</sup>	d <sub>0</sub> expt'l (Å)	d <sub>0</sub> theor y (Å)	$\epsilon_2 = \epsilon_2' + i\epsilon_2''$		$\epsilon_2$   <sup>2</sup>	$\delta_{skin}$ (10 <sup>-7</sup> cm)
					$\epsilon_2'$	$\epsilon_2''$		
FAM	0.945	2.45 x 10 <sup>5</sup>	72.5	73.4	-2.98	8.36	78.68	34.00
$\lambda_{Max}=520nm$ $\phi=0.8$ $n_r=0.62$	1.50	1.98 x 10 <sup>6</sup>	106.2	110.5	-3.17	8.03	74.53	34.27
	2.15	4.58 x 10 <sup>6</sup>	115.6	124.7	-4.69	5.06	47.55	34.39
	2.65	1.0 x 10 <sup>7</sup>	147.0	144.0	-4.86	4.57	44.51	34.47
	3.30	2.76 x 10 <sup>7</sup>	183.0	175.7	-4.98	4.16	42.14	34.55
	4.00	5.13 x 10 <sup>7</sup>	207.0	195.6	-5.06	3.86	40.50	34.62
	8.25	4.88 x 10 <sup>8</sup>	320.8	286.7	-5.20	3.15	36.98	34.84
Cy3B	0.945	1.36 x 10 <sup>5</sup>	57.6	57.3	-5.61	9.09	114.05	31.79
$\lambda_{Max}=570nm$ $\phi=0.7$ $n_r=0.31$	1.50	1.24 x 10 <sup>6</sup>	108.0	89.2	-7.29	6.22	91.83	31.24
	4.00	2.40 x 10 <sup>7</sup>	160.0	147.4	-8.52	3.17	82.64	30.58
	8.25	2.54 x 10 <sup>8</sup>	224.0	222.0	-8.72	2.23	80.98	30.48

### 3.3.3 Experimental Considerations

The loading level of DNA is assumed to be stochastic but can be controlled from one DNA per AuNP to full NP coverage by controlling the stoichiometry of the reaction. For the energy transfer efficiency studies, a single displacement is utilized for AuNPs < 2 nm radii, while complete displacement of the phosphine is utilized for AuNPs > 2 nm radii to improve collection efficiencies. On the 2nm and 4nm radius AuNP, loading level dependent quenching was analyzed to ensure no loading level effect on the quenching behavior. Since it has been experimentally demonstrated that the LSPR frequency for the AuNP can be influenced by the passivating ligand head group, and the magnitude of the shift will be dependent on the metal NP size and the degree of surface passivation [58]. The shift in LSPR frequency arises from changes in the local dielectric environment of the AuNP, which may lead to changes in the resonant coupling of the fluorescent molecule oscillator with the AuNP).

Inspection of the absorption spectra in Figure 3.4 for 4.0nm radius AuNPs as a function of the DNA loading levels reveal that a < 1 nm shift is observed for single labeling of DNA on a AuNP for all sizes. When the surface is completely passivated by the DNA a shift of ~ 2 nm is observed for 8.25 nm radius AuNP.

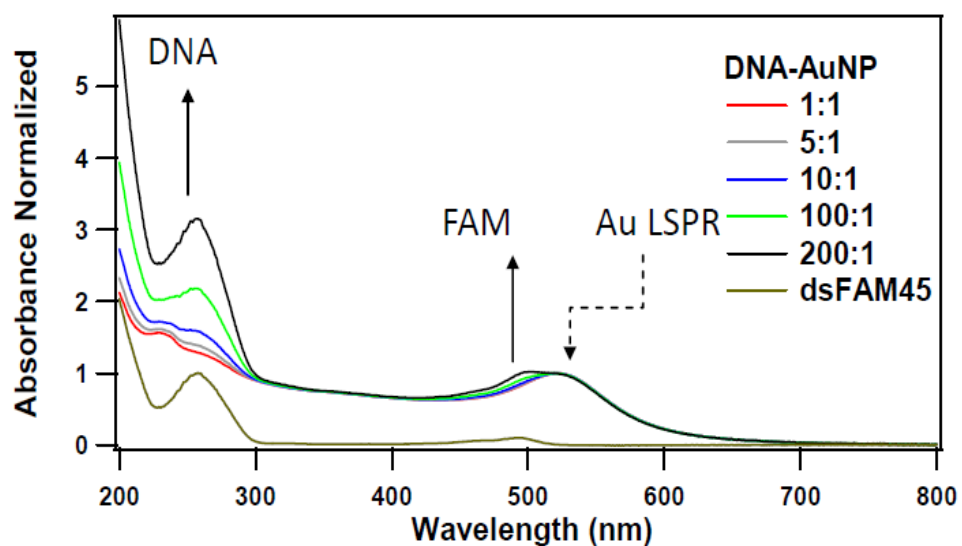
Besides loading levels there are a few other considerations that must be taken into account. For the developed model it is assumed that only AuNPs of a single size are present, but it is clear to see from the TEM analysis given in Chapter Two that this is not the case. Although the size distribution in AuNP is nearly Gaussian, the effect on quenching will not be a normal Gaussian statistics problem; for instance a dye in resonance with the plasmon will exhibit an  $\text{Eff} \propto \epsilon_{\lambda}^4$  and a size dependence that will track to the  $r^3$  power. In addition, as was previously discussed the extinction coefficient of the AuNPs is size dependent, therefore a distribution of

sizes results in a weighted distribution in the cross-section for coupling of the donor dye to the AuNP. The quenching results would be weighted towards the larger AuNPs in each experiment. The error caused by this will be visualized by an imperfect match between experimental and theoretical observations. The best fits to experimental data using equation 3.6 indicates the maximum error of <10%. The error that arises from the size dispersity could be accounted for with a correctional factor but would result in the loss of the simplicity of use for the average biomolecular researcher. Furthermore, in recent years there have been significant improvements to the synthesis of nanoparticle yielding a <5% size distribution for nearly all sizes. This negates the need to build a distribution function to account for what would need to be a batch to batch correctional factor [112].

Another source of deviation in the efficiency curves may be caused by the absence of a J-overlap integral from the developed theory. In fact, no model to date that attempts to explain the coupling behavior of a fluorescent dipole to a metal nanoparticle has been able to incorporate a J-overlap integral in the calculation. Instead every available model has assumed a resonance condition is met between the donor dye and accepting nanoparticle which allows the math of the integral to be left out. This assumption is utilized in the developed model.

The inclusion of a J-overlap integral and the size dispersity for the AuNP should improve the statistics, but for a purely theoretical approach are corrections that are statistically meaningful but difficult to compose. A compelling comparison of the derived model to existing models illustrates the dramatic improvement the size dependent NSET model offers over the available models, illustrated in the residual graphs in Figure 3.5. The residuals are generated of between the “best fit” efficiency plots and the available models. The Chew model was derived from the GN-model and over estimates the scattering component of the AuNPs.

a)



b)

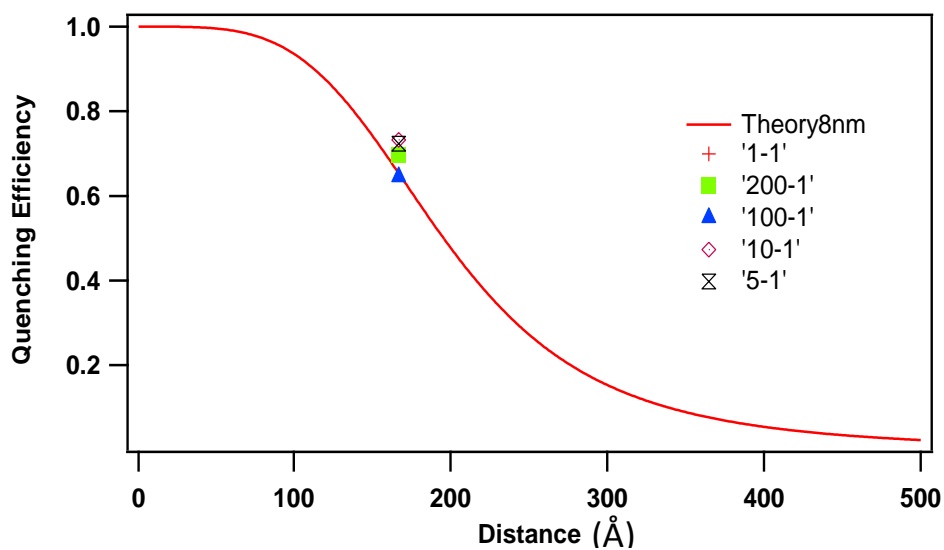
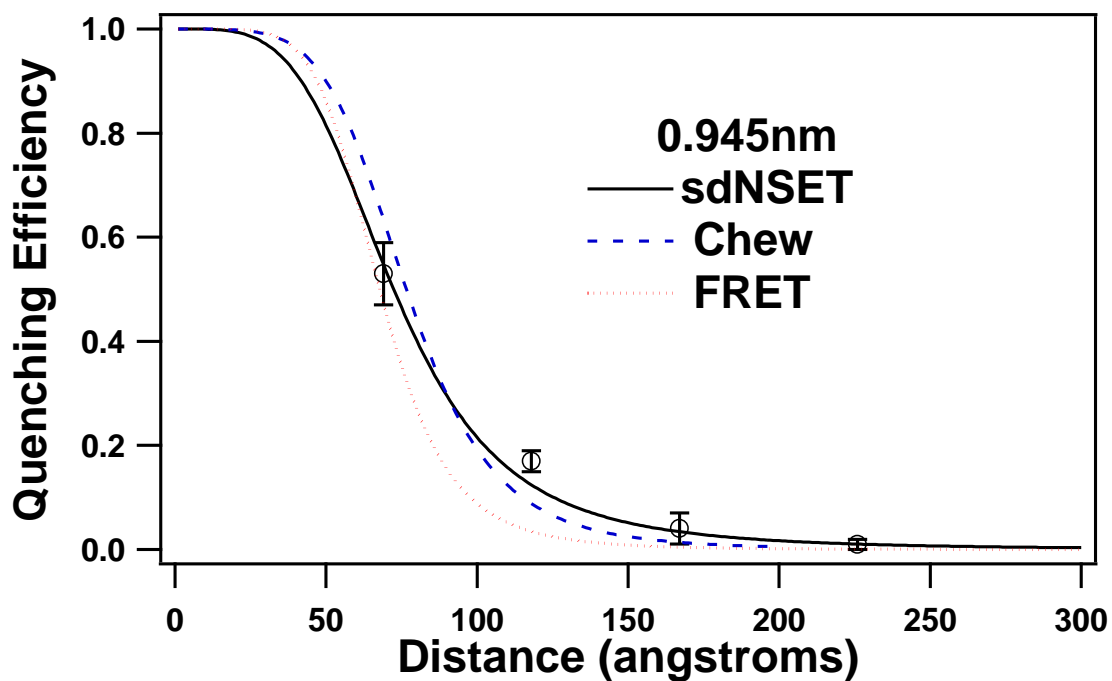


**Figure 3.4** a) Absorption spectra of 4.0nm AuNP with different loading levels of FAM labeled DNA strands. b) Energy transfer efficiencies of the different loading levels of DNA on 4.0nm AuNP



a)

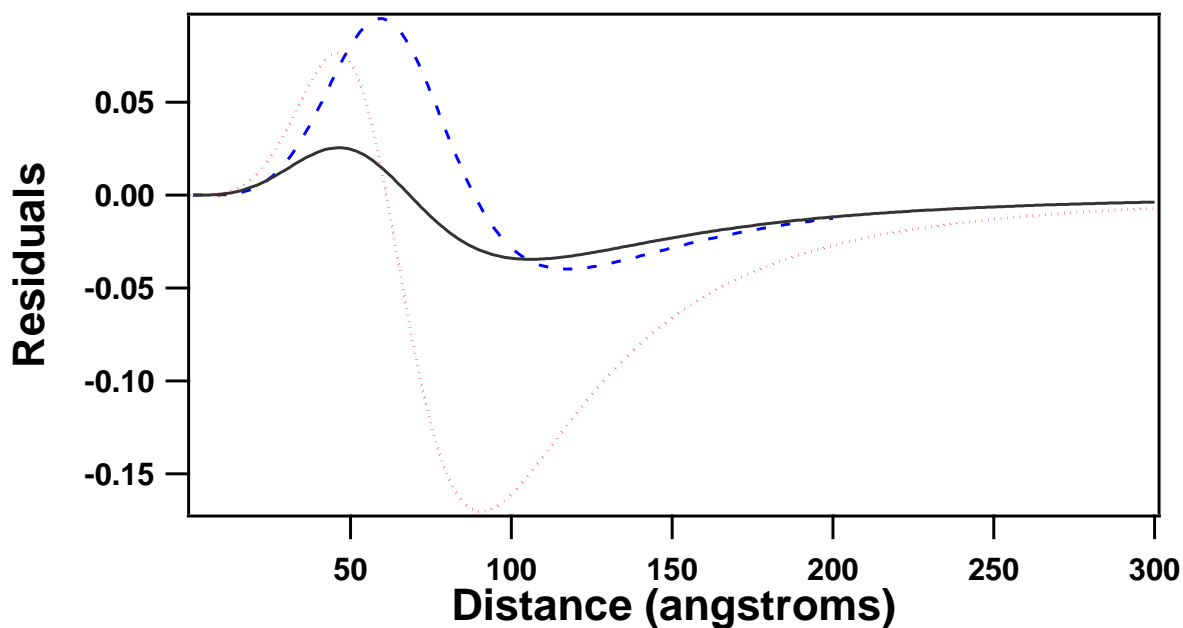


**Figure 3.5** Theoretical size dependent efficiency curves, for the developed model as well as two other leading theories, and experimental values for selected separation distances for FAM as an excited state donor to AuNP with radii of (a)  $0.95 \pm 0.18$  nm, (b)  $1.5 \pm 0.30$  nm, (c)  $2.16 \pm 0.55$  nm, (d)  $2.65 \pm 0.45$  nm, (e)  $3.3 \pm 0.5$  nm, (f)  $4.0 \pm 0.3$  nm, and (g)  $8.25 \pm 1.20$  nm, along with the residual plots for each size. (h) All sizes overlaid (i) All sizes overlaid for the Cy3B

b)

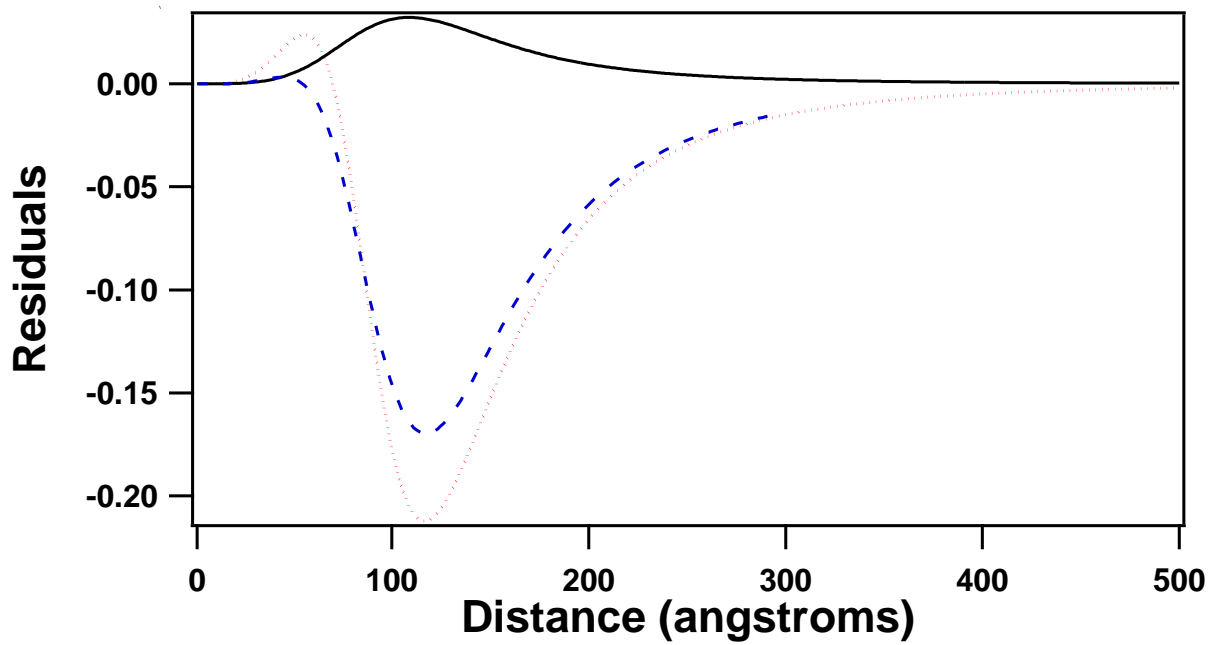
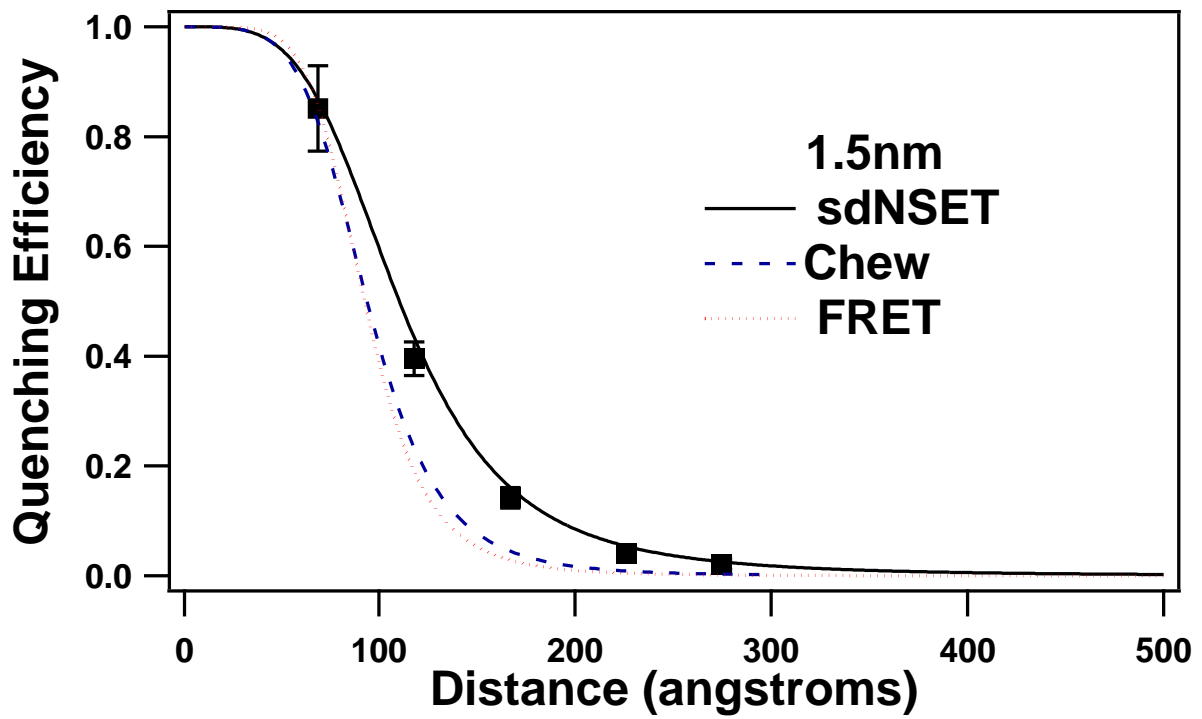


(Figure 3.5 continued)

c)

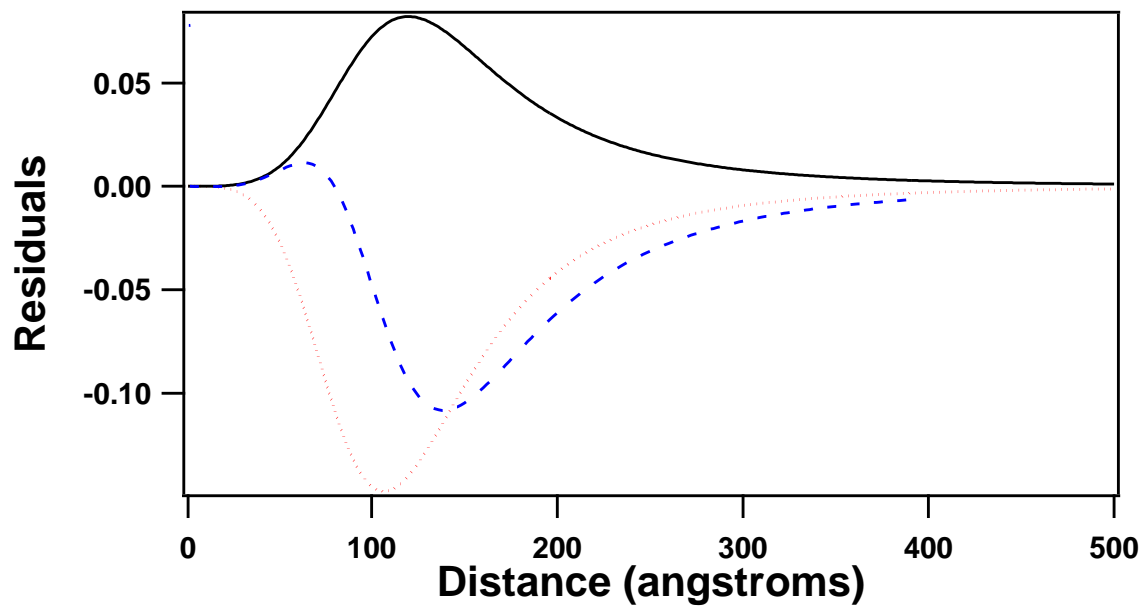
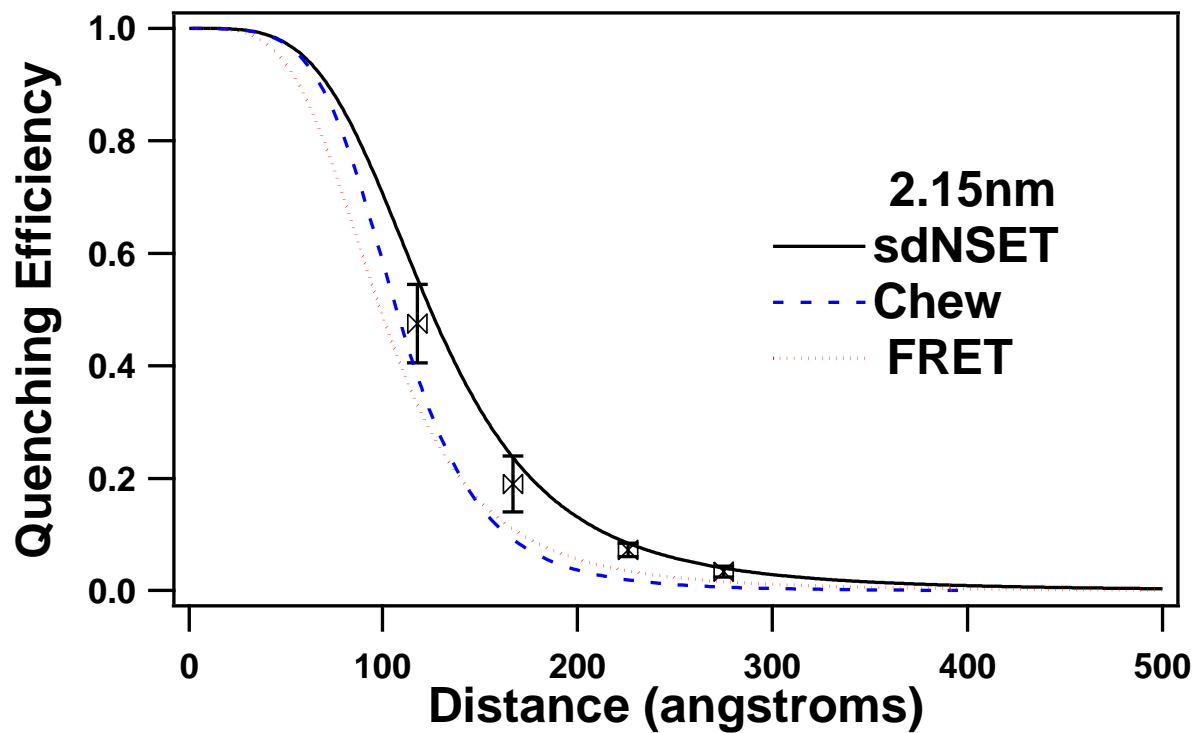


(Figure 3.5 continued)

e)

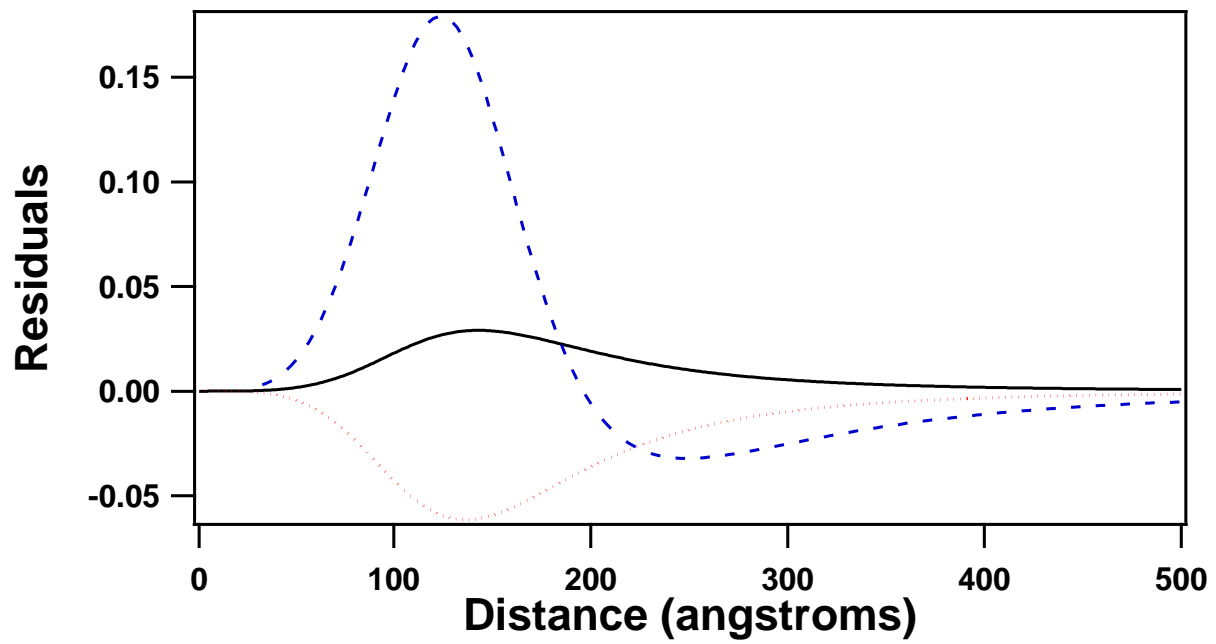
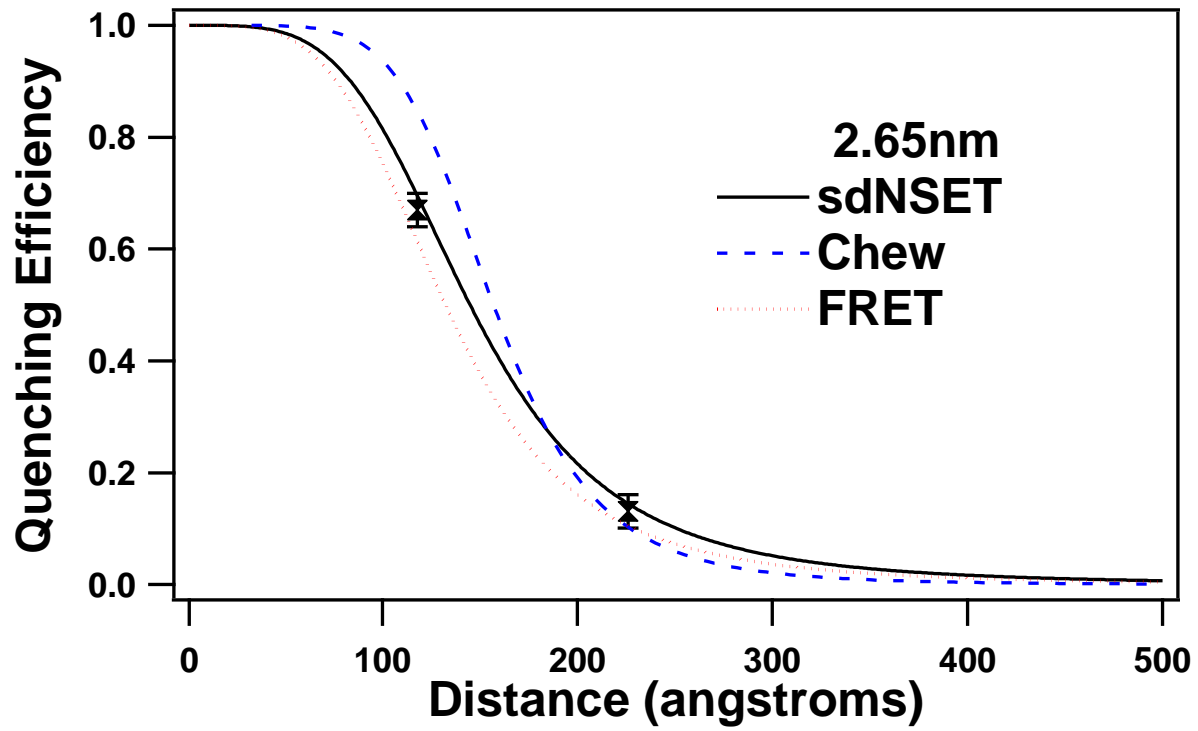


(Figure 3.5 continued)

e)

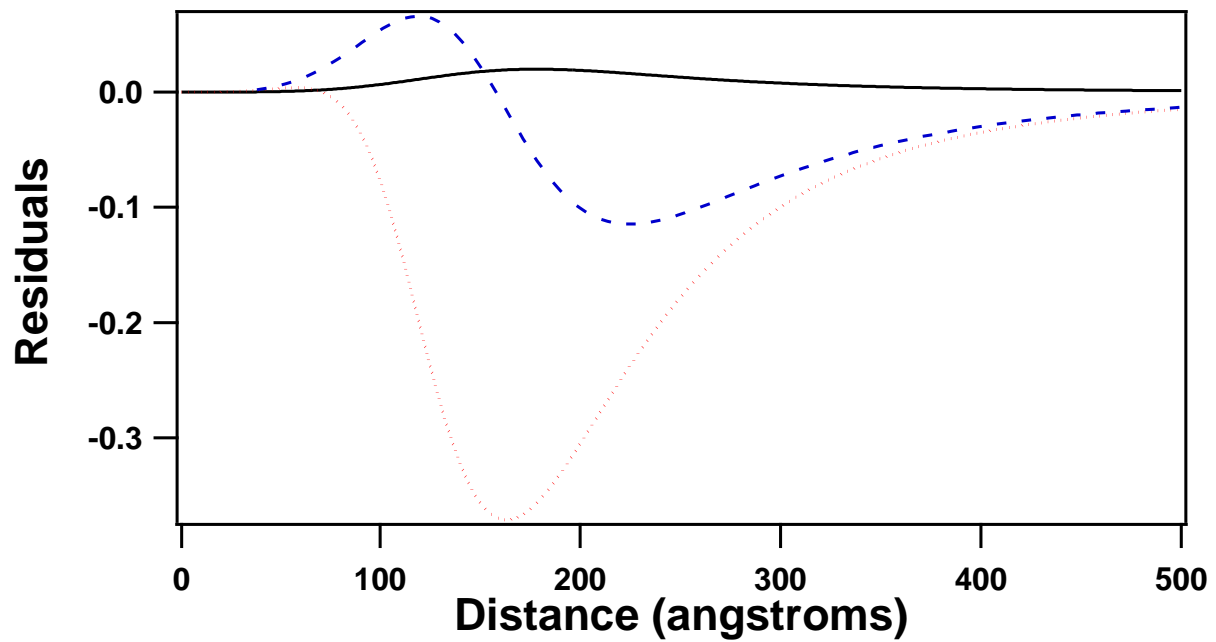
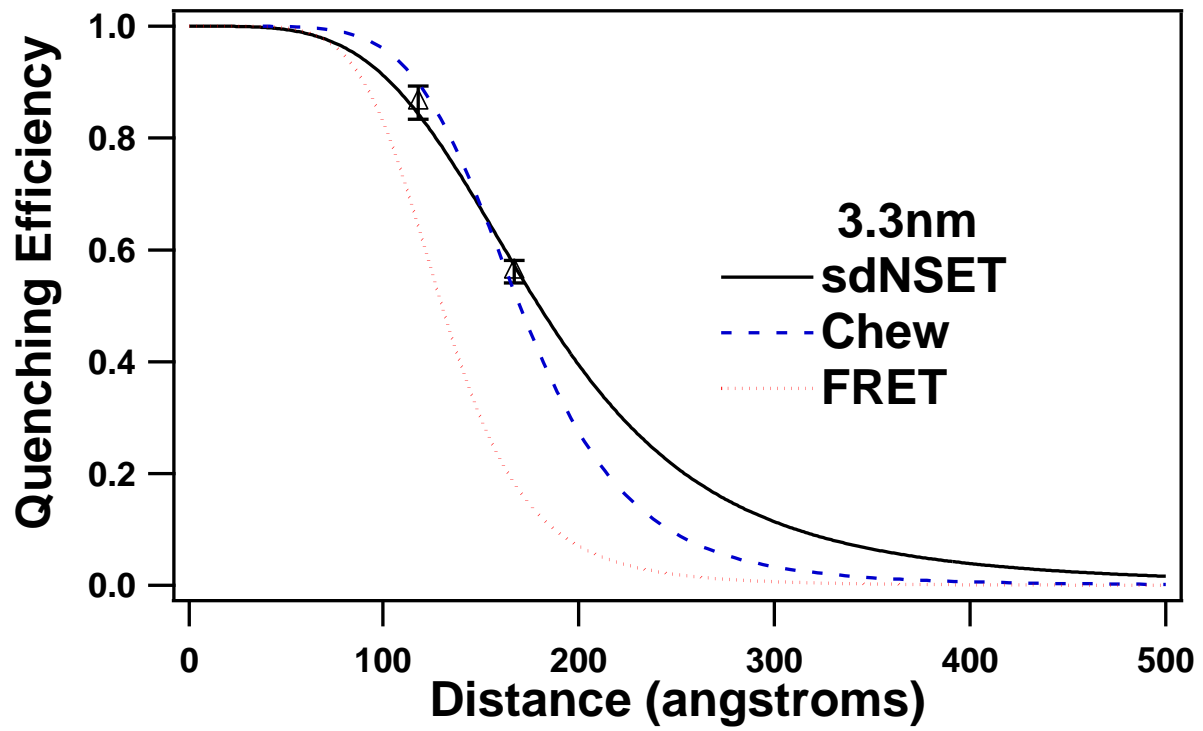


(Figure 3.5 continued)

f)

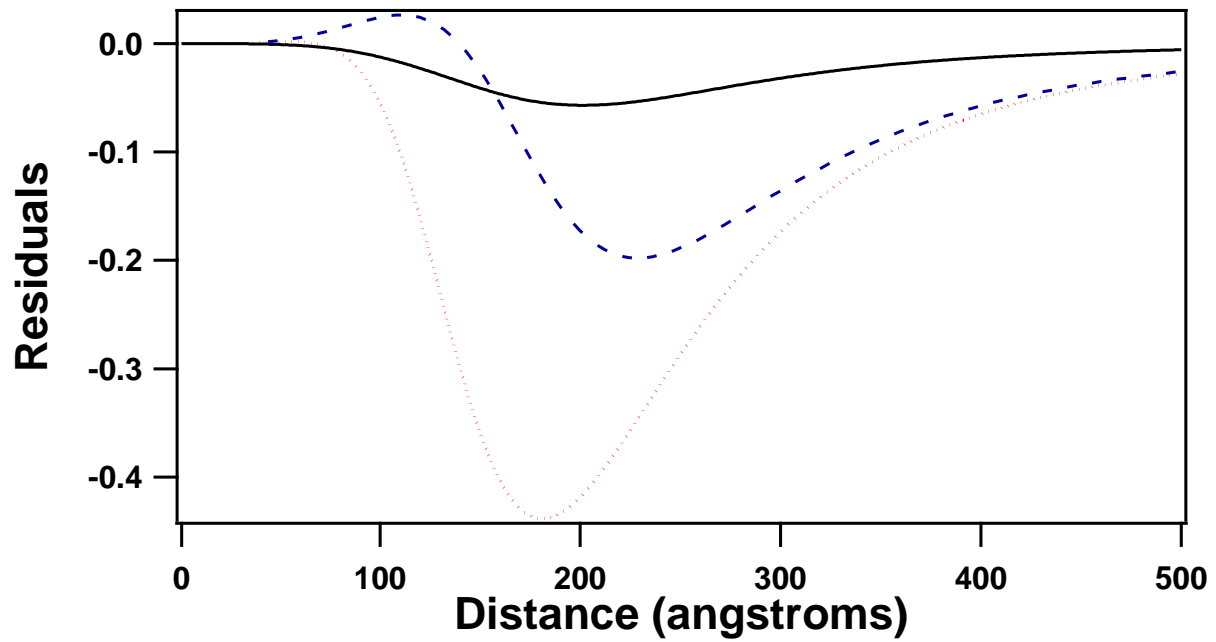
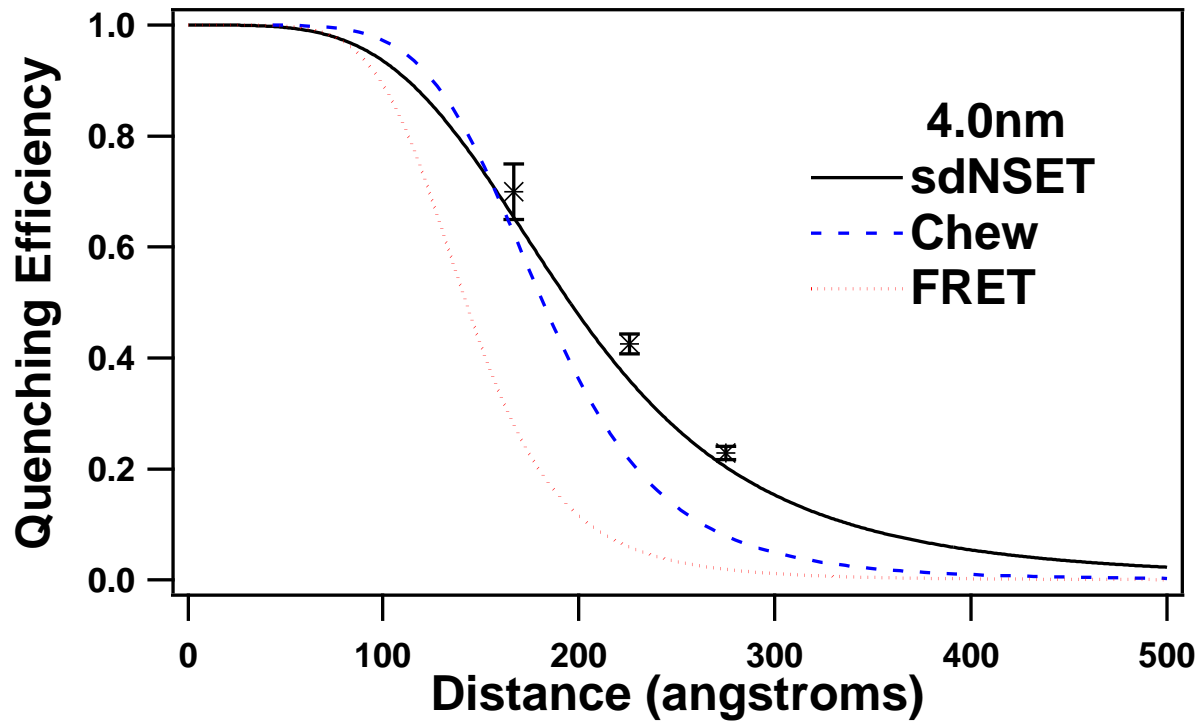


(Figure 3.5 continued)

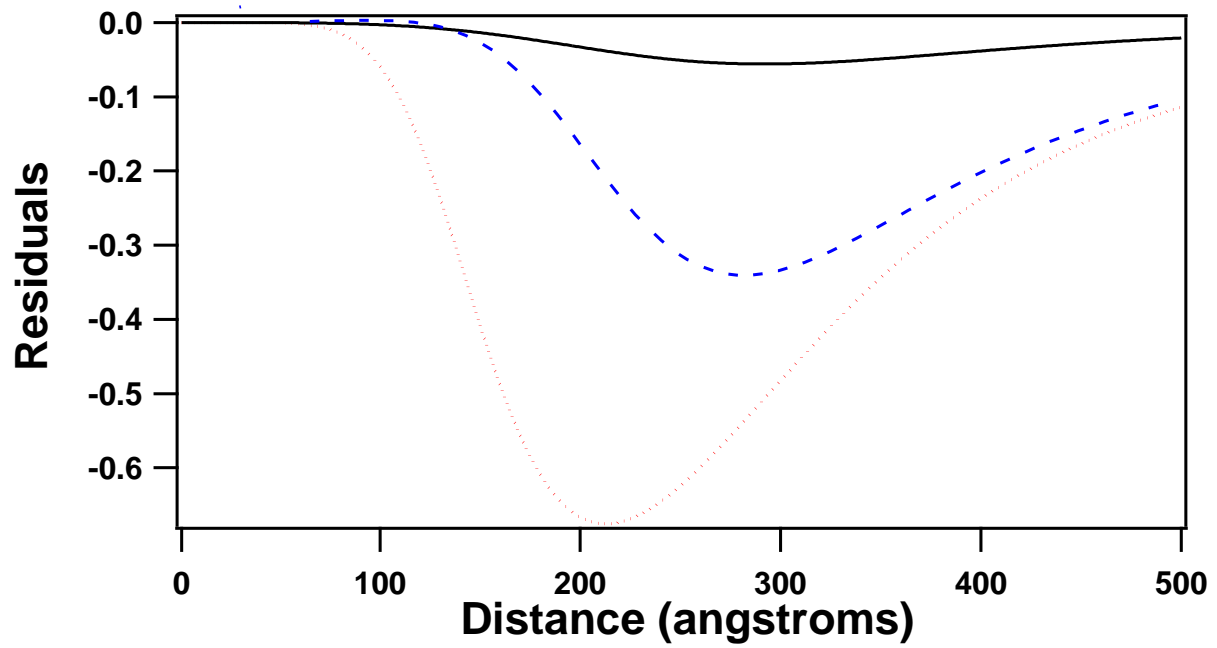
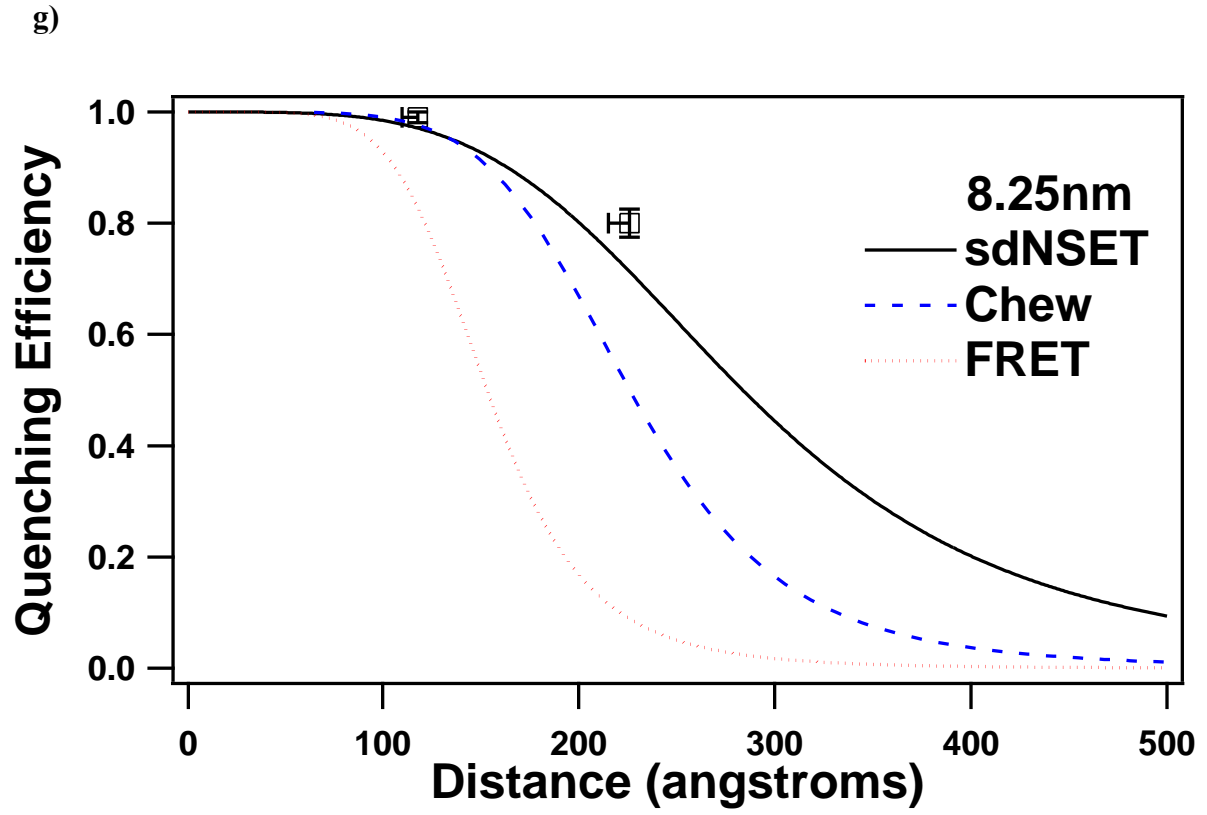
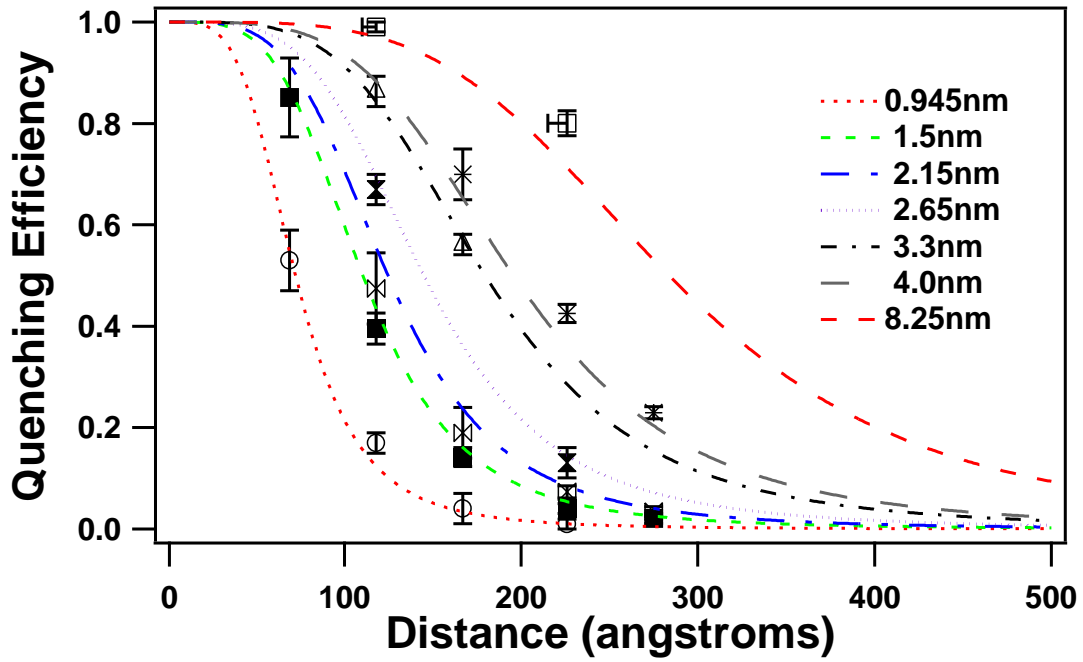


(Figure 3.5 continued)



h)

i)

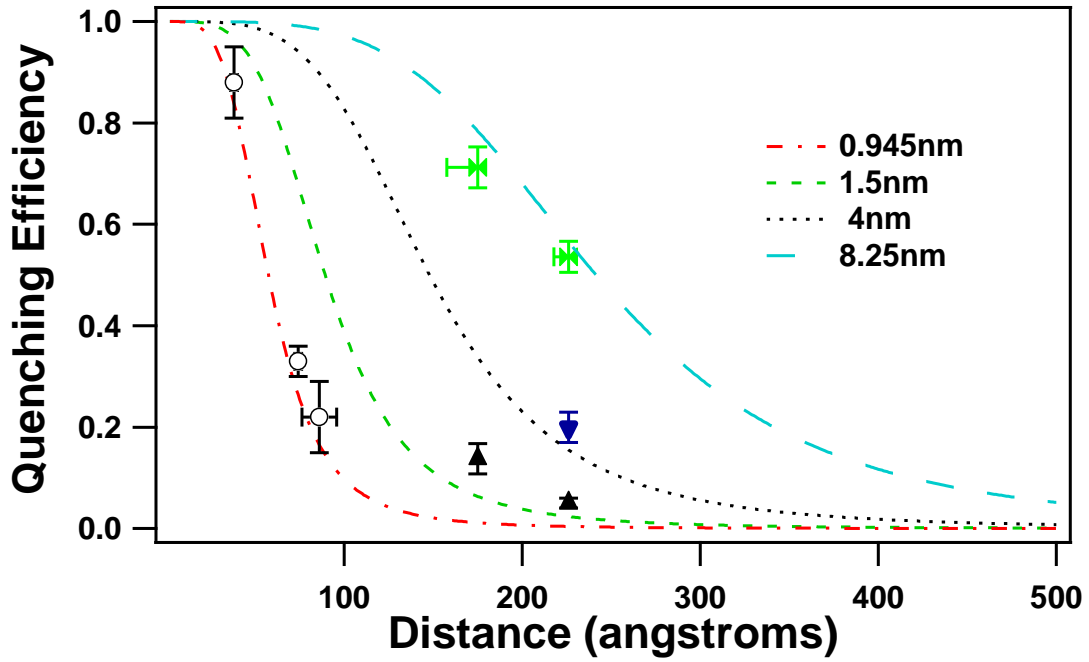


(Figure 3.5 continued)

It also treats the LSPR of the AuNP as a large dipole which results in the model having a native  $1/d^6$ . The model is originally calculated for separation distances that include the radius of the accepting nanoparticles since the plasmon is considered a dipole. For simplicity sake Figure 3.5 has had the radius subtracted from each point for direct comparison to the distance dependence with the developed model, which reports separation distances between donating dipole and the surface of the AuNP.

A FRET derived model was also used to compare the developed size dependent NSET model. The assumptions made for this model treat the AuNP as a zero-point dipole and again are solved for distance separations that include the radius of the NP. Once again, in order to make a direct comparison to the size dependent NSET model the radius of the particle has been subtracted from the distances to account for only the distance between the dipole and the surface of the AuNP. These two models, Chew and FRET, were used to compare the derived model because they represent the models that predict the most accurate  $d_0$  values when compared to experimental observations.

It is clear from the residuals in Figure 3.5 that the developed size dependent NSET model dramatically increases the accuracy and precision between the experimental observations and theoretically predicted quenching efficiencies. This is most likely due to fact that it is incorrect to treat plasmonic nanoparticles as dipoles, especially has size is decreased below the mean free path of the electrons and the LSPR begins to broaden out, as is done in the FRET and Chew models. By incorporating the size dependent absorptivity and dielectric function, the developed model has been able to not only correctly predict the  $1/d^4$  distance dependence but has also shown accurate prediction of the actual quenching efficiencies at distinct distances from the AuNP surface. The deviation in the data for the smaller particles can be attributed to large size

dispersity, coupled to the volumetric dependence ( $r^3$ ) of the extinction coefficient. This dispersity gets better with increasing particle size but as the particles approach 20nm in radius, it is believed the deviation for the largest sample (8.25nm radius) arise from contributions from the scattering component of the dielectric function or potentially due to a change in the tilt angle of the DNA stands relative to the surface of the AuNP. Further studies are required to account for the scattering of these larger particles.

### **3.3.4 Photoluminescent Quenching Results**

The AuNP size and separation distance dependent PL quenching behavior for FAM and Cy3B are plotted in Figure 3.6 a-g and Table 3.5. In Figure 3.6, the experimental data is plotted in terms of quenching efficiency vs. fluorophore-AuNP separation distance. The experimental data and theoretical predictions are summarized in Table 3.4. Inspection of the FAM (Figure 3.5(a-h)) and Cy3B (Figure 3.5 (i)). The experimental data shows strong agreement between theory and experiment for FAM for all AuNP sizes and separation distances. Plotting the experimental  $d_0$  values onto the theoretical  $d_0$  predictions in Figure 3.1 illustrates the quality of agreement between theory and experiment further validating the model. The results strongly support the incorporation of size dependent dielectric constants (eqn 3.2) and the redefinition of absorptivity (eqn 3.4) to accurately predict the AuNP size dependent trends for energy transfer from a fluorescent molecule to a AuNP.

## **3.4 Conclusion**

The interaction of an oscillator with a AuNP can be accurately described within the image dipole approximation if the size dependent electronic properties for a AuNP are properly incorporated.

**Table 3.5** Lifetime values for Cy3B quenching studies by AuNP

Complex (DNA bp-Au radius)	$k_1(\tau \text{ ns})$	$A_1$	$k_{ex}(\tau \text{ ns})$	$A_{ex}$	$C$
Cy3B	0.4 (2.5)	0.95	-	-	0.01 2
45bp-Au1.5nm	0.47 (2.1)	0.79	-	-	0.01 5
60bp-Au1.5nm	0.42 (2.376)	0.64	-	-	0.40
60bp-Au4.0nm	0.5 (2.0)	0.94	-	-	0.21
45bp- Au8.25nm	1.38 (0.72)	0.59	0.4 (2.5)	0.38	0.03 0
60bp- Au8.25nm	0.86 (1.16)	0.94	-	-	0.01 0

a)

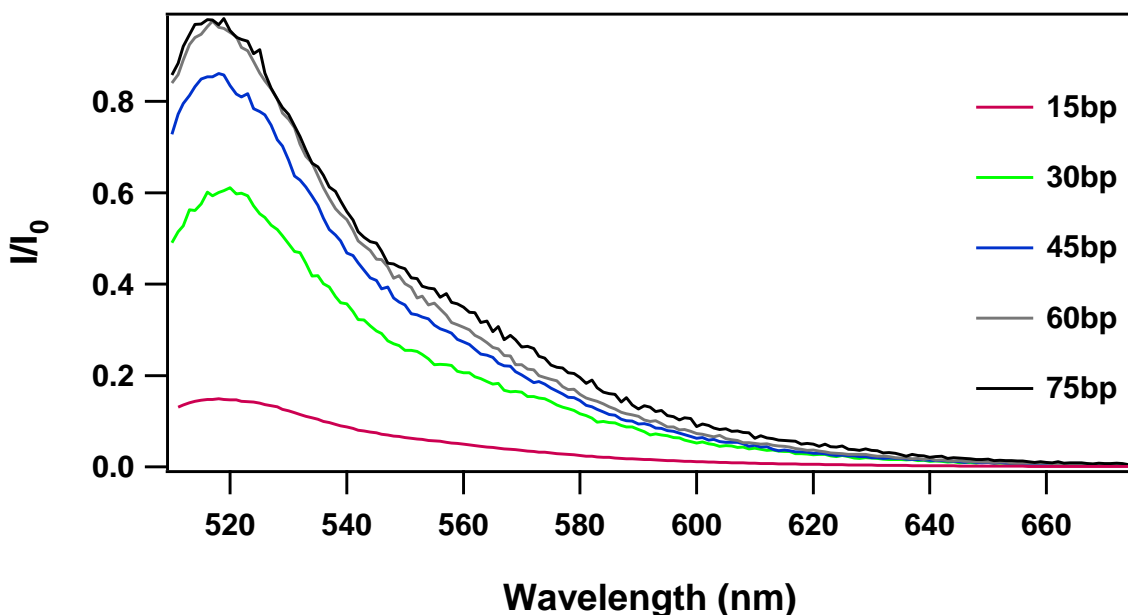
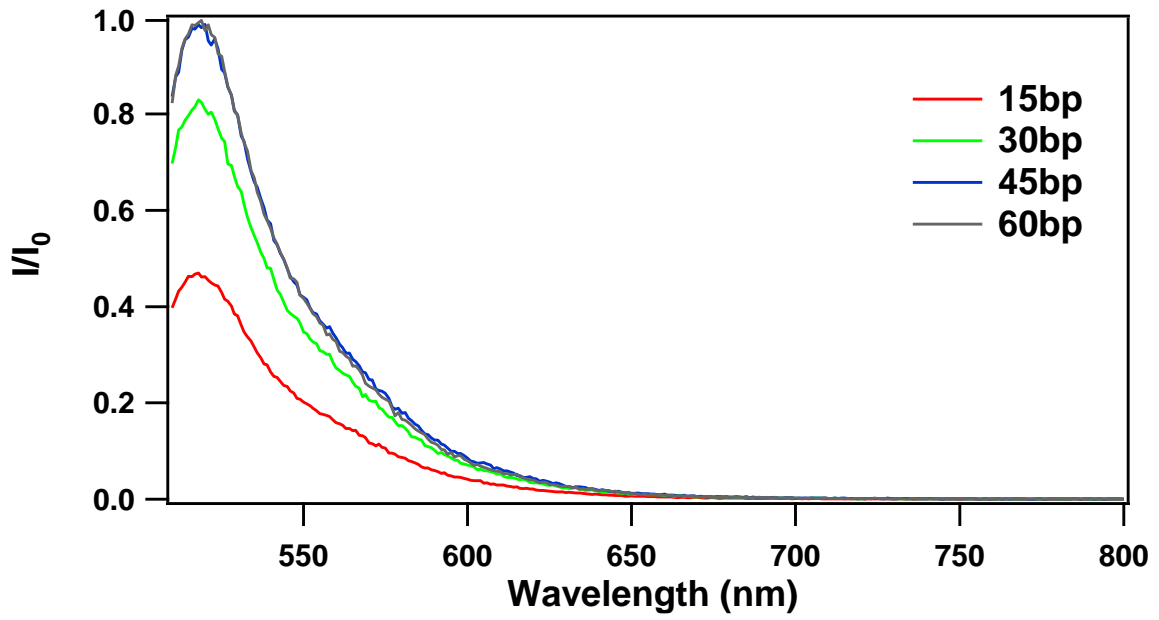


**Figure 3.6** a) DNA length dependent FAM quenching data for 0.945 nm radius AuNP b) DNA length dependent FAM quenching data for 1.5 nm radius AuNP c) DNA length dependent FAM quenching data for 2.15 nm radius AuNP d) DNA length dependent FAM quenching data for 2.65 nm radius AuNP e) DNA length dependent FAM quenching data for 3.3 nm radius AuNP f) DNA length dependent FAM quenching data for 4.0 nm radius AuNP g) DNA length dependent FAM quenching data for 8.25 nm AuNP

b)



c)

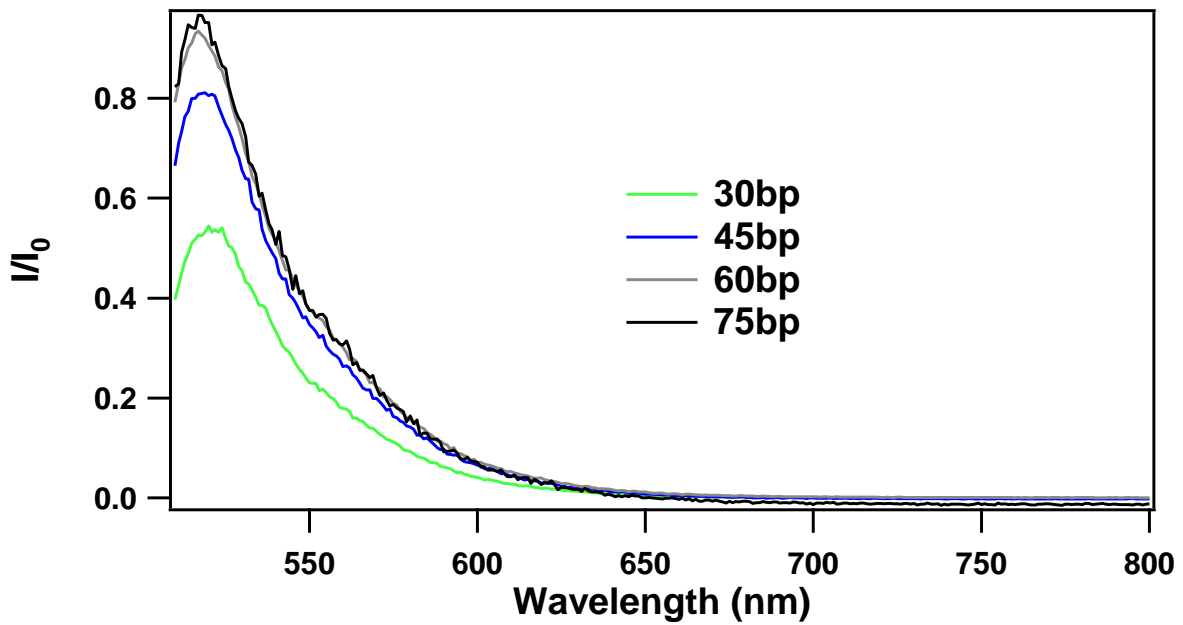
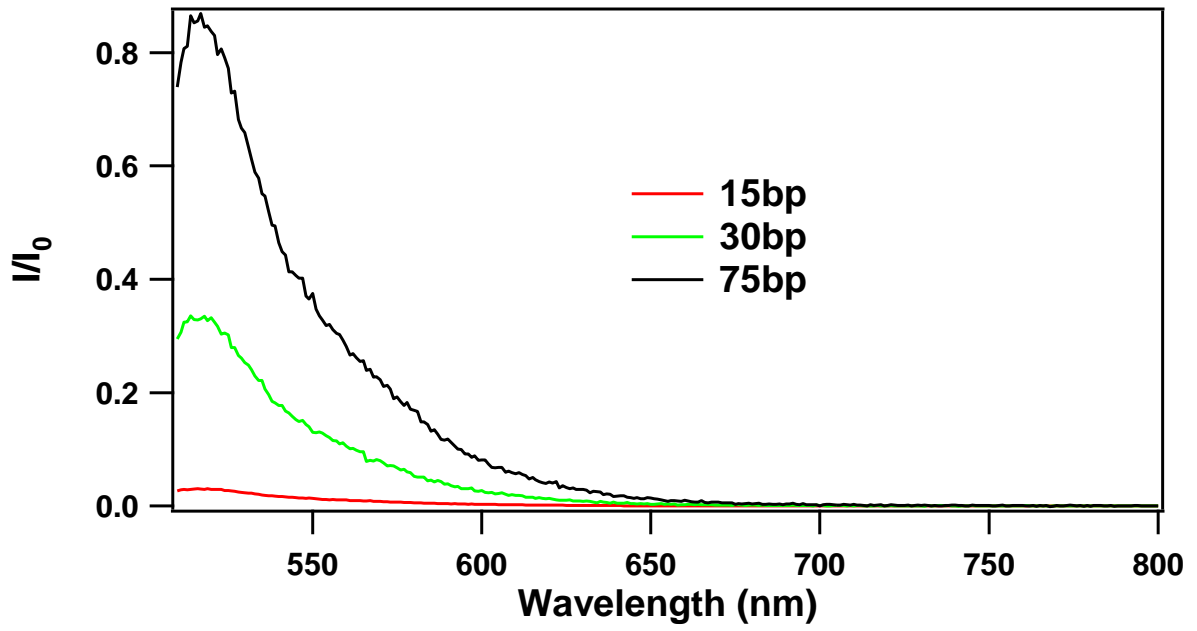


(Figure 3.6 continued)

d)



e)

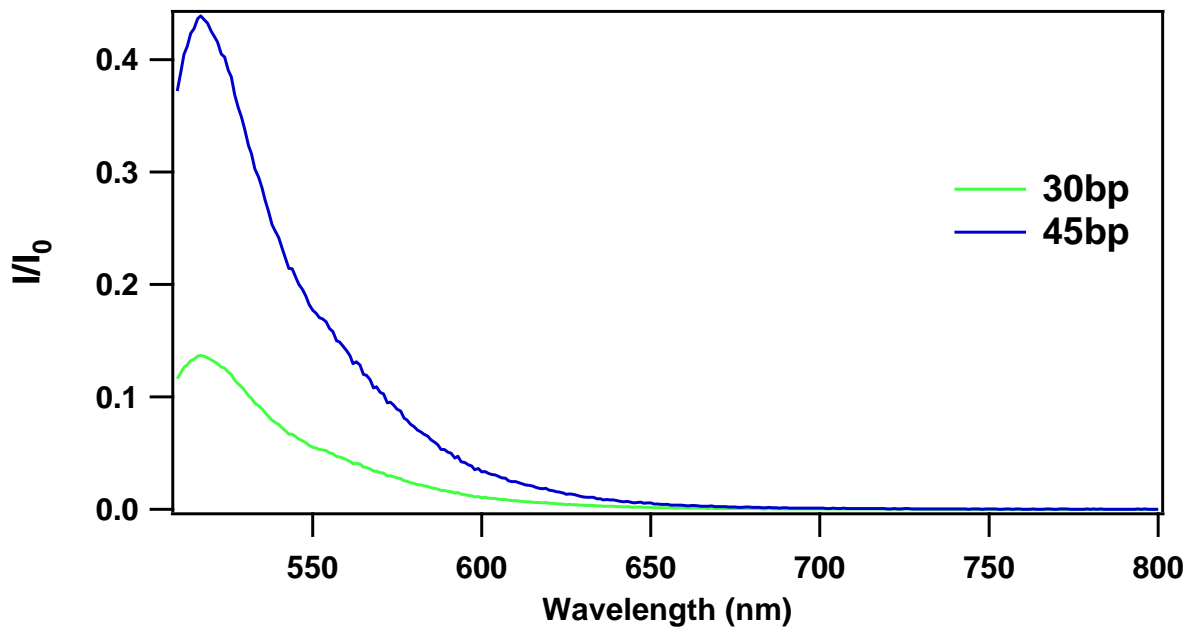
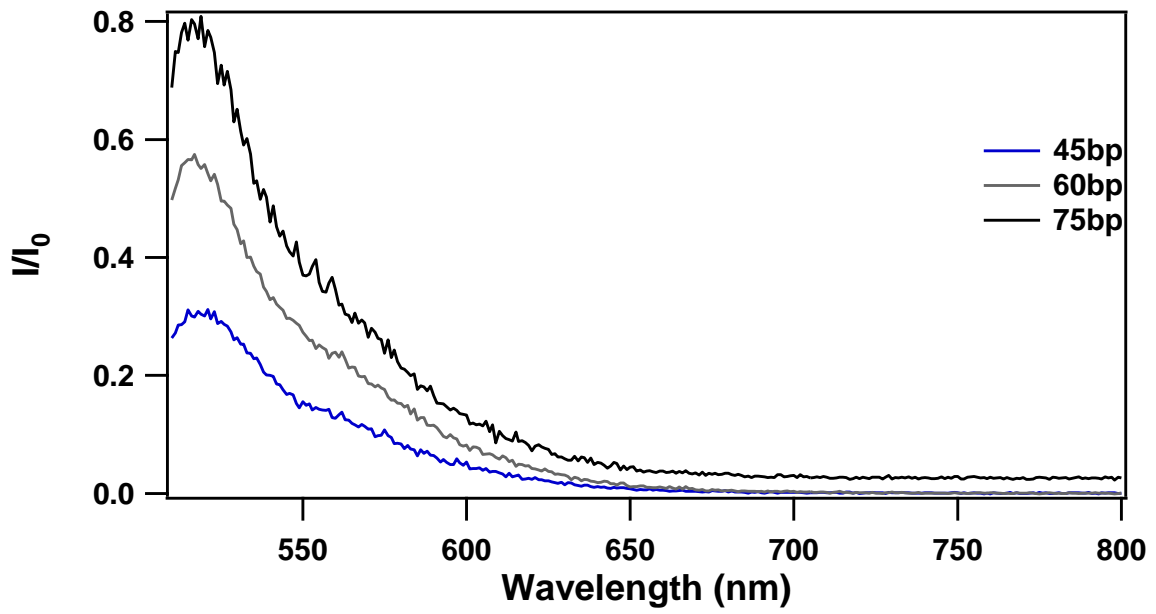


(Figure 3.6 continued)

f)



g)

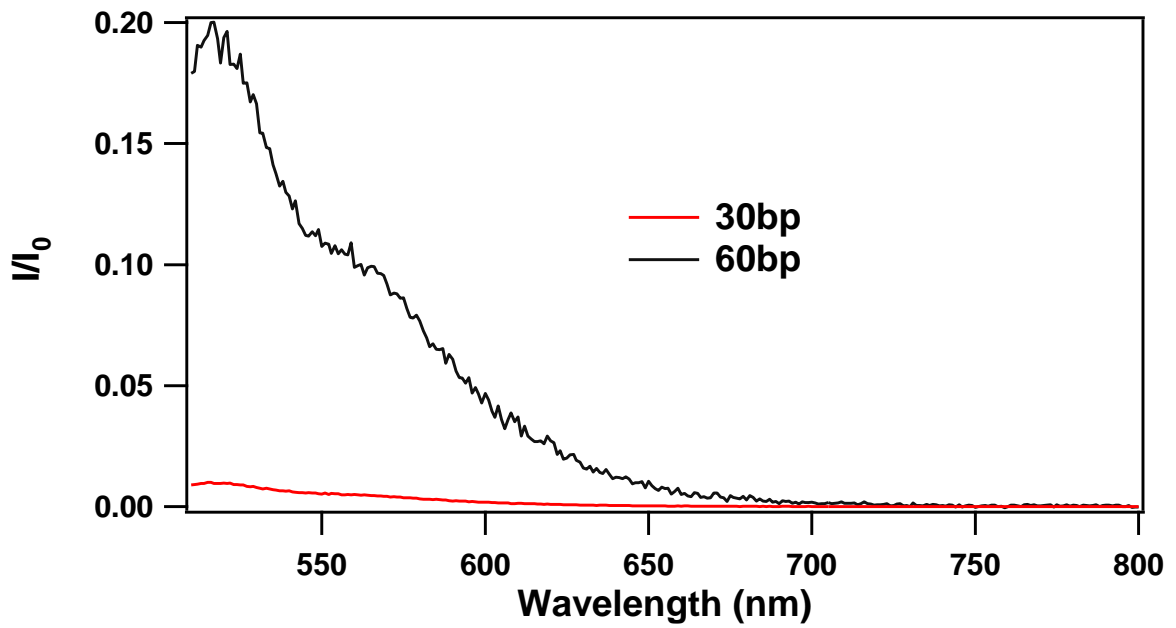


(Figure 3.6 continued)

The image dipole approximation, which incorporates radiative and non-radiative rates, correctly describes the observed fluorescent behavior of a dye as a function of its separation distance from the metal surface. The developed size dependent NSET model in this manuscript accurately predicts experimental data collected for AuNP sizes between 0.95 and 8.25 nm radii interacting with excited state oscillators in resonance and near resonance with the LSPR of the AuNP. The careful measurement of the size dependent quenching of the excited state of molecular fluorescent molecules by AuNPs up to 8.25nm demonstrates that the observed size dependent quenching behavior can be understood in terms of the modification of the non-radiative effects within this size range without inclusion of radiative rate modification. More importantly, the as derived size dependent NSET expression accounts for the reported shift in  $d_0$  values observed by others as the AuNP increases in size.

NSET provides an important predictive model for scientists using AuNPs as energy transfer reporters, whether in biophysics or molecular chemistry. The correlation observed between theory and experiment demonstrates the validity of the derived size dependent NSET model when the correct terms for  $\epsilon_2$  and  $A$  are incorporated. The developed model can be used to generate curves for other fluorescent molecules and is currently being explored to test the validity of the model for other metals. New experimental studies and derivation of the theorem are currently being pursued to provide an analytically predictive model for other shapes, sizes, and metal compositions.

# CHAPTER FOUR

## SUPER QUENCHING OF BLUE DYES

### 4.1 Introduction

AuNPs are very important in the biophysical toolbox with applications in resonant energy transfer (RET) spectroscopy to surface enhanced RAMAN spectroscopy (SERS), optical sensors, bio-diagnostics, and use in drug delivery platforms[70, 1, 71, 72, 73, 2]. The use of AuNPs in biotechnology reflects their ease of synthesis, ability to be functionalized, and stability. One of the most useful characteristics of AuNPs is known as the localized surface plasmon. The LSPR in AuNPs arises from the oscillation of the free electrons producing a strong electric field at the surface, which is extremely sensitive to ligand passivation, particle size, shape and environment. These induced oscillation has been dubbed the intraband transitions and have been studied extensively.

In this chapter the enhanced quenching of fluorescent molecules by the higher energy interband transitions of 2nm AuNPs will be discussed. This enhanced quenching of an excited state fluorophore is attributed to the interactions between the excited state wavefunction and the higher energy, size-independent interband ( $d \rightarrow sp$ ) transition in Au, in addition to the size-dependent intraband transitions (the LSPR) [74, 9, 75, 76, 77]. This coupling, which leads to the observation of a competition between radiative enhancement and radiative quenching depends on the composition, size, and shape of the nanoparticle [74, 80, 60, 76, 78, 81, 82, 83, 84]. There have been extensive studies that have looked at the quenching of fluorophores by the LSPR of AuNPs, and found to follow the frequency dependence of a 2nm AuNP absorption spectra [31, 32, 33, 19, 29, 76, 78]. Fluorophores whose emission does not overlap with the absorption spectra of the AuNPs did not show any quenching while the one whose emission overlaps with

the LSPR show a quenching behavior with a  $1/d^4$  distance dependence as predicted by the NSET model [31, 32, 19].

The intensity of interband transitions ( $d \rightarrow sp$ ) increase exponentially above the LSPR band [63, 76]. These transitions are strongly absorptive in nature and likely the major contributor to quenching of molecular dyes in the far field. The quenching behavior of molecular dyes with emission blue of the LSPR is important since coherent coupling with the interband transition should be destructive leading to strong quenching of the excited state intensity, but has received only limited attention [76, 79]. In this chapter, the quenching behavior for Alexa Fluor 350 (AF350) by the  $d \rightarrow sp$  interband transition will be investigated. The photoluminescence (PL) of AF350 ( $\lambda_{em} = 440$  nm) overlaps strongly with the interband transition and is higher in energy than the LSPR in 2 nm Au ( $\lambda_{LSPR} = 520$  nm). The use of 2 nm AuNP allows the interband effect to be probed without interference from a large scattering contribution from the intraband (LSPR) that may be present in larger AuNPs, since 2 nm AuNPs exhibits a weak, intraband contribution with no significant scattering [33].

## 4.2 Materials and Methods

The dye coupled DNA strands used in this study were purchased from Midland Oligos Inc. and the sequences are given Table 4.1. The complementary strands were annealed together by heating them in 20 mM PBS 100 mM NaCl pH7.5 buffer to 95 °C for 2 min and then cooling to room temperature. The annealed ds-DNA was treated with dithiothreitol (DTT) to deprotect the thiol linker and then passed through a NAP-V column to remove the excess DTT and protecting group. The deprotected ds-DNA is instantly mixed with a solution of BSPP coated 2 nm AuNPs such that the DNA: Au ratio was 1:1.1. The unreacted AuNPs were removed by ethanol precipitation. The steady state experiments were conducted on a Varian Cary Eclipse

Fluorescence spectrophotometer respectively at  $293\text{K}\pm 2\text{ K}$  in 20 mM PBS buffer, 0.1 M NaCl, pH7.5 with  $\lambda_{\text{ex}} = 350\text{ nm}$ . The Stern-Volmer studies were conducted by keeping the concentration of the AF350 labeled strands constant at (0.175mM) and varying the concentration of the 2nm AuNPs from 0.245mM to 0.05 mM. Figure 4.1 illustrates how this study hopes to track quenching of AF350 as the dye is positioned through the near field and into the far field.

### 4.3 DNA Complex Results

The coupling to the excited state of the dye by the AuNP comes from the resonance of the absorption of the AuNP with the emission of the dye. AF350 has an absorption maxima  $\lambda_{\text{abs}} = 350\text{ nm}$ , and an emission maxima  $\lambda_{\text{em}} = 440\text{ nm}$ . The extinction spectra of the AuNP is comprised of a size dependent LSPR band (intraband transitions) and a size independent  $d \rightarrow sp$  (interband) transitions. This study will look at coupling to the interband transition which is blue of 520nm. Ignoring the ligand contributions ( $\lambda_{\text{BSPP}} = 250\text{ nm}$ ) to the observed extinction spectra for a AuNP, the intraband ( $\lambda_{\text{SPR}} = 520\text{ nm}$ ) and higher lying interband contribution to the total dielectric function of the metal can be expressed as equation (4.1), such that, [9, 75]

$$\varepsilon_{\text{total}} = \varepsilon_{\text{intra}} + \varepsilon_{\text{inter}} = (\varepsilon'_{\text{intra}} + \varepsilon''_{\text{intra}}) + (\varepsilon'_{\text{inter}} + \varepsilon''_{\text{inter}}) \quad (4.1)$$

The real component,  $\varepsilon'$  describes scattering while the imaginary component,  $\varepsilon''$  absorptive. By using a 2nm AuNP the  $\varepsilon'$  term approaches zero for the energy range under investigation in this chapter. The  $\varepsilon_{\text{intra}}$  is calculated for a spherical particle using the Mie approximation assuming the Drude model where the free conduction electron cloud vibrates resonantly with the incident field against a positive background allowing  $\varepsilon_{\text{intra}}$  to be written as equation 4.2 [76, 77],

$$\varepsilon_{\text{intra}} = 1 - \frac{\omega_{p,\text{eff}}}{\omega(\omega + i\gamma_{\text{eff}})} \quad (4.2)$$

where  $\omega_{p,eff}$  is the effective plasma frequency and  $\gamma_{eff}$  is the damping rate for the collective oscillations (plasmon). The  $\epsilon_{intra}$  equation can be expressed in terms of a size dependent function following the approach of Kreibig [33, 9]. Kreibig determined  $\gamma_{eff}$  to be size dependent, which results in a broadening of the LSPR band with decreasing size [9, 33, 75].

The interband transitions described the direct excitation of core electrons in the AuNPs. These core electrons are strongly coupled to the positive nuclei that make up the lattice structure of the nanoparticles. Due to the extreme difference in mass between the core electrons and the nuclei, the Etchegoin approximations allow the positive charge of the nuclei to “spread out” as a background that effects all the core electrons equally. Since the core electrons feel the positive charge of nuclei directly, more energy is required to perturb them. Etchegoin’s approximations treat this relationship by introducing a dampening factor that is related to the positive charge of the nuclei [63]. This dampening factor is much larger in magnitude than the dampening exerted upon the Drude electrons discussed in the previous chapter. The dielectric function for the interband transitions is expressed in equation 4.3, [105, 111, 63]

$$\epsilon_{inter} = \sum_{i=1,2} \frac{A_i}{\omega_i} \left[ \frac{e^{i\phi_i}}{\omega_i^{-1} - \omega^{-1} - \Gamma_i^{-1}} + \frac{e^{-i\phi_i}}{\omega_i^{-1} + \omega^{-1} + \Gamma_i^{-1}} \right] \quad (4.3)$$

where  $\Gamma_i$  is the interband damping rate and is size independent because it only considers the positive charge the core electrons feel from the nuclei that make up the lattice, and  $A_i$  is a measure of the electron occupation number of the d band.  $\omega_i$  is known as a critical frequency that is described the energy required to induce the excitation of the electron, and  $\phi_i$  is the efficiency of that transition. Figure 4.2 shows the overlay of the AuNPs absorptions spectra with the absorption and emission of AF350. The arrow indicates the peak of the intraband transitions. To the blue of this arrow the intraband transitions decline sharply and the interband transition increase in intensity.

In Figure 4.3, the steady-state intensity quenching for the AF350 Au-DNA conjugate for 15bp (68.75 Å), 22bp (93.08 Å), 30bp (118.1 Å), 45bp (170.0 Å) and 90bp (296.4Å) is shown. Control over the dye to AuNP separation distance is achieved by appending the dye to the distal end of double stranded DNA through a 5'-phosphate modification. The choice of DNA lengths reflect desire to measure quenching behavior in the near-field (15-30bp) as well as the far-field (45 and 90bp). For this study, DNA is assumed to conform to a rigid rod approximation over the experimental length scale, allowing the separation distance to be calculated from the 2 nm AuNP surface to the center of the dye using the Clegg model [67]. The experimental results on AF350 in Figure 4.3 show >95% quenching the steady state results irrespective of the dye-AuNP separation distance.

The appended DNA experiments were conducted in dilute solutions to eliminate the effects of self-quenching and the inner filter effect of the AuNP absorption of incident light. Comparison of the results to earlier studies on LSPR intraband effects on quenching indicate the >95% quenching at all experimentally measured distances is surprising and likely implies that coupling of the excited state wavefunction of the dye with the interband transitions of the AuNP is different than coupling to the intraband transition.

Melting studies were done to ensure the dye is not being damaged during the experiments. The AF350 labeled ds-DNA were heated from RT, (about 20 °C) to 30 °C, 50 °C, 70 °C and 100 °C and the cooled back down to RT. In Figure 4.4 it is clear that as the DNA melts the labeled strand diffuses away from the particle resulting the fluorescent signal is recovered. It is apparent that over the course of the study the AF350 labeled strand does unanneal resulting in the AF350 emission turning on. The melting study was done on two different strand lengths. The 15mer melting signal does not return to the original room temperature measurement which led to

the conclusion that some of the linker strand must have dissociated from the surface over the course of the experiment. This resulted in signal from free dye being observed after the sample was heated, and then cooled to RT.

**Table 4.1** List of DNA sequences used in the proximal study of the quenching of AF350 by 2nm AuNPs

15mer-AF350 68 Å	AF350-C6-CGTGTGAATTCGTGC
15mer-SH	RSS-C6-GCACGAATTCACACG
22mer- AF350 93 Å	AF350-C6-CGCCTACTACCCAGTCATCAGC
22mer-SH	RSS-C6-GCTGACTGGGTAGTAGGCG
30mer- AF350 117 Å	AF350-C6- CGCCTACTACCGAATTCGATAGTCATCAGC
30mer-SH	RSS-C6-GCTGATGACTATCGAATTCGGTAGTAGGCG
45mer- AF350 170 Å	AF350-C6- CGTTCCGTGTGCATACTGAATTCCGTGTTACTCTTGCCAACCTCG
45mer-SH	RSS-C6- CGAGGTTGGCAAGAGTAACACGGAATTCAGTATGCACACGGAACG
90mer- AF350 310 Å	AF350-C6- CGTTCCGTGTGCATACTGAATTCCGTGTTACTCTTGCCAACCTC GCGTTCCGTGTGCATACTGAATTCCGTGTTACTCTTGCCAACCTCG
90mer-SH	RSS-C6- CGAGGTTGGCAAGAGTAACACGGAATTCAGTATGCACACGGAACG CGAGGTTGGCAAGAGTAACACGGAATTCAGTATGCACACGGAACG

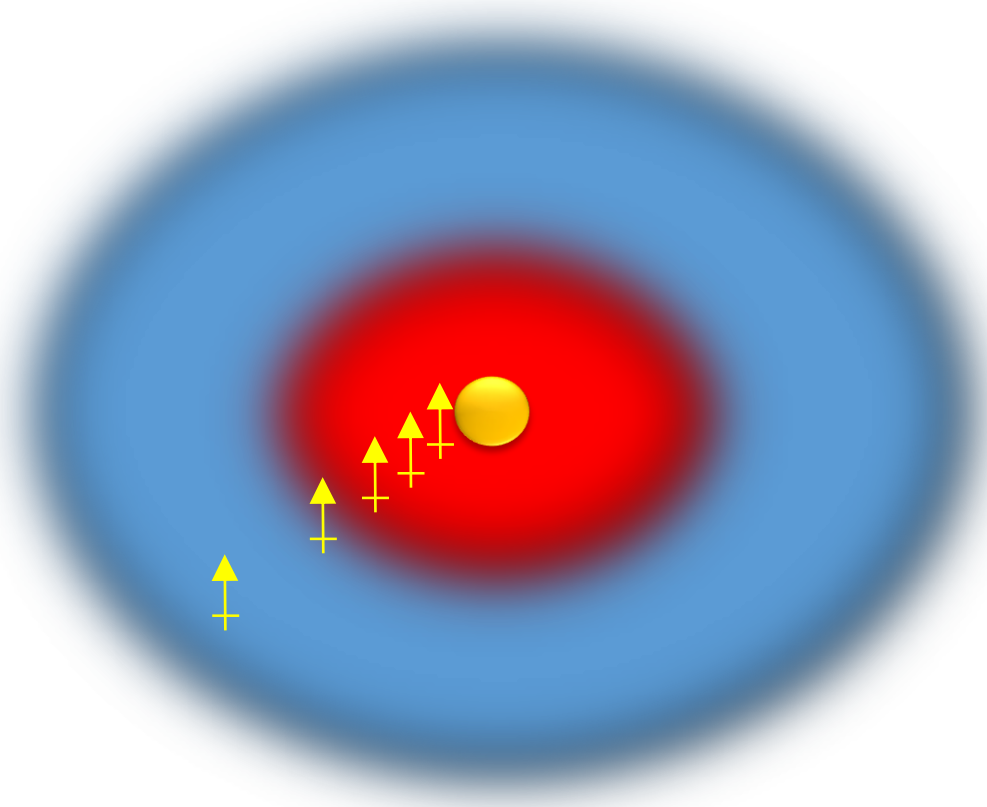


**Figure 4.1** Illustration the experimental approach to investigating the distance dependence of the quenching behavior blue dyes will have. The gold ball in the middle represents the AuNP, the red cloud its near-field, the blue its far-field, and the yellow arrows dipoles at discrete distances from the AuNP

The melting study reached a maximum at 100 °C but did not reach the level expected when compared to the control with the free gold and unappended dye labeled DNA. This may be a result in a drop in quantum yield with increasing temperature. To test this hypothesis a heating study was done on the AF350 labeled strand in the absence of AuNPs and it was indeed found that as the temperature increased the signal decreased, shown in Figure 4.5. This effect could be the result of nonradiative pathways opening up as kinetic energy of the system is increased.

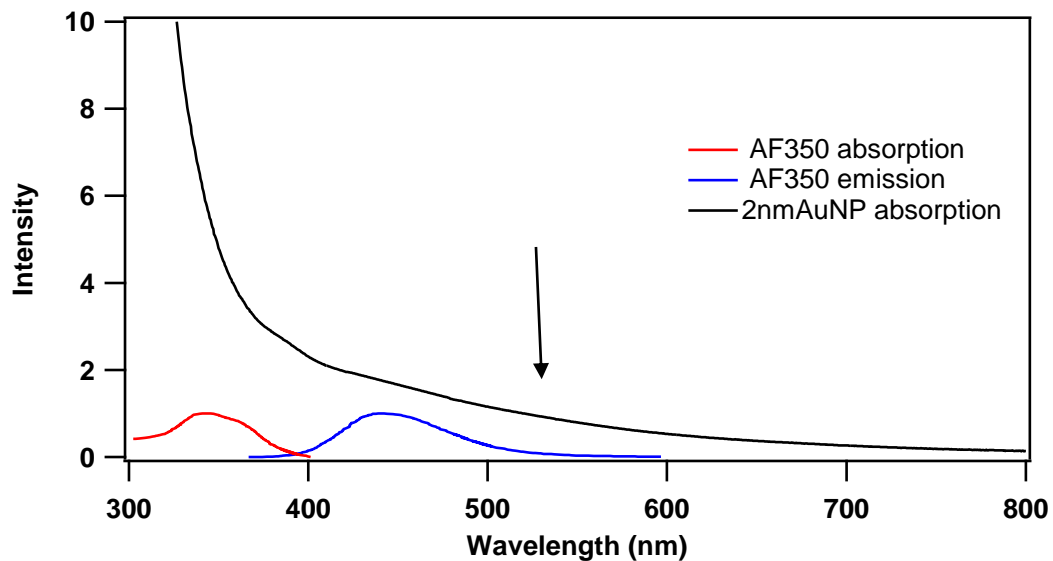


**Figure 4.2** Spectral overlay of 2nm absorption spectra with AF350 absorption and emission. The arrow at 520nm indicates the decline of the intraband and the beginning of the interband transitions

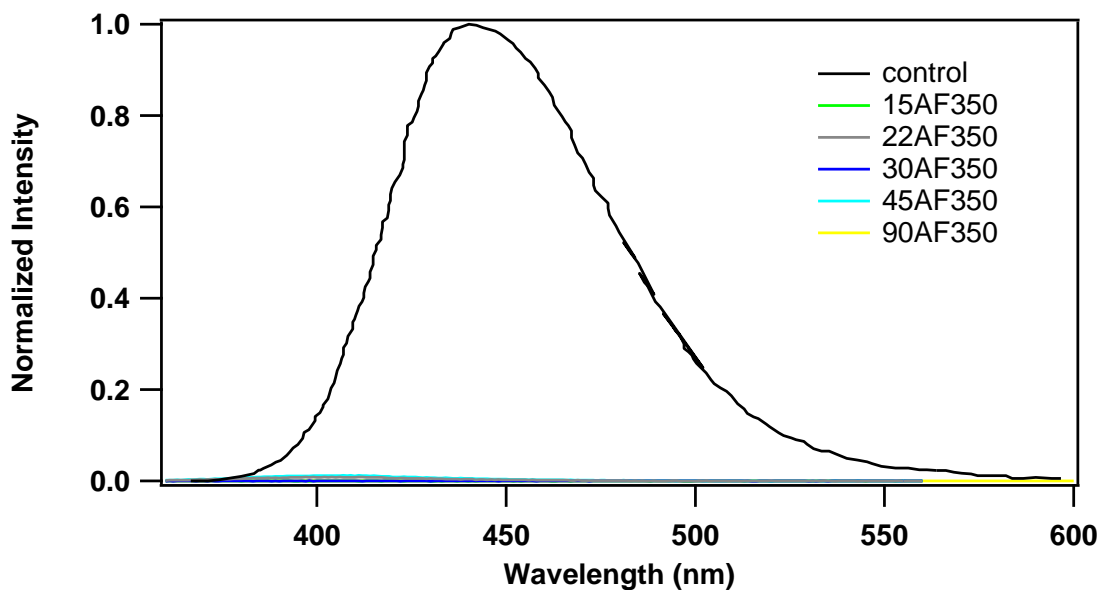


**Figure 4.3** Normalized PL intensity for AF350 for the control (AF350 labeled strand in the presence of unappended AuNPs) and the different length strands appended to the surface of the 2nm AuNP

A plot of the quenching data for AF350 versus distance is shown in Figure 4.6 along with the original empirical NSET, the size dependent NSET, and the CPS-Kuhn model predictions. The poor agreement between data and theory confirms the failure of the available NSET models to predict quenching behavior for dyes that overlap the interband transition in the AuNPs. Agreement with the CPS-Kuhn model cannot be confirmed or denied with the limited distances DNA can achieve, due to the limited distance range for maintaining a rigid rod approximation for DNA (<100bp, 330 Å including the C6 spacers) the lengths required to map the full behavior exceed the experimental range for DNA based distance control in this study. In an attempt to further understand the strong quenching behavior a Stern-Volmer Study was carried-out to allow the extrapolation of the radius of the quenching sphere around AF350 to be calculated, in order to determine the  $d_0$  value.

#### 4.4 Stern-Volmer Studies

##### 4.4.1 Stern-Volmer on AF350

Stern-Volmer studies were conducted in order to determine if the observed range of quenching is reasonable. Stern-Volmer quenching assumes that a sphere of action exists around the emitting dye wherein if a single quencher is present the dye will be 100% quenched. This sphere has a volume that can be calculated by rearranging equation 4.4

$$\lambda = V[Q]N/1000 \quad (4.4)$$

where  $\lambda$  is the mean number of quenching inside the sphere of action, V is the volume of the sphere of action, [Q] is the concentration of the quenching in this case AuNPs, N is Avogadro's number. In order to solve for V  $\lambda$  is set to 1 and the Q is set at the concentration where 50% of the signal is quenched, this value is the reciprocal of the measured  $K_{SV}$ .

During the proximal experiments, where the DNA is appended to the AuNP, the steady state measurements are taken after dilutions are done to the reaction to obtain maximum signal. This has to be done because of what is known as the “inner filter effect” [85]. This effect points out that a portion of the incident light is absorbed by the AuNP resulting in decreased signal from the fluorophore not because the fluorescence is quenched but a smaller population of fluorophores are excited initially. This is a difficult problem to get around due to the differences in extinction coefficients of the AuNPs and the fluorophore at the wavelength that the system needs to be pumped at. For example, with AF350 the experiment is pumped at 350nm. At this wavelength AF350 has an extinction coefficient of  $19,000 \text{ (cm}\cdot\text{M)}^{-1}$  and the AuNP's is over  $300,000 \text{ (cm}\cdot\text{M)}^{-1}$ . This results in the AuNP absorbing an order of magnitude more incident light than AF350 when there is a 1:1 ratio between their concentrations, as is the case during the appended experiments and the corresponding controls. To avoid this as much as possible in all the Stern-Volmer experiments AF350 was at least 5 times more concentrated than the AuNP. For these experiments the concentration of the AF350 labeled DNA was kept constant at 1.75mM and the concentration of 2nm AuNP was varied.

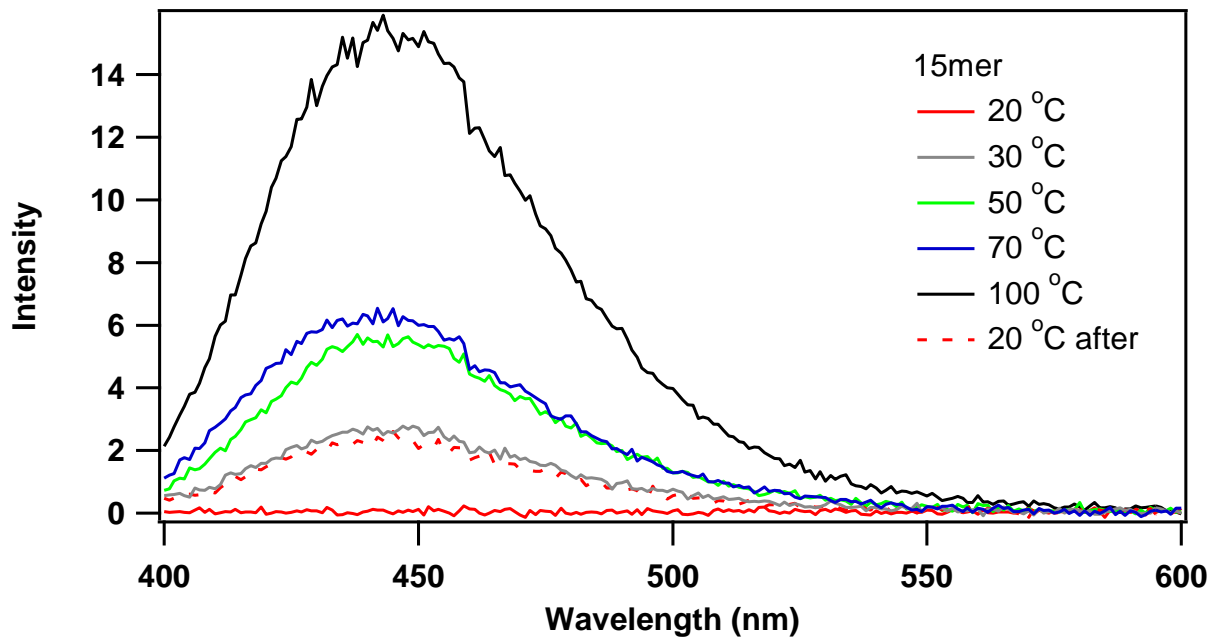
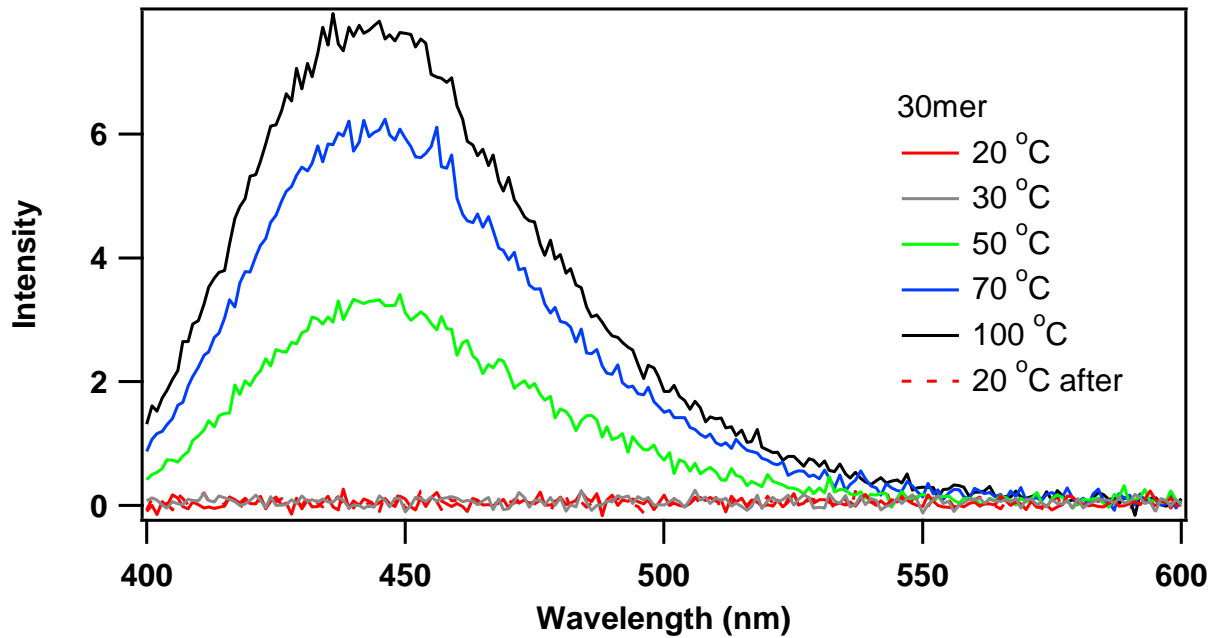
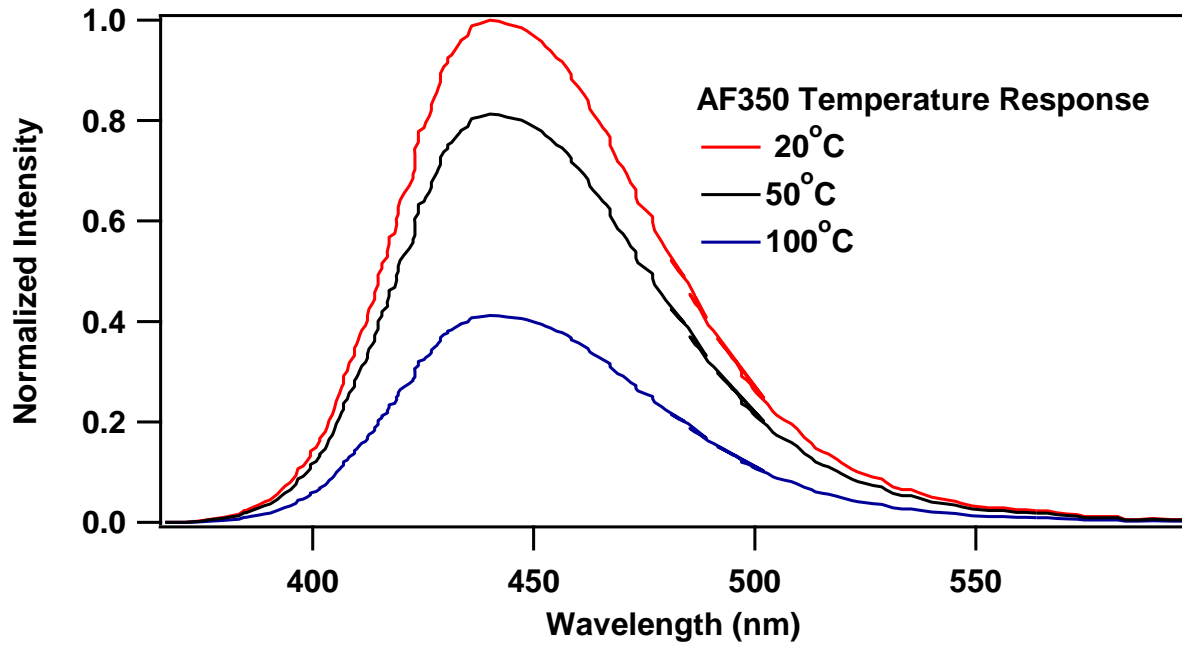


**Figure 4.4** Melting study indicates that as the ds-DNA is melted the AF350 signal returns as the labeled strand diffuses away

a)



b)

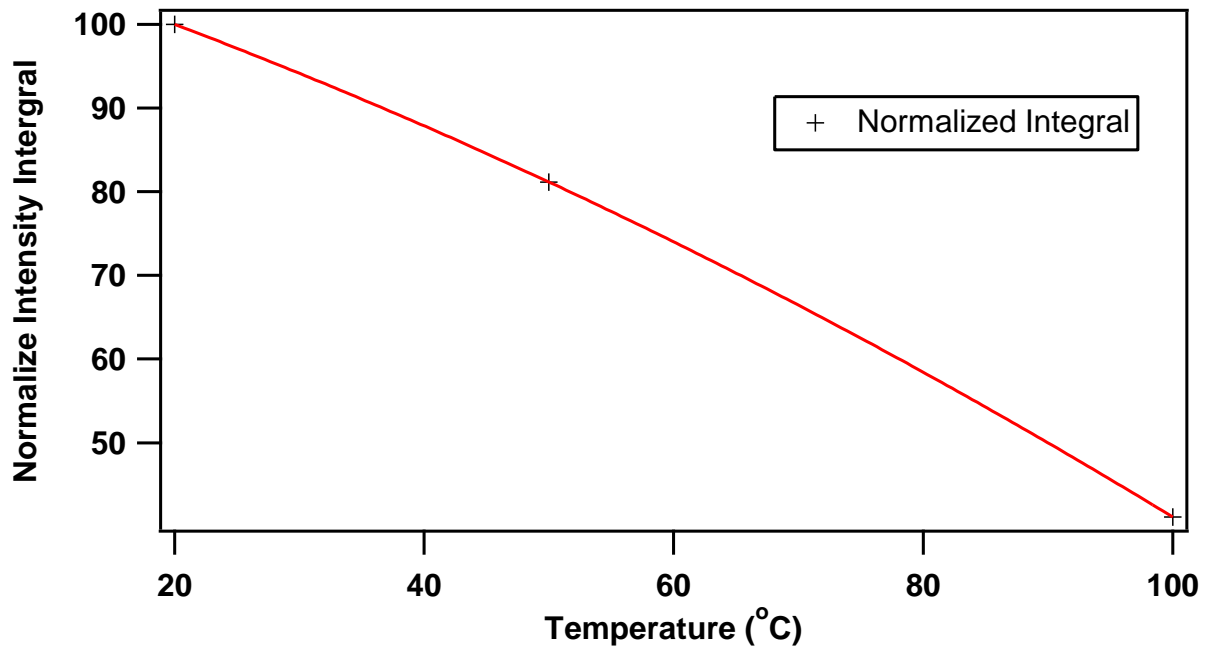


**Figure 4.5** a) Temperature dependence of free AF350 labeled DNA. b) Plot of the normalized integrals for the temperature dependence

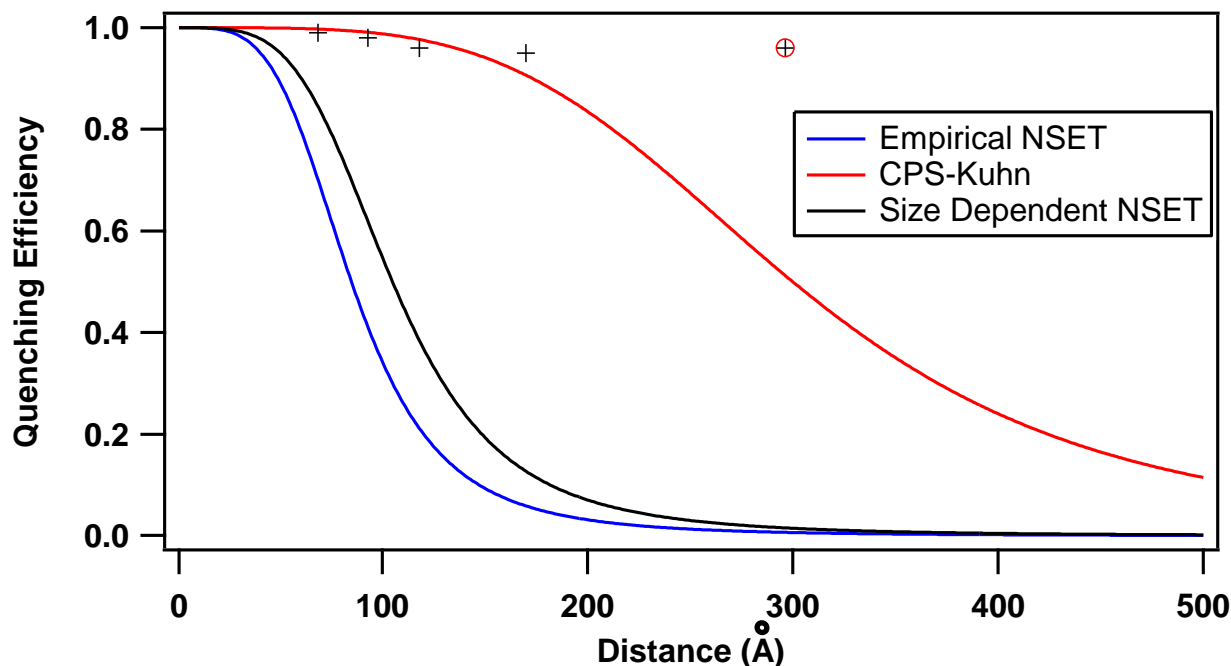


**Figure 4.6** Efficiency curves for several theories explaining resonant energy transfer coupled to the LSPR of metal NPs the data point with the red circle around it represents the 90mer and is noted because it is likely that the rigid rod approximation is failing

The amount of quenching was monitored via steady state emission. The raw data is shown in Figure 4.7. For the most dilute sample of AuNP a larger decrease in intensity is observed than would expected from just an inner filter effect. The AuNP concentration is 1/100<sup>th</sup> of the AF350 labeled DNA. At this ratio just by the inner filter effect a less than 10% drop in intensity is expected, instead a 70% drop is observed. Using the Stern-Volmer equation (4.5) the extent of the quenching can be compared to other dyes.

$$\frac{I_0}{I} = 1 + K_{sv}[Q] \quad (4.5)$$

where  $I_0$  and  $I$  are the integrated photoluminescence intensity of the emitter in the absence of and in the presence of the quencher, respectively.  $K_{sv}$  is the Stern-Volmer constant for the system

and  $Q$  is the quenching concentration. Figure 4.7 plots the  $I_0/I$  values and the inner filter corrected values which are used to extract the  $K_{SV}$ .

Clearly the more concentrated the AuNPs, the less signal detected from AF350. A plot of  $I_0/I$  vs.  $[AuNP]$  yields the classic Stern-Volmer plot. The linear nature of the concentration dependence, observed in Figure 4.7, is indicative of collisional quenching opposed to static quenching. Further proof would be represented in the lifetime quenching data but the extent of quenching even at low AuNPs prevented any lifetime measurements from being obtained. Without the lifetime studies to correlate the steady state experiments with, static quenching cannot be completely be ruled out, but these experiments have been designed to minimize static interactions by passivated the surface with BSPP which is negatively charged and should repel the negatively charged phosphate backbone of the ds-DNA. With this information it is possible to conclude that the extra 60% drop in signal most likely results from collisional quenching by the AuNPs.

Comparing the experimentally derived  $K_{SV}$  values for AF350 and AuNPs to literature values for dyes that are in resonance with the LSPR of the AuNPs it is seen to be much larger. This indicates that a lower concentration of AuNPs is required to quench 50% of the emission of AF350 than is needed for quenching redder dyes such as coumarin 153, and acridium ester [7, 107]. Coupled to the information from the proximal quenching with the appended DNA experiments it is possible to conclude that this quenching mechanism must be more efficient than the available resonant energy transfer theories predict.

Using the  $K_{SV}$  from the steady state experiments the 50% quenching concentration was determined to be  $24\mu M$ . This corresponds to a sphere of action with the volume of  $6.9 \cdot 10^{-17} m^3$ . From the volume of the sphere the radius of that sphere for AF350 being quenched by a 2nm

AuNP is 2540nm. This is much longer than any energy transfer model expects. This must be due to the fact that the energy transfer process is different than that of the current models describe.

#### **4.4.2 Diphenyl Anthracene Stern-Volmer**

In an attempt to verify the enhanced quenching behavior coupled to the d-sp transitions, diphenyl anthracene (DPA) was also tested via Stern-Volmer quenching. For the AF350 all the DNA appended samples were quenched so much that it was not possible to obtain enough signal to measure fluorescent lifetimes, DPA was chosen because of its extended native lifetime of 6.7ns. DPA is organically soluble so it was necessary to adjust the synthesis of the 2nm AuNP to remain organically soluble. The particles for this study were synthesized by the biphasic reduction method discussed in chapter two. Instead of using TPP as a capping agent dodecanethiol was used. The choice of a thiol over the phosphine reflects the desire to maintain stability and ensure no exchange of would occur at the surface during the experiment. The resulting 2nm AuNPs were organically soluble and quite stable due to the thiol group. The DPA Stern-Volmer plot of  $I_0/I$  is plotted in Figure 4.8.

The quenching data does seem to indicate enhanced quenching at low concentrations of AuNPs. In this study the DPA concentration was kept constant at 1mM and the most concentrated AuNP sample was 32 $\mu$ M. The choice of not to go more concentrated than 32 $\mu$ M reflects the lack of PL signal due to the increased inner filter effect. Unfortunately, the quenching data alone is not sufficient enough to claim enhanced quenching so lifetimes were taken of the samples. The results are in Figure 4.9.

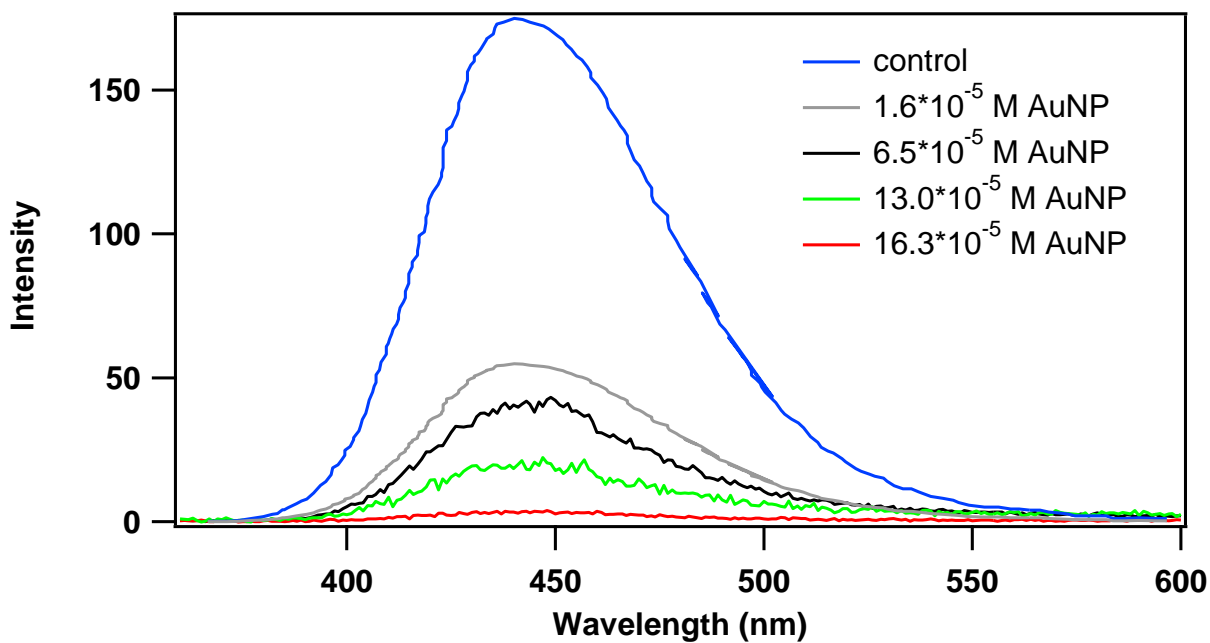
According to the lifetime results there is no significant change the radiative decay rate over concentration range studied. Anthracene has been known to intercalate into long carbon chains [86] and it was hoped that the addition of the two phenyl groups would limit the packing

efficiency of the DPA into the dodecanthiol that passivated the AuNP. The lack of agreement between the steady state and the lifetime data, illustrated in Figure 4.9, indicates that there is significant of static interaction. Further studies are required to eliminate static quenching contributions from the data.

#### **4.5 Conclusions**

Energy transfer can be thought of as a ball rolling down hill in most applications. FRET, the most basic example, has a higher energy excited state donor and its energy (the ball) rolls downhill to a lower energy excited state of an acceptor. For all the experiments discussed previously with NSET a resonance between the donor dye and accepting AuNP is met but the emissions of the donor is lower energy than the dominant feature in the absorption, the LSPR at 520nm. In this chapter a “downhill” type energy transfer process was investigated from a set of high frequency dye to 2nm AuNPs. The extinction spectra can be divided into scattering and absorption terms reflecting the real and imaginary dielectric dispersion curves for the transitions [32, 19, 74, 76]. This study was conducted to minimize the real (scattering) component in an effort to observe the higher energy interactions between a fluorophore and AuNPs. Minimization of the scattering was very important for this study as higher frequency radiation is scattered more efficiently and a large scattering artifact in the measurements would have been detrimental to the study. As it is, a distant dependent quenching model cannot be used to explain the proximal quenching of AF350 by 2nm AuNPs. In order to determine whether there is, in fact, a distance dependence to the coupling of the interband transitions through the far field the experiment needs to be redesigned to be able enable longer distances to be mapped.

a)



b)

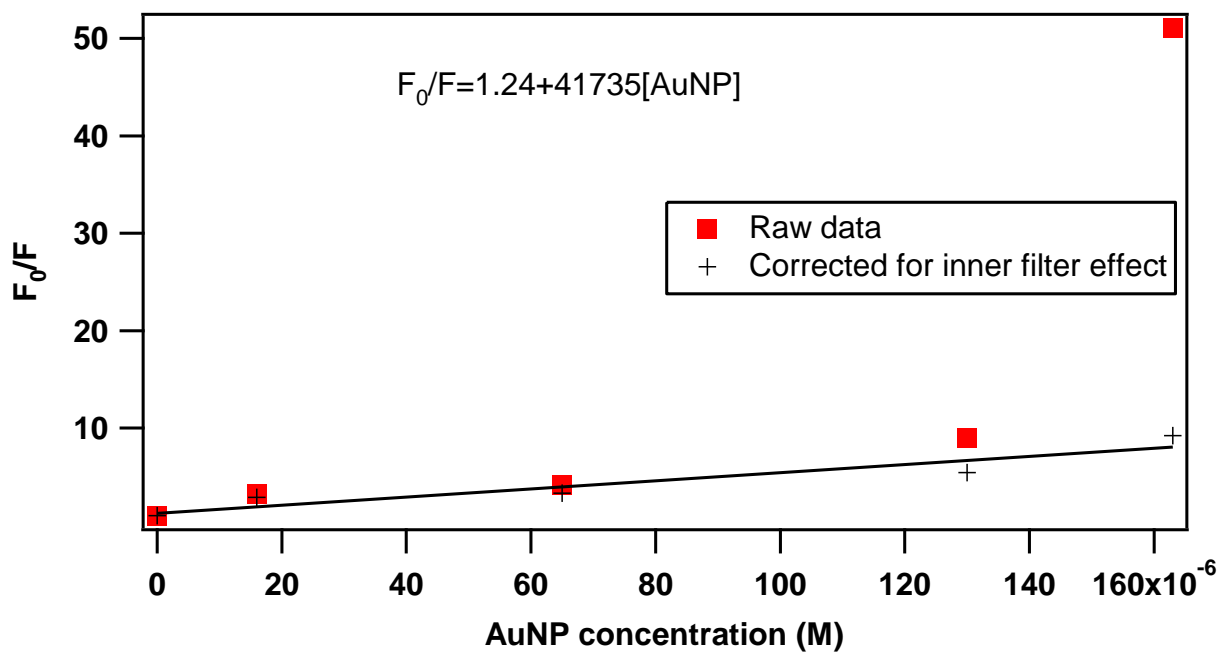


**Figure 4.7** a) Raw data for Stern-Volmer studies on AF350 b) Stern-Volmer plot included points corrected for the inner filter effect with line of best fit on the corrected data to extract a  $K_{SV}$  of  $41735\text{M}^{-1}$

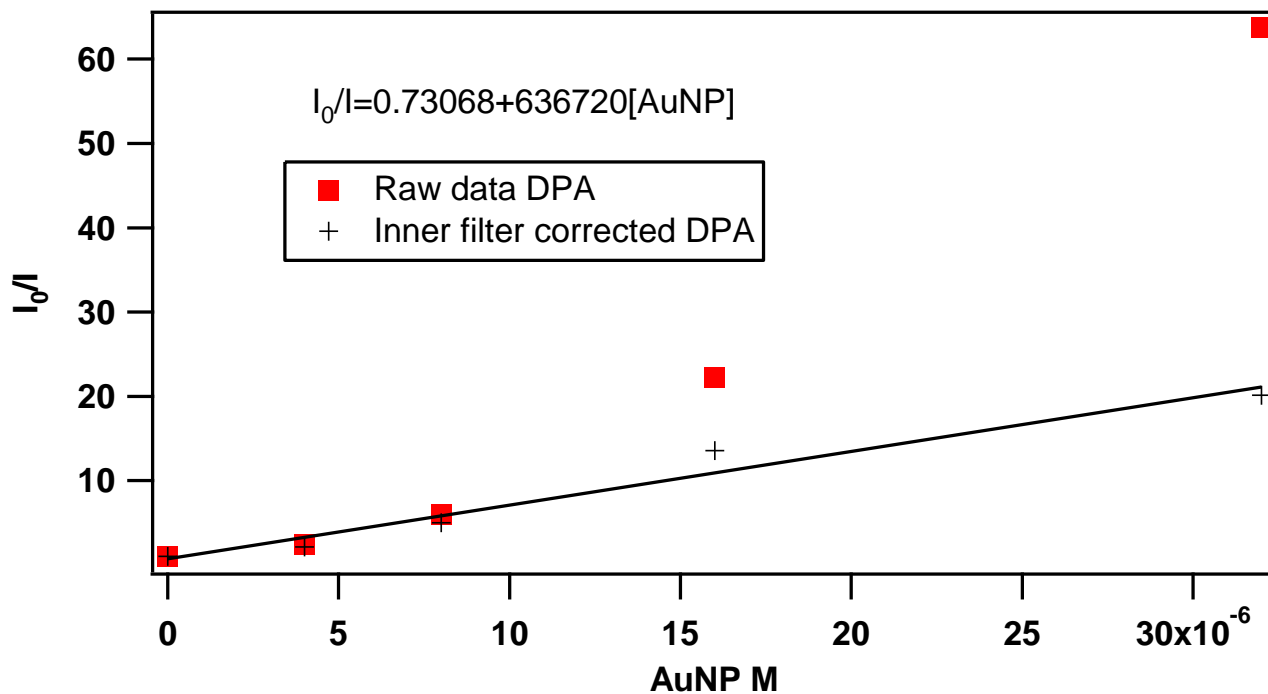


**Figure 4.8** The  $I_0/I$  plots of the intensity integrals of the diphenyl anthracene fluorescence in the presence of various 2nm AuNP concentrations along with the points corrected for the inner filter effect and a best fit line to extract a  $K_{SV}$  of  $636720M^{-1}$

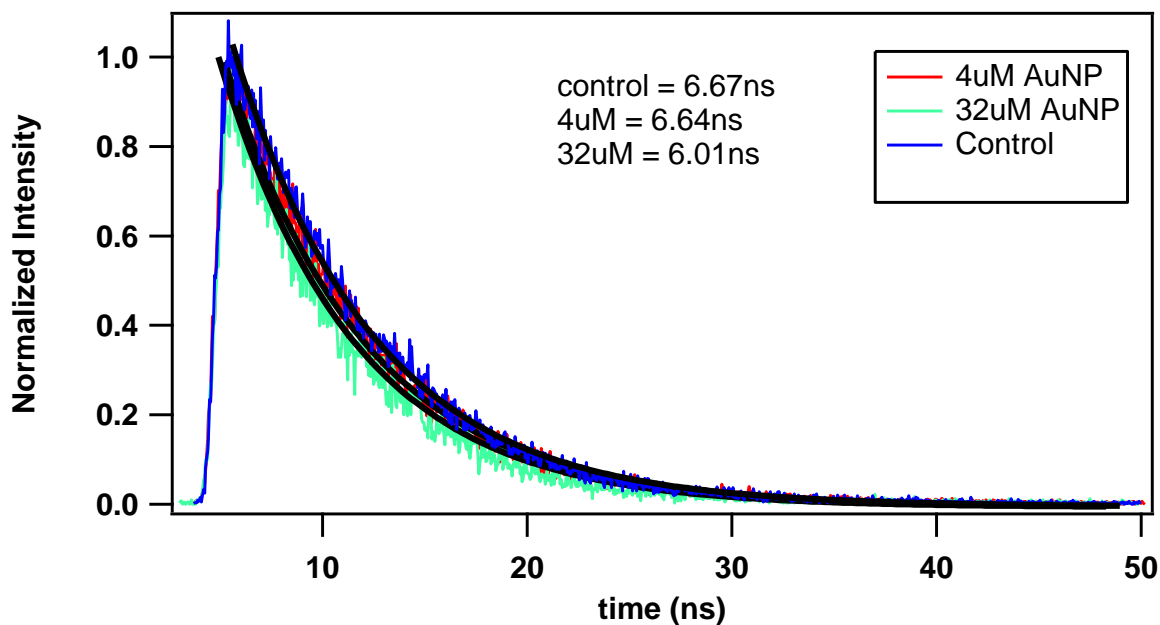


**Figure 4.9** Lifetime results for Stern-Volmer studies on the least concentrated and most concentrated AuNP samples with single exponential decay fits.

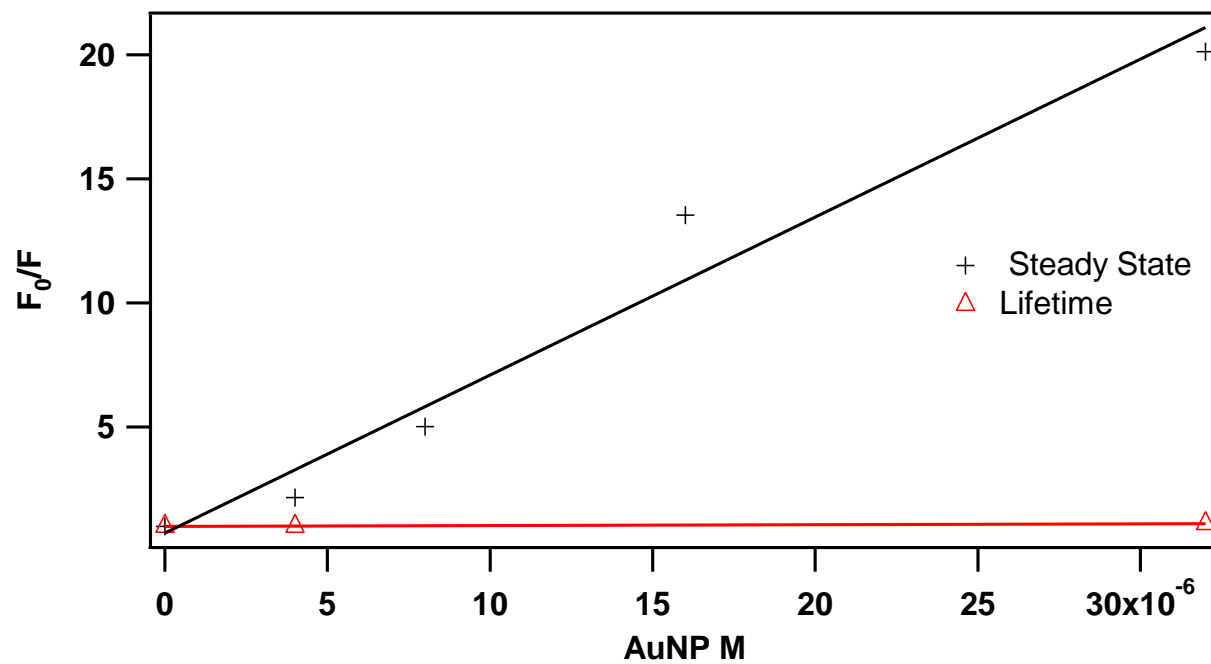


**Figure 4.10** Plot of the  $\tau_0/\tau$  and  $I_0/I$  data showing a lack of agreement between lifetime and steady state experiments leads to the conclusion of static quenching of the DPA

## REFERENCES

- [1] Borisov, S. M.; Wolfbeis, S. M. *Chem. Rev.* **2008**, 108, 423-461.
- [2] Anker, J. N.; Hall, W. P.; Lyandres, O.; Shah, N. C.; Zhao, J.; van Duyne, R. D. *Nat. Mater.* **2008**, 7, 442-453.
- [3] Adleman, J. R.; Boyd, D. A.; Goodwin, D. G.; Psaltis, D. *Nano Lett.*, **2009**, 9 (12), 4417-4423
- [4] Liu, X.; Freeman, R.; Golub, E.; Willner, I. *ACS Nano*, **2011**, 5 (9), 7648-7655
- [5] Chen, N. T.; Cheng, S. H.; Liu, C. P.; Souris, J. S.; Chen, C. T.; Mou, C. Y.; Lo, L. W. *Int. J. Mol. Sci.* **2012**, 13, 16598-16623.
- [6] Gersten, J.; Nitzan, J. *Chem. Phys.* **1981**, 75, 1139-1152.
- [7] Ghosh, D.; Chattopadhyay, N. *Opt. Photon. J.* **2013**, 3, 18-26.
- [8] Ruppin, R. *J. Chem. Phys.* **1982**, 76, 1681-1684.
- [9] Kreibig, U.; Vollmer, M. *Optical Properties of Metal Clusters*. Vol. 25 (Springer-Verlag, 1995).
- [10] Lakowicz, J. R. *Principles of Fluorescence Spectroscopy*, 2006, Springer Science, LLC.
- [11] Dulkeith, E.; Ringler, M.; Klar, T. A.; Feldmann, J.; Javier, A. M.; Parak, W. J. *Nano Lett.* **2005**, 5, 585-589.
- [12] Novotny, L.; Hecht, B. *Principles of Nano-Optics*. (Cambridge University Press, 2006).
- [13] González-Díaz, Juan B.; García-Martín, Antonio; García-Martín, José M.; Cebollada, Alfonso; Armelles, Gaspar; Sepúlveda, Borja; Alaverdyan, Yury; Käll, Mikael *Small* **2008** 4 (2): 202-5.
- [14] Du, Guan Xiang; Mori, Tetsuji; Suzuki, Michiaki; Saito, Shin; Fukuda, Hiroaki; Takahashi, Migaku *Appl. Phys. Lett.* **2010** 96 (8): 081915
- [15] Boardman, A. *Electromagnetic surface modes* J. Wiley, NY 1982
- [16] S. Link, M.A. El-Sayed, *J. Phys. Chem. B* **1999** 103, 8410
- [17] Long, N. N; Vu. L. V.; Kiem, C. D.; Doanh, S. C.; Nguyet, C. T.; Hang, P. T.; Thien, N. D.; Quynh, L. M. *J. of Physics: Conference Series* **2009**, 187, 012026

- [18] Moskovits, M. *Rev. Mod. Phys.* **1985**, 57, 783-826.
- [19] Jennings, T. L.; Schlatterer, J. C.; Singh, M. P.; Greenbaum, N. L.; Strouse, G. F. *Nano Lett.* **2006**, 6, 1318-1324.
- [20] Huang, X.; Jain, P. K.; El-Sayed, I. H.; El-Sayed, M. A. *Photochem Photobiol.* **2006**, 82 (2), 412- 417
- [21] ] Stryer, L.; Haugland, R. P. *Proc. Nat. Acad. Sci.* **1967**, 58, 719-725.
- [22] Clapp, A. R.; Medintz, I. L.; Mauro, J. M.; Fisher, B. R.; Bawendi, M. G.; Mattoussi, H. *J. Am. Chem. Soc.* **2004**, 126, 301-310.
- [23] Eliseeva, S. V.; Bunzli, J. C. G. *Chem. Soc. Rev.* **2010**, 39, 189-227.
- [24] Selvin, P. R.; Hearst, J. E. P. *Natl. Acad. Sci.* **1994**, 91, 10024-10028.
- [25] Selvin, P. R. *Annu. Rev. Bioph. Biom.* **2002**, 31, 275-302.
- [26] Wingert, P. A.; Mizukami, H.; Ostafin, A. E. *Nanotech.* **2007**, 18, 29570-29577.
- [27] Sapsford, K. E.; Berti, L.; Medintz, I. L. *Angew. Chem. Int. Ed.* **2006**, 45, 4562-4588.
- [28] Pflieger, K. D. G.; Eidne, K. A. *Nature Methods* **2006**, 3, 165-169.
- [29] Pons, T.; Medintz, I. L.; Wang, X.; English, D. S.; Mattoussi, H. *J. Am. Chem. Soc.* **2006**, 128, 15324-15331.
- [30] Yasuda, R.; Masaike, T.; Adachi, K. et. al. *Proc. Nat. Acad. Sci.*, **2003**, 100, 9314-9318.
- [31] Yun, C. S.; Javier, A.; Jennings, T.; Fisher, M.; Hira, S.; Peterson, S.; Hopkins, B.; Reich, N. O.; Strouse, G. F. *J. Am. Chem. Soc.* **2005**, 127, 3115- 3119.
- [32] Jennings, T. L.; Singh, M. P.; Strouse, G. F. *J. Am. Chem. Soc.* **2006**, 128, 5462-5467.
- [33] Singh, M. P.; Strouse, G. F. *J. Am. Chem. Soc.* **2010**, 132, 9383-9391.
- [34] Bardhan, R.; Grady, N. K.; Cole, J. R.; Joshi, A.; Halas, N. J. *ACS Nano* **2009**, 3 (3), 744-752
- [35] Fore, S.; Koberling, F.; Koenig, M.; Kapusta, P.; Kraemer, B.; Ewers, B.; Erdmann, R.; Ruettinger, S.; Fiore, J. L.; Nesbitt, D. *Biophysical Journal* **2012**, 102, 199-204
- [36] Babu, R.; Periasamy, A. *J. of Cell Biology* **2003**, 160, 629-633
- [37] Truong, K.; Ikura, M.; *Biophysical Methods* **2001**, 11, 573-578

- [38] Kuhn, H. *J. Chem. Phys.* **1970**, *53*, 101-108.
- [39] Chance, R. R.; Prock, A.; Silbey, R. *J. Chem. Phys.* **1975**, *62*, 2245-2253.
- [40] Chance, R. R.; Prock, A.; Silbey, R. *Adv. Chem. Phys.* **1978**, *37*, 1-65.
- [41] Johnson, P. B.; Christy, R. W. *Phys. Rev. B* **1972**, *6*, 4370-4379
- [42] Persson, B. N. J.; Lang, N. D. *Phys. Rev. B* **1982**, *26*, 5409-5415.
- [43] Xing, T.; Sunarso, J.; Yang, W.; Yin, Y.; Glushenkov, A. M.; Li, L. H.; Howlett, P. C.; Chen, Y. *Nanoscale* **2013**, *5*, 7970-7976
- [44] Kimling, J.; Maier, M.; Okenve, B.; Kotaidis, V.; Ballot, H.; Plech, A. *J. Phys. Chem. B* **2006**, *110* (32), 15700-15707
- [45] Daniel, M; Astruc, D. *Chemical Reviews* **2004**, *104* (1), 293-346
- [46] Huheey, J. E. *Inorganic Chemistry: Principles of Structure and Reactivity* (Dorling Kindersley Pvt Ltd, 2008).
- [47] Hayat, M. A. *Colloidal Gold: Principles, Methods and Applications* vol. 1 1989, Academic Press, Inc.
- [48] Jennings, T. L.; Strouse, G. F. *Adv. Exp. Med. Biol* **2007**, *620*, 34-47.
- [49] Medintz, I. L.; Uyeda, H. T.; Goldman, E. R.; Mattoussi, H. *Nature Mater.* **2005**, *4*, 435-446.
- [50] Swierczewska, M.; Lee, S.; Chen, X. Y. *Phys. Chem. Chem. Phys.* **2011**, *13*, 9929-9941.
- [51] Dubertret, B.; Calame, M.; Libchaber, A. J., *Nat. Biotechnol.* **2001**, *19*, 365-370.
- [52] Forster, T. *Ann. Phys.* **1948**, *2*, 55-75.
- [53] Griffin, J.; Singh, A. K.; Senapati, D.; Rhodes, P.; Mitchell, K.; Robinson, B.; Yu, E.; Ray, P. *Chem. Eur. J.* **2009**, *15*, 342-351.
- [54] Chowdhury, S.; Wu, Z. K.; Jaquins-Gerstl, A.; Liu, S. P.; Dembska, A.; Armitage, B. A.; Jin, R. C.; Peteanu, L. A. *J. Phys. Chem. C* **2011**, *115*, 20105-20112.
- [55] Link, S.; El-Sayed, M. A. *Int. Rev. Phys. Chem.* **2000**, *19*, 409-453.
- [56] Kelly, K. L.; Coronado, E.; Zhao, L. L.; Schatz, G. C. *J. Phys. Chem. B* **2003**, *107*, 668-677.

- [57] Acuna, G. P.; 1318-1324 Bucher, M.; Stein, I. H.; Steinhauer, C.; Kuzyk, A.; Holzmeister, P.; Schreiber, R.; Moroz, A.; Stefani, F. D.; Liedl, T.; Simmel, F. C.; Tinnefeld, P. *ACS Nano* **2012**, *6*, 3189-3195.
- [58] Han, H.; Valle, V.; Maye, M. M. *Nanotechnology* **2012**, *23*, 435401-435407.
- [59] Carminati, R.; Greffet, J. J.; Henkel, C.; Vigoureux, J. M. *Opt. Comm.* **2006**, *261*, 368-375.
- [60] Chew, H. *J. Chem. Phys.* **1987**, *87*, 1355-1360.
- [61] Pustovit, V. N.; Shahbazyan, T. V. *J. Chem. Phys.* **2012**, *136*, 204701-204707.
- [62] Saini, S.; Srinivas, G.; Bagchi, B. *J. Phys. Chem. B* **2009**, *113*, 1817-1832.
- [63] Etchegoin, P. G.; Le Ru, E. C.; Meyer, M. *J. Chem. Phys.* **2006**, *125*, 164705-164708.
- [64] Jain, P. K.; Lee, K. S.; El-Sayed, I. H.; El-Sayed, M. A. *J. Phys. Chem. B* **2006**, *110*, 7238-7248.
- [65] Liu, X. O.; Atwater, M.; Wang, J. H.; Huo, Q. *Colloids Surf. B* **2007**, *58*, 3-7.
- [66] Chhabra, R.; Sharma, J.; Wang, H. N.; Zou, S. L.; Lin, S.; Yan, H.; Lindsay, S.; Liu, Y. *Nanotechnology* **2009**, *20*, 485210-485211.
- [67] Clegg, R. M.; Murchie, A. I. H.; Zechel, A.; Lilley, D. M. J. *Proc. Natl. Acad. Sci. USA* **1993**, *90*, 2994-2998.
- [68] Hill, H. D.; Millstone, J. E.; Banholzer, M. J.; Mirkin, C. A. *ACS Nano* **2009**, *3*, 418-424
- [69] Li, Z. G.; Niu, T. X.; Zhang, Z. J.; Chen, R.; Feng, G. Y.; Bi, S. P. *Biosensors & Bioelectronics* **2011**, *26*, 4564-4570
- [70] Sardar, R.; Funston, A. M.; Mulavaney, P.; Murray, R. W. *Langmuir* **2009**, *25*, 13840-13851.
- [71] Daniel, M. C.; Astruc, D. *Chem. Rev.* **2004**, *104*, 293-346.
- [72] Giljohann, D. A.; Seferos, D. S.; Daniel, W. L.; Massich, M. D; Patel, P. C.; Mirkin, C. A. *Angew. Chemie-Intl. Ed.* **2010**, *49*, 3280-3294.
- [73] Huang, X. H.; Neretina, S.; El-Sayed, M. A. *Adv. Mater.* **2009**, *21*, 4880-4910.
- [74] Lakowicz, J. R. *Anal. Biochem.* **2005**, *337*, 171-194.
- [75] Alvarez, M. M.; Khoury, J. T.; Schaaff, T. G.; Shafigullin, M. N.; Vezmar, I.; Whetten, R. L. *J. Phys. Chem. B* **1997**, *101*, 3706-3712.

- [76] Wiederrecht, G. P.; Wurtz, G. A.; Hranisavljevic, *J. Nano. Lett.* **2004**, 4, 2121-2125.
- [77] Pinchuk, A.; Plessen, G.; Kreibig, U. *J. Phys. D: Appl. Phys.* **2004**, 37, 3133- 3139.
- [78] Chen, Y.; Munechika, K.; Ginger, D. S. *Nano Lett.* **2007**, 7, 690-696.
- [79] ] Malicki, M.; Hales, J. M.; Rumi, M.; Barlow, S. McClary, L.; Marder, S. R.; Perry, J. W. *Phys. Chem. Chem. Phys.*, **2010**, 12, 6267-6277.
- [80] Jensen, T.; Kelly, L.; Lazarides, A.; Schatz, G. C. *J. Cluster Sci.* **1999**, 10, 295-317.
- [81] Stiles, P. L.; Dieringer, J. A.; Shah, N. C.; van Duyne, R. R. *Ann. Rev. Anal. Chem.* **2008**, 1, 601-626.
- [82] Haes, A. J.; Zou, S. L.; Zhao, J.; Schatz, G. C.; van Duyne, R. R. *J. Am. Chem. Soc.* **2006**, 128, 10905-10914.
- [83] Das, P.; Metiu, H. *J. Phys. Chem.* **1985**, 89, 4680-4687.
- [84] Larsen, R. E.; Metiu, H. *J. Chem. Phys.* **2001**, 114, 6851-6860.
- [85] Borissevitch, I. E. *Journal of Luminescence* **1999**, 81 (3), 219-224.
- [86] Ogawa, M.; Kuroda, K.; Kato, C. *Studies in Surface Science and Catalysis* **1994**, 83, 171-178
- [87] Mie, Gustav *Annalen der Physik* **1908**, 330 (3), 377-445.
- [88] Qian, H.; Jin, R. *Chem. Mater.* **2011**, 23, 2209-2217.
- [89] M. Zhu, C. M. Aikens, F. J. Hollander, G. C. Schatz, R. Jin, *J. Am. Chem. Soc.*, **2008**, 130, 5883-5885.
- [90] Ziegler, C; Eychmüller, A, *J. Phys. Chem. C* **2011**, 115 (11), 4502-4506
- [91] Liu, Y.; Lin, X; Sun, Y.; Rajh, T., *J. Am. Chem. Soc.*, **2013**, 135 (10), 3764-3767
- [92] Alexandridis, P., *Chemical and Engineering Technology* **2011**, 31, 15-28
- [93] Lopez-Sanchez, J. A.; Dimitratos, N.; Hammond, C.; Brett, G. L.; Kesavan, L; White, S.; Miedziak, P.; Tiruvalam, R.; Jenkins, R. L.; Carley, A. F.; Knight, D.; Kiely, C.J.; Hutchings, G. J., *Nature Chemistry* **2011** 3, 551-556
- [94] Gupta, A. K.; Gupta, M., *Biomaterials* **2005**, 26, 3995-40212
- [95] Wang, H.; Xu, J., Z.; Zhu, J., J.; Chen, H. Y., *J. Crystal Growth* **2002**, 244, 88-94.

- [96] Fedlheim, D., L.; Foss, C. A. *Metal Nanoparticles Synthesis, Characterization and Applications*. (Marcel Dekker Inc., 2002).
- [97] W. Ostwald. **1896**. *Lehrbuch der Allgemeinen Chemie*, vol. 2, part 1. Leipzig, Germany.
- [98] I.M. Lifshitz, V.V. Slyozov (1961). *Journal of Physics and Chemistry of Solids* **1961** 19, 35–50
- [99] Bastus, N. G.; Comenge, J.; Puentes, V., *Langmuir*, **2011**, 27 (17), 11098-11105
- [100] Nghiem, T., H.; Nguyen, T., T.; Fort, E.; Nguyen, T., P.; Hoang, T., M., N.; Nguyen, T., Q.; Tran, H., N., *Adv. Nat. Sci.: Nanosci. Nanotechnol.* **2012**, 3, 015002
- [101] Lambert, J., H., *Photometria sive de mensura et gradibus, colorum et umbrae*, Germany: Eberhardt Klett, **1760**
- [102] Beer, *Bestimmung der Absorption des rothen Lichts in farbigen Flussigkeiten* **1852**, 86, 78-88.
- [103] Starks, C., M.; Liotta, C., L.; Halpern, M., E., *Phase-Transfer Catalysis: Fundamentals I*. (Springer Netherlands, 1994).
- [104] Lakowicz, J. R. *Anal. Biochem.* **2001**, 298, 1-24.
- [105] Dulkeith, E.; Morteani, A. C.; Niedereichholz, T.; Klar, T. A.; Feldmann, J.; Levi, S.A.; van Veggel, F.C.J.M.; Reinhoudt, D. N.; Möller, M.; Gittens, D. I., *Phys. Rev. Lett.* **2002**, 89, 203002-203005.
- [106] Wang, L.; Rouxue, Y.; Ziyang, H.; Lun, W.; Jinghui Z.; Jie, B.; Xun, W.; Qing, P.; Yadong, Li. *Angew. Chem. Int. Ed.* **2005**, 44, 6054–6057.
- [107] Xu, Q.; Liu, J.; He, Z; Yang, S., *Chem. Commun.* **2010**, 46, 8800-8802
- [108] Wijaya, A.; Schaffer, S., B.; Pallares, I. G.; Hamad-Schifferli, K., *ACS Nano* **2009**, 3 (1), 80-86
- [109] Zheng, D.; Seferos, D., S.; Giljohann, D., A.; Patel, P., C.; Mirkin, C. A., *Nano Lett.* **2009**, 9 (9), 3258-3261
- [110] Yan, J., M.; Zhang, X., B.; Akita, T.; Haruta, M.; Xu, Q., *J. Am. Chem. Soc.* **2010**, 132 (15), 5326-5327
- [111] Fan, Z.; Shelton, M.; Singh, A., K.; Senapati, D.; Khan, S., A.; Ray, P., C., *ACS Nano*. **2012**, 6 (2), 1065–1073
- [112] Zhang, Q.; Xie, J.; Yu, Y.; Lee, J., Y., *Nanoscale*, **2010**, 2, 1962-1975

# BIOGRAPHICAL SKETCH

## Profile

Interdisciplinary scientist with strong background in spectroscopy, synthesis, biochemistry and physical modeling of nanoscale measurements and electromagnetic interactions. Has also spent time as lab manager and group leader.

## Education

Bachelor of Science: Chemical Science, 2008  
Florida State University – Tallahassee, FL, USA

Ph. D Inorganic Chemistry, 2014  
Florida State University – Tallahassee, FL, USA

Advisor: Geoffrey F. Strouse

“A study of electromagnetic interactions between metal nanoparticles and organic fluorophores”

## Professional Experience

### Undergraduate Research

August 2006-December 2008 FSU

Professor Geoffrey F. Strouse

Synthesis of metal and metal alloy nanoparticles via chemical reduction with  $\text{NaBH}_4$ .

August 2007-May 2008 FSU

Associate Professor M. Shatruk

Synthesized Tetrathafulvalene-based ligands to be used in multifunctional magneto- and optoelectronic materials

**Outreach Volunteer** August 2010-May 2012 FSU

Performed chemistry demonstrations at middle schools and high schools to encourage interest in pursuing higher education.

**Research Assistant** January 2011-November 2013 FSU

Earned PhD in Inorganic Chemistry specializing in Nanomaterial Spectroscopy

**University Libraries Graduate Advisory Board** August 2012-September 2013

Met with University Library administrators and advised on policy changes

## Accomplishments.

### Peer Reviewed Publications

1. Qilin Dai; Megan E. Foley; Christopher J. Breshike; Adrian Lita; Geoffrey F. Strouse “Ligand-Passivated Eu:Y<sub>2</sub>O<sub>3</sub> Nanocrystals as a Phosphor for White Light Emitting Diodes” *Journal of the American Chemical Society* **2011**; 133 (39) 15475-15486
2. L. Washington, II, M. E. Foley, S. Cheong, L. Quffa, C. J. Breshike, J. Watt, R. D. Tilley and G. F. Strouse “Ostwald’s Rule of Stages and Its Role in CdSe Quantum Dot Crystallization” *Journal of the American Chemical Society* **2012**; 134 (41) 17046-17052
3. D. N. Ventura, S. Li, C. A. Baker, C. J. Breshike, A. L. Spann, G. F. Strouse, H. W. Kroto and S. F. A. Acquah “A flexible cross-linked multi-walled carbon nanotube paper for sensing hydrogen” *Carbon* **2012**; 50 (7) 2672-2674
4. Christopher J. Breshike, Ryan A. Riskowski, Geoffrey F. Strouse “NSET Resized: Correctly predicting the excited state size dependent gold nanoparticle-dye interaction” *J. Phys. Chem. C* **2013**, 117 (45), 23942-23949
5. Christopher J. Breshike, Ryan A. Riskowski, Mani Singh, Geoffrey F. Strouse “Enhanced Coupling of the dsp-band in Gold Nanoparticles with the dipole in Alexa Fluor 350” *pending submission*

6. Christopher J. Breshike, Ryan A. Riskowski, Geoffrey F. Strouse “Energy Transfer to Metal Alloy Nanoparticles from fluorescent dyes” *pending submission*

#### **Presentations**

1. 3<sup>rd</sup> Annual ACC Meeting of the Minds, Tallahassee, FL- April 2008 **Poster**  
“Tetrathiafulvalene-based ligands as building blocks for multifunctional magneto- and optoelectronic materials”
2. 244<sup>th</sup> American-Chemical-Society National Meeting & Exposition, Philadelphia, PA- August 2012 **Poster** “Gold nanoparticles size dependent energy transfer quenching: Extending the optical molecular ruler range.”
3. 244<sup>th</sup> American-Chemical-Society National Meeting & Exposition, Philadelphia, PA- August 2012 **Oral** “Gold nanoparticles size dependent energy transfer quenching: Extending the optical molecular ruler range.”
4. 68<sup>th</sup> Southwest Regional Meeting of the American-Chemical-Society, Baton Rouge, LA- November 2012 **Oral** “Studying the size dependence of gold nanoparticles; energy transfer from fluorophores to gold nanoparticles”
5. 246<sup>th</sup> American-Chemical-Society National Meeting & Exposition, Indianapolis, IN- September 2013 **Oral** “Experimental determination of nanoparticle size dependence on nanometal energy transfer”

#### **Management**

##### **Energy Transfer/Spectroscopy Group Leader** (2011-Present)

Oversaw two junior graduate students and two undergraduate students. Proposed and supervised NSET related experiments as well as data analysis.

##### **Group Manager** (2010-2012)

In charge of purchasing and oversaw group meetings.